

Poly (N-Isopropylacrylamide)-Based Microgels for Contaminant Removal from  
Water

by

Feng Gao

A thesis submitted in partial fulfillment of the requirements for the degree of

Master of Science

Department of Chemistry  
University of Alberta

© Feng Gao, 2021

# Abstract

Polymer based materials have been utilized widely for applications that can be of benefit to human health and the environment. This thesis covers the general scope of polymer materials on bases of star-shaped polymer and temperature-responsive poly (N-isopropylacrylamide) (pNIPAm) microgels, their co-functional polymers, their assemblies, and their applications as an anti-fouling coating layer on membrane surfaces in water remediation systems.

Chapter 1 gives a brief introduction of anti-fouling membrane and stimuli-responsive polymers, their assemblies and applications, and the background on polymer material coated anti-fouling membranes.

Chapter 2 focuses on investigating the anti-fouling properties with the filtration system using star-shaped polymer composed membranes. Star-shaped polymers with a silica core have been designed to enhance the coating stability and anti-fouling properties. The anti-fouling performance could be tuned by varying the star-shaped polymer compositions in the membrane.

Chapter 3 focuses on optimizing the pNIPAm based microgel coating on a polyethersulfone (PES) membrane through a new coating strategy. In this work, the microgel coating stability was investigated by tuning the microgel sizes and coating processes. With optimized microgel sizes and coating processes, the anti-fouling performance also was optimized by varying the charge group (acrylic acid, AAc) compositions in the microgel. A long-term filtration was operated to confirm the coating stability with an AAc composited microgel coated membrane. As a further study of the AAc composited microgel coating in water remediation applications, Chapter 4 discussed the idea of microgels as sorbents during the filtration process.

Chapter 4 focuses on investigating the absorption capacity of pNIPAm based microgel coatings for water remediation application. The interactions between the microgel and metal ions were studied by observing the microgel shrink/swell behavior in the metal ion solution. The metal ion concentration changes obtained from ICP-OES during the filtration reveal the absorption capacity.

## Preface

This thesis is an original work by Feng Gao under the supervision of Dr. Michael J. Serpe.

In Chapter 2 of this thesis, I was responsible for the material synthesis, data collection, and analysis. Dr. Muhammad Amirul Islam participated in the the material synthesis, experimental procedure design, data collection, and data analysis, and Jae-Young Cho participated in the characterization of the polymer materials.

In Chapter 3 of this thesis, I was responsible for the experimental design, data collection, and analysis. Dr. Muhammad Amirul Islam participated in the experimental procedure, and Jae-Young Cho participated on the characterization of the membrane and polymer materials.

In Chapter 4 of this thesis, I was responsible for the experimental design, data collection, and analysis. Varalika Tyagi participated in the experimental procedure and data collection, Nicholas Balasuriya precipitated in the microfluidic system design, and Qiming Shen and Changhao Fang precipitated in useful discussions.

## Acknowledgement

Foremost, I would like to express my deep and sincere gratitude to my supervisor, Dr. Michael J. Serpe, for giving me the opportunity to work in his laboratory and supporting me in my research by providing invaluable guidance throughout my research projects. As a great supervisor, his patience, motivation, enthusiasm, and immense knowledge inspired me to pursue our goals. His guidance helped me during the period of research and writing of this thesis. I am extremely grateful for his friendship, life advice, and the great times we shared. I could not have imagined having a better supervisor and mentor for my M. Sc. program. There is no doubt that it is my luck to have met him.

I cannot express enough thanks to my committee members, Dr. Mohtada Sadrzadeh and Dr. Ran Zhao, for their insightful comments, valuable suggestions, and constructive criticism. I would also like to thank Dr. Sadrzadeh for giving me the opportunity to work in his laboratory. I am also grateful to Jae-Young Cho for helping me with the characterization. My sincere thanks also go to Dr. Robert Jordan for his valuable suggestions and his patience in steering me from the wrong direction. In addition, I would like to express my sincere appreciation to Dr. Anna Jordan for her effort in editing this thesis and for her patient teaching on my writing.

I would like to express my thanks to all the past and current Serpe group members and all the undergraduate students who worked with me. There is no doubt that it is my luck to have worked with them. I also want to extend my gratitude to Dr. Muhammad Amirul Islam for his valuable suggestions and constructive criticism on my projects.

I am also grateful to Dr. Gregory Kiema and Dr. Yoram Apelblat for their assistance during my TA duties.

Finally, I would like to thank my parents, grandparents, and the rest of my family for their love, support, and encouragements. I would like to express my deepest gratitude to my girlfriend, Yanning Xu, who has been there for me through the tough

times and encouraged me over all the years. Thank you for standing by me all the time.  
I love you.

# Table of Content

Abstract .....	ii
Preface.....	iii
Acknowledgement.....	iv
List of Figures.....	ix
List of Tables.....	xiii
List of Abbreviations.....	xiv
Chapter 1 Introduction to Anti-fouling Filtration Membrane and Stimuli-Responsive Microgels.....	1
1.1 Background of Anti-fouling Membrane.....	1
1.2 Star-shaped Block Copolymer Coated Anti-fouling Membrane.....	3
1.2.1 Layer-by-layer Assembled Core-shell Block Copolymers.....	3
1.2.2 Thermally Stable Core-shell Block Polymers.....	5
1.3 Stimuli-responsive Polymers.....	6
1.3.1 Stimuli-responsive Hydrogels and Microgels.....	7
1.3.2 Temperature Responsive Polymers.....	8
1.3.3 PNIPAm-based Thermoresponsive Polymer.....	10
1.3.4 pH Responsive Polymers.....	11
1.4 Anti-fouling Coating with Stimuli-responsive Polymers.....	13
1.5 Water Remediation by PNIPAm Based Microgel.....	16
1.6 pNIPAm Based Microgel Synthesis.....	19
1.7 Conclusion.....	19
Chapter 2 Generation of a Highly Efficient Antifouling Coating of Silica Nanoparticle Core-Polymer Arms Star-Shaped Polymers.....	21

2.1 Introduction.....	21
2.2 Experimental Section.....	23
2.2.1 Star-shaped Polymer Synthesis.....	23
2.2.2 Membrane Preparation.....	26
2.2.3 Filtration Experiments.....	28
2.3 Results and Discussion.....	30
2.4 Conclusion.....	34
Chapter 3 Improved Anti-fouling and Self-cleaning Ability of Polyethersulfone Membranes Coated with PNIPAm-based Microgels for Oily Water Treatment.....	35
3.1 Introduction.....	35
3.2 Experimental Section.....	39
3.2.1 PNIPAm-based Microgel Synthesis.....	39
3.2.2 Stepwise-pressurized Coating.....	40
3.2.3 Oily Wastewater Filtration.....	41
3.2.4 Long-term Filtration Stability Tests.....	42
3.2.5 Self-cleaning by an Alternative Wash with Different Temperature.....	42
3.2.6 Characterization of Microgels and Membranes.....	43
3.3 Results and Discussion.....	44
3.4 Conclusion.....	59
Chapter 4 Poly (N-Isopropylacrylamide)-based Microgels as Sorbents for Pb <sup>2+</sup> , Hg <sup>2+</sup> and Cr <sup>3+</sup> Removal for Filtration Application.....	61
4.1 Introduction.....	61
4.2 Experimental Section.....	65
4.2.1 PNIPAm-based Microgel Synthesis.....	66
4.2.2 Microgel Behaviors in Solution.....	66
4.2.3 Microgel Behaviors on Au Substrate.....	67
4.2.4 Direct Absorption Experiment.....	70
4.2.5 Filtration Absorption Experiment.....	71

4.3 Results and Discussion.....	72
4.4 Conclusion.....	85
Chapter 5 Conclusions and Future Outlook.....	86
References.....	89

## List of Figures

Figure 1-1 Chemical structures of the core-shell SPs (a) PS-b-PDMAEMA (b) PS-b-PMAA. Reprinted (adapted) with permission from ref. 22. Copyright (2015) Elsevier Ltd.....	3
Figure 1-2 Procedure of layer-by-layer assembly of cationic (blue color) and anionic (red color) core-shell star block copolymers on a PSF membrane. Reprinted (adapted) with permission from ref. 22. Copyright (2015) Elsevier Ltd.....	4
Figure 1-3 Chemical structures of the core-shell SPs (a) PS-b-PDMAEMA-s-PEGMA. (b) PS-b-PMAA-s-PEGMA. Reprinted (adapted) with permission from ref. 23. Copyright (2015) Elsevier B.V.....	6
Figure 1-4 Monomer structures of typical polymers with a LCST.....	9
Figure 1-5 pH-Responsive polymers of different architectures: (a) unimer–micelle, (b) micelle reverse micelle, (c) nanogels or microgels, (d) hollow reverse hollow, (e) dendrimer, (f) hyper-branched, (g) micelle morphology changes (from worm-like to hollow), and (h) polymer brushes. Adapted with permission from Ref.47 Copyright 2017, The Royal Society of Chemistry.....	12
Figure 1-6 a) Schematic drawing of the filtration and cleaning procedure. The orange film represents the humic acid deposit, and the blue circles represent the microgels in swollen form (at 20 °C) or collapsed form (at 38 °C). Step (2) represents the first cleaning, and step (3) represents the extra cleaning procedure. b) Photographs of PES membranes after the first (first and third columns) and extra (second and fourth columns) cleaning steps. Reprinted (adapted) with permission from ref. 52. Copyright (2019) American Chemical Society.....	15
Figure 1-7 Schematic illustration of the preparation process (A–C) and the proposed	

concept of the smart membrane with functional gates for detection and removal of trace Pb <sup>2+</sup> ions (D–K). Reprinted (adapted) with permission from ref. 59. Copyright (2013) The Royal Society of Chemistry.....	18
Figure 2-1 Schematic of the synthesis of atom transfer radical polymerization (ATRP) initiator.....	24
Figure 2-2 Schematic of the immobilizing ATRP initiator onto silica nanoparticles....	24
Figure 2-3 Schematic of grafting polystyrene and poly(ethylene glycol) methacrylate onto silica nanoparticles.....	25
Figure 2-4 Schematic of flat sheet membrane preparation by blending and phase inversion technique. Adapted with permission from Ref.72 Copyright 2019, Elsevier Inc.....	27
Figure 2-5 A side view of the filtration experiment basic setup.....	28
Figure 2-6 SEM image for final star-shaped polymers.....	30
Figure 2-7 Evaluation of the blended SP membrane from representative underwater n-hexadecane captive bubble contact angles measurement. a) Bare PES membrane (M1), b) 2 w/w% star-shaped polymer-modified PES membrane, and c) 4 w/w% star-shaped polymer-modified PES membrane.....	32
Figure 2-8 Evaluation of antifouling properties against hexadecane oil-in-water emulsion .....	33
Figure 3-1 Swelling/shrinking mechanism of pNIPAm chains in microgels and illustration of the conformational change induced by temperature changes on pNIPAm based microgel particles.....	37
Figure 3-2 The permeate flux during stepwise pressurized coating for (a) MG-1, (b) NG-1, (c) NG-2, and (d) NG-3 at 2 psi (red region), 5 psi (yellow region), 10 psi (blue region), 20 psi (green region), 30 psi (orange region), 40 psi (grey region), and 50 psi (purple region).....	46

Figure 3-3 The SEM images for (a) an unmodified PES membrane and an NG-1 coated PES membrane via (b) constant pressure coating, (c) constant pressure coating, followed by drying, and (d) stepwise pressure coating followed by drying.....50

Figure 3-4 FTIR spectra of 10AAc (black), 20AAc (red), and 30AAc (blue).....51

Figure 3-5 Evaluation of the microgel coated membrane from representative underwater n-hexadecane captive bubble contact angles measurements. a) Bare PES membrane, b) 0AAc microgel coated PES membrane, c) 10AAc microgel coated PES membrane, and d) 20AAc microgel coated PES membrane.....54

Figure 3-6 Evaluation of antifouling properties against hexadecane oil-in-water emulsion using unmodified PES membrane (black), and 0AAc-(red),10AAc-(blue), 20AAc-(pink), and 30AAc-(green) coated PES membranes.....55

Figure 3-7 The SEM images for a 20AAc coated PES membrane (a) before and (b) after one-week filtration under atmosphere pressure and 30AAc coated PES membrane, and (c) before and (d) after one-week filtration under atmosphere pressure.....57

Figure 3-8 Evaluation of self-cleaning behavior with alternative 55 °C and 25 °C DI water washing for (a) an unmodified PES and (b) a 20AAc coated PES membrane. (c) The percentage flux recovery before and after alternative 55 °C and 25 °C DI water washing, followed by further 55 °C and 25 °C oil filtration cycles.....59

Figure 4-1 (a) Swelling/shrinking mechanism of acrylic molecules in microgels and illustration of the conformational change induced by pH changes on pNIPAm-co-AAc microgel particles. (b) The swelling mechanism of microgels is driven by the interaction between acrylic acid molecules and heavy metal ions.....64

Figure 4-2 (a) Schematic illustration of a typical Fabry-Pérot etalon composed of two reflective mirrors (vertical yellow lines) separated by a dielectric material with refractive index  $\eta$  and thickness of  $d$ . Incident light (black arrows) striking the etalon at an angle  $\theta$  enter its cavity and undergo multiple internal reflections where constructive and destructive interferences occur in the transmitted (T1, T2, and T3) or reflected (R1, R2, and R3) waves. (b) The structure of the microgel-based etalon device is composed of two reflective Au layers (II and IV) separated by a microgel layer (III) and constructed on a glass substrate (I).....68

Figure 4-3 (a) Representative spectra for an etalon composed of pNIPAm-co-AAc microgels (b) Peaks shift to higher wavelengths (red shift) when the microgel swells, while the peaks are shift to lower wavelengths (blue shift) when the microgel layer shrinks.....69

Figure 4-4 (a) Structure of the microfluidic device loaded with an etalon sensor in the middle (b) A side view of the etalon sensing experiment basic setup.....70

Figure 4-5 Proposed sorption mechanism for (a) electrostatic interaction between the metal ion and AAc in microgel, coordinate covalent bond between the metal ion and (b) NIPAm, and (c) BIS.....73

Figure 4-6 (a) Representative absorbance spectrum obtained of 30AAc microgel in the chromium solution with the different concentrations. The microgel diameter ratio changes along with the increasing metal ion concentration were calculated by the square root of the absorbance ratio at 400 nm for (b) Cr<sup>3+</sup>, (c) Pb<sup>2+</sup>, and (d) Hg<sup>2+</sup> .....75

Figure 4-7 (a) Representative reflectance spectrum showing a blue shift upon exposure to Cr<sup>3+</sup> solution with increase concentration. The peak shifts from different etalons made of 0AAc(black), 10AAc(red), 20AAc(green), and 30AAc(blue) along with increasing metal ion concentration for (b) Cr<sup>3+</sup>, (c) Pb<sup>2+</sup>, and (d) Hg<sup>2+</sup> .....78

Figure 4-8 Calibration curves for (a) Cr<sup>3+</sup>, (b) Hg<sup>2+</sup>, and (c) Pb<sup>2+</sup> used to quantify the amount of Cr<sup>3+</sup>, Hg<sup>2+</sup>, and Pb<sup>2+</sup> sorbed by the microgels. The straight line in each plot is a linear fit to the data using OriginLab Pro version 8.5 program software.....80

Figure 4-9 pH comparison on removal efficiency at pH at (a) 3.5 and (b) 6.5 for Cr<sup>3+</sup>(blue), Hg<sup>2+</sup>(red), and Pb<sup>2+</sup>(black). A sorbent dose of 2 mg of microgel was used in a 10 mL total volume, with 1 ppm Cr<sup>3+</sup>, 1ppm Hg<sup>2+</sup>, and 1ppm Pb<sup>2+</sup> initial concentrations of the ions.....83

Figure 4-10 Pressure comparison on removal efficiency with (a) atmosphere pressure and (b) 20 psi for Cr<sup>3+</sup>(blue), Hg<sup>2+</sup>(red), and Pb<sup>2+</sup>(black). A sorbent dose of 45.4 cm<sup>2</sup> microgel coated membrane was used in a 400 mL total volume, with 1 ppm Cr<sup>3+</sup>, 1ppm Hg<sup>2+</sup>, and 1ppm Pb<sup>2+</sup> initial concentrations of the ions.....85

## List of Tables

Table 1-1 Guidelines for Canadian Drinking Water Quality for the Above Heavy Metal Ion.....	17
Table 2-1 Chemical Compositions of Phase Inversion Membrane used for Further Experiment.....	28
Table 3-1 Hydrodynamic Diameter and Standard Deviations for the Investigated Microgels.....	45
Table 3-2 Distinctive IR Functional Groups and Their Representative Vibrational Frequencies for PNIPAm-co-AAc Microgels.....	52
Table 3-3 The NIPAm to AAc Monomer Ratios in Different AAc Composed Microgels.....	53

# List of Abbreviations

AAc: acrylic acid

APMAH: N-(3-aminopropyl) methacrylamide hydrochloride

APTES: (3-aminopropyl) triethoxysilane

APS: ammonium persulfate

ATRP: atom transfer radical polymerization

BIBB: 2-bromoisobutryl bromide

BIS: N,N'-methylenebisacrylamide

CaCl<sub>2</sub>: calcium dichloride

CrCl<sub>2</sub>: chromium(II) chloride

CrBr: copper(I) bromide

CrBr<sub>2</sub>: copper(II) bromide

DI: deionized

DEA: N,N-diethylacrylamide

DLS: dynamic light scattering

FDR: flux decline ratio

FRR: flux recovery ratio

FTIR: Fourier-transform infrared spectroscopy

HMDS: hexamethyldisilazane

HCl: hydrochloric acid

HgCl<sub>2</sub>: mercury(II) chloride

LCST: lower critical solution temperature

MAA: methacrylic acid

M12C4: methacryloyloxymethyl-12-crown-4

MIBK: methyl isobutyl ketone

NIPAm: N-isopropylacrylamide

NaOH: sodium hydroxide

PNIPAm: poly(N-isopropylacrylamide)

PS: polystyrene

PDMAEMA: poly(N,N-dimethylaminoethyl methacrylate)

PEGMA: poly(ethylene glycol) methacrylate

PES: polyethersulfone

PMAA: polymethacrylic acid

PSF: polysulfone

PVDF: polyvinylidene fluoride

PbCl<sub>2</sub>: lead(II) chloride

SPs: star-shaped block polymers

SEM: scanning electron microscope

SAGD: steam-assisted gravity drainage

SDS: sodium dodecyl sulfate

SI-ATRP: surface-initiated atom transfer radical polymerization

TEA: triethylamine

UCST: upper critical solution temperature

VCL: N-vinylcaprolactam

VPTT: volume phase transition temperature

# CHAPTER 1

## Introduction to Anti-fouling Filtration Membrane and Stimuli-Responsive Microgels

Wastewater treatment has been at the forefront of research for decades. Because of the growing concern over environmental pollution, which was brought about by rapid industrialization and household activities, new membrane technologies are emerging frequently. Since a filtration membrane needs to be used in a long-term cycle, fouling and output water quality will be considered as the biggest challenges. This chapter discusses the general background of filtration membrane, including anti-fouling treatments and heavy metal ion removal using stimuli-responsive microgels.

### 1.1 Background of Anti-fouling Membrane

Membrane technology is considered a feasible and efficient technology for seawater desalination and wastewater treatment.<sup>1</sup> Because of the high cost of inorganic membranes, modifying polymer materials to generate high-performance polymeric membranes has been one of the most vibrant areas of research in the last five years.<sup>2-3</sup> Because of the long-term operation of a membrane, fouling phenomena become the major problem in maintaining the function of a membrane. The fouling phenomena are caused mainly by the adsorption of particles, organic matter, and microorganisms on the membrane surface, or even in the pores of the membrane.<sup>4</sup> Accumulation of water contaminants on and inside the membrane leads to a cake layer of foulants on the membrane surface and blocks the structure inside the pore. This can cause a significant decline in the filtration flux and shorten the membrane lifespan.<sup>5-6</sup> This phenomenon commonly appears in the oil sand produced water treatment in Alberta (Canada). Oil sand produced water contains highly stable emulsified oil, which is one of the major foulants encountered in membrane purification processes. Membranes fouled by emulsified oil need periodic cleaning using various chemical processes, which may damage the membrane surface, increase the cleaning cost and generating further waste.<sup>7-8</sup> Oily wastewater is the major source of wastewater in the oil industry in

Alberta.<sup>9</sup> The major components of the oily wastewater are silica, total organic carbon (usually long chain alkanes), and total dissolved solid (various dissolved compounds, ions, and micro-granules).<sup>9</sup> Based on these facts, researchers have focused more on the membrane surface modification techniques to achieve the anti-fouling properties for oil emulsion wastewater treatment.<sup>10-11</sup>

Chemical grafting of functional materials on membrane surfaces has been the major direction for surface modification for anti-fouling membranes<sup>12-13</sup> since the fouling phenomenon is caused mainly by the hydrophobic–hydrophobic interactions between oil molecules and the membrane. The grafted materials are primarily used for anti-fouling membrane fabrication in oily wastewater treatment, which usually are hydrophilic or charged molecules that can provide hydrophilic and electrostatic interactions between the water constituents and the membrane in order to avoid the hydrophobic–hydrophobic interaction between oil and membrane. Although chemical grafting is considered as an effective way to make anti-fouling membranes, there are still some disadvantages. The major drawback is the limited compatibility of the membrane because the grafting process requires an expensive or destructive process, which influences the permeation properties if the reaction is not controlled properly.<sup>14</sup> Moreover, the grafting materials can be separated from the membrane surface after long-term operation, which also causes an unstable product quality and an increased cost for filtration. Chemical coating needs covalent bonds to fabricate hydrophilic materials on the membrane surface while the physical coating does not. Physical coating only needs intermolecular forces, like hydrophobic-hydrophobic interaction, to fabricate anti-fouling materials on the membrane surface

Physical coating processes can offer controlled anti-fouling properties on membranes without affecting the permeation properties if the material is designed properly.<sup>15</sup> Compared with chemical grafted membranes, a physical coated membrane does not need an expensive or destructive grafting chemical material process on the membrane surface. Physical coating processes can be controlled more easily than chemical reactions on a membrane surface. Polyelectrolytes commonly are used as coating materials for anti-fouling membranes.<sup>16-17</sup> Linear polyelectrolytes,<sup>17</sup>

hyperbranched polyelectrolytes,<sup>18</sup> charged inorganic materials,<sup>19</sup> carbon nanotubes,<sup>20</sup> and graphene oxide<sup>21</sup> are used for fouling resistance. However, these materials also have limitations in the stability of the coatings, membrane reactivations, and increased membrane surface roughness, which may cause the aggregation of the coating material.

## 1.2 Star-shaped Block Copolymer Coated Anti-fouling Membrane

Recently, a new type of anti-fouling coating material, star-shaped block copolymers (SPs), was introduced as a physical coating material for membrane modification processes.<sup>22-23</sup> These types of materials can contain both hydrophobic and hydrophilic components at the same time. The hydrophobic part increases the coating stability to maintain the coating on the membrane surface after a long-term operation. The hydrophilic part offers highly anti-fouling properties during the oily water filtration process.

### 1.2.1 Layer-by-layer Assembled Core-shell Block Copolymers

In 2016, Diep et al. designed a star-shaped block copolymer, which consists of a hydrophobic polystyrene (PS) core and a charged hydrophilic poly (N,N-dimethylaminoethyl methacrylate)(PDMAEMA) or polymethacrylic acid (PMAA) arms.<sup>22</sup> SPs were coated on a commercial polysulfone (PSF) membrane using a layer-by-layer self-assembly method. The modified membrane exhibits high anti-fouling properties against model wastewater pollutants, including dyes, bovine serum albumin, humic acid, and oil emulsion.

As shown in Figure 1-1, SPs consist of a hydrophobic PS core and hydrophilic PDMAEMA or PMAA arms.

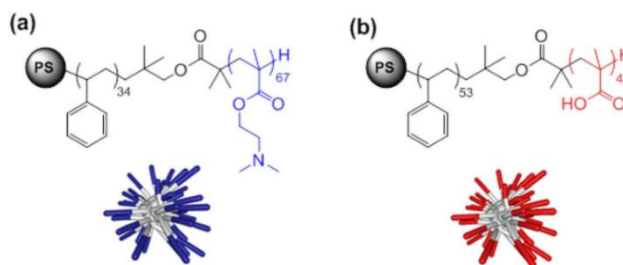


**Figure 1-1.** Chemical structures of the core-shell SPs (a) PS-b-PDMAEMA (b) PS-b-PMAA. Reprinted (adapted) with permission from ref. 22. Copyright (2015) Elsevier Ltd.

These SPs show high coating stability on the membrane surface due to the hydrophobic–hydrophobic interaction between the hydrophobic PS core and inner arms and the hydrophobic membrane surface. In addition, an electrostatic interaction between the cationic arms on SPs and a partially negatively charged membrane surface also provides a high coating stability. Because of the high density of hydrophilic arms, high anti-fouling properties can be achieved with a thin layer of SP coating on the membrane surface.

To coat SPs on a hydrophobic membrane surface, the first monolayer coating contained PS-b-PDMAEMA, which contains cationic arms. Due to the electrostatic force between the cation arms on SPs and the partially negatively charged membrane, the PS-b-PDMAEMA star-shaped block copolymer will have additional coating stability, along with the hydrophobic–hydrophobic interaction of the PS core and the membrane material. Although cationic SPs can bond strongly on the membrane surface, the monolayer coating with amine groups is not suitable to provide appreciable anti-fouling properties since positive charges can attract abundant negatively charged foulants, like humic acid. Therefore, another layer of anionic SPs is needed to improve the anti-fouling performance, as shown in Figure 1-2.

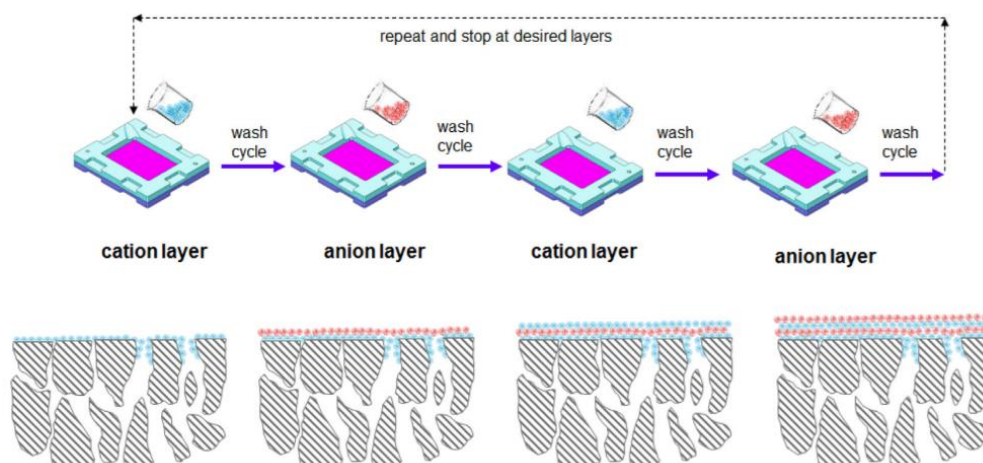


**Figure 1-2.** Procedure of layer-by-layer assembly of cationic (blue color) and anionic (red color) core-shell star block copolymers on a PSF membrane. Reprinted (adapted) with permission from ref. 22. Copyright (2015) Elsevier Ltd.

PS-*b*-PMAA star-shaped block copolymers are modified as a second anti-fouling layer on the membrane surface. Due to the electrostatic force between cationic and anionic SPs, the second layer of anionic SPs also have a strong interaction with the first layer of cationic SPs, creating a much more stable coating for long-term operation.

This layer-by-layer coating strategy offers a thin and defect-free anti-fouling separation layer. The number of deposited layers determines the permeability and selectivity for the desired membrane.<sup>24-25</sup> The surface potential and morphology also can be tuned by this technology.<sup>26</sup> This strategy can reduce the water flux through the membrane significantly and commonly is used to prepare nanofiltration membranes.<sup>27</sup> Although this coating strategy offers both stability and high efficiency, this processes often requires a postdeposition treatment that is not used widely in large scale membrane modifications.<sup>28-29</sup>

Another technological challenge is the development of thermally stable membranes. For example, in a steam-assisted gravity drainage (SAGD) process, which is a thermally enhanced heavy oil recovery method for the extraction of bitumen in Alberta, water is typically 70 to 95 °C.<sup>30</sup> Degradation of the coating material on membranes at higher temperatures also can be a major problem in using this technology in oil sand industry.

### **1.2.2 Thermally Stable Core-shell Block Polymers**

The SPs with pure charged hydrophilic arms show low stability during high temperature filtration because of the high charge density on the SPs arms. Based on the electron repulsion force on the SPs arms, hydrophilic arms are not stable enough to maintain anti-fouling properties at higher temperature. Some of the hydrophilic arms degraded, and the remaining hydrophobic core increased the surface roughness and caused more foulant on the membrane surface.

To address the issues associated with water permeability, anti-fouling properties, and thermal stability, B. Soltannia et al. used uncharged hydrophilic poly(ethylene glycol) methacrylate (PEGMA) associated with charged molecules PDMAEMA and PMAA as the hydrophilic arms of the SPs.<sup>23</sup>

Figure 1-3 shows the improved SP structure. SPs consist of a hydrophobic PS core and hydrophilic arms. Hydrophilic arms are a statistical copolymer consisting of charged monomers (PDMAEMA or PMAA) and highly hydrophilic neutral-charged PEGMA. PEGMA can improve the thermal stability of SPs and maintain the high quality of anti-fouling performance at the same time.

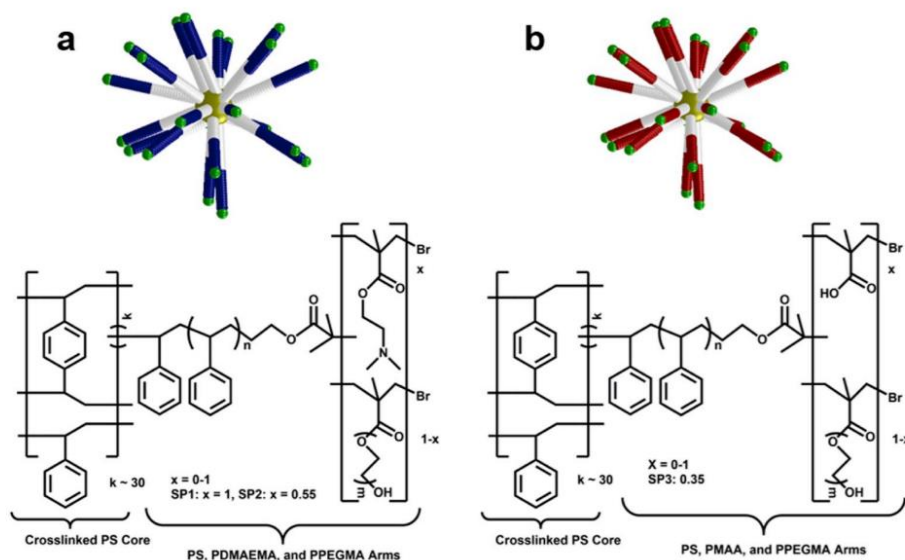


**Figure 1-3.** Chemical structures of the core-shell SPs (a) PS-b-PDMAEMA-s-PEGMA. (b) PS-b-PMAA-s-PEGMA. Reprinted (adapted) with permission from ref. 23. Copyright (2015) Elsevier B.V..

Their result imply that the interaction between star-shaped copolymers and hydrophobic membranes are strong enough to be used for high-temperature filtration. The thermal and chemical stability of the coating could be improved further by changing the core/arm material. For example, silica-based core polymer-based arms can be used because of the high thermal stability for silica nanoparticles. Chapter 2 discusses a new type of silica core-polymer arms star-shaped polymer nanoparticles and its performance as an anti-fouling coating on PES membrane for oily water filtration.

### 1.3 Stimuli-responsive Polymers

Stimuli-responsive polymers are macromolecules that can exhibit dramatic changes in response to an external environment change. When the polymers in the crosslinked

networks are hydrophilic, they form hydrogels. Due to the hydrophilic nature, hydrogels are used widely as antifouling coatings on filtration membrane surfaces. This chapter discusses the general background of stimuli-responsive polymers with N-isopropylacrylamide (NIPAm) monomers.

### 1.3.1 Stimuli-responsive Hydrogels and Microgels

Hydrogels are composed of hydrophilic polymers that are chemically and/or physically crosslinked into insoluble, yet hydrophilic structures. They can absorb and retain water in their three-dimensional structure up to a thousand times of their dry weight in the aqueous environment without dissolution because of the hydrophilic functional group in the monomer or crosslinker of hydrogels. Hydrogels also show porous structures, allowing other chemicals to be transported in/out of their matrix.<sup>24</sup>

Hydrogels can be designed to respond to small environmental changes with a sharp transition of their transition ratio, which is defined as the mass of water absorbed per gram of a hydrogel matrix. The equilibrium swelling state of hydrogels immersed in a suitable solvent is obtained when there is a thermodynamic equilibrium between the solvent inside and outside the hydrogel following the Flory–Rehner (F–R) theory.<sup>25</sup> The F–R theory assumes that the enthalpy of mixing promotes swelling, while the elastic forces imposed by the crosslinked chains in the matrix promote contraction. When a hydrogel is soaked in water, osmotic pressure drives the water molecules to diffuse into the hydrogel matrix, causing expansion of the hydrogel. Since the flexible polymer chains are held together by crosslinkers, the chain expansion can be countered by an elastic restoring force. The equilibrium can be reached when the two forces are balanced.

$$\Delta G_{\text{total}} = \Delta G_{\text{elastic}} + \Delta G_{\text{mixing}} \quad (1-1)$$

Equation 1-1 shows the basic principle of F–R theory, where  $\Delta G$  is the Gibbs free energy. When the external stimuli interrupt the balance between chain expansion and elastic restoring force, the hydrogel will adapt to the new environment by alternating its swelling ratio, which can result in a stimuli-responsive property. This behavior can be obtained both with physical (temperature, light, electric field, magnetic

field) and chemical (pH, salt, biomolecules) stimuli. According to their different solvation states, hydrogels can change their chain conformation, mesh sizes, and refractive index reversibly.<sup>26-28</sup>

The speed of the response is an important factor for stimuli-responsive hydrogels in real-world applications. Equation 1-2 reveals a theory proposed by Tanaka and Fillmore in 1979.<sup>29</sup>

$$\tau = R^2/\pi^2D \quad (1-2)$$

The characteristic time ( $\tau$ ) for a hydrogel's volumetric change is directly proportional to the square of the gel size  $R$  and inversely proportional to the diffusion coefficient ( $D$ ). To minimize the response time of a hydrogel, hydrogels with submicron dimensions (microgels) have been developed. Combining the advantages of colloidal particles and stimuli-responsive microgels yields a high surface-to volume ratio, colloidal stability, good water absorption, proper elasticity, porous structure, and fast stimuli responsivity. Microgels are used widely in superabsorbent materials, miniaturized devices, emulsion stabilizers, and anti-fouling coatings.<sup>30-32</sup>

### 1.3.2 Temperature Responsive Polymers

Temperature responsive polymers can be separated into two main groups, depending on different temperature-dependent behaviors. One category deswells upon heating, exhibiting a lower critical solution temperature (LCST). The other category swells upon heating, exhibiting an upper critical solution temperature (UCST).

Hydrogels exhibiting an LCST behavior, generally carry both hydrophobic and hydrophilic groups. Many monomers have been developed to making hydrogels with an LCST, for example, N-isopropylacrylamide (NIPAm), N-vinylcaprolactam (VCL), and N,N-diethylacrylamide (DEA).<sup>33-35</sup> Figure 1-4 shows the chemical structure of the monomer stated above. Of the various stimuli-responsive polymers, poly(N-isopropylacrylamide) (pNIPAm), discovered in 1968<sup>36</sup>, has emerged as the most popular one over the past few decades. PNIPAm has been studied widely because of its volume phase transition temperature (VPTT) at around 32° C, which is near the range of physiological relevance. VPTT is defined as the temperature at which the degree of swelling changes dramatically. Specifically, below this temperature, pNIPAm exists in

the extension state, forming a random coil; above this temperature it exists in the collapsed state, forming a globular conformation.

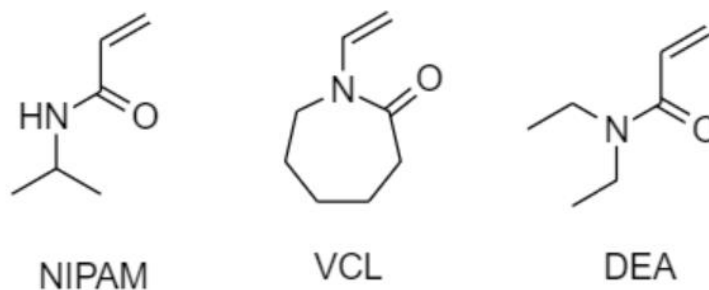


**Figure 1-4.** Monomer structures of typical polymers with a LCST.

Single chain pNIPAm has been studied to explain this temperature-dependent phase transition behavior in polymers using the Gibbs free energy equation below:

$$\Delta G = \Delta H - T\Delta S \quad (1-3)$$

where  $G$  is the Gibbs free energy for dissolution,  $H$  is the enthalpy,  $S$  is the entropy change caused by the interaction between solvent (typically water) and polymer chains, and  $T$  is the temperature of the system. If  $\Delta G$  is negative, the polymer dissolution is spontaneous. If  $\Delta G$  is positive, the polymer deswells and is insoluble in the solvent.

Since pNIPAm has both hydrophobic isopropyl groups and hydrophilic amide groups, the LCST response of pNIPAm (and other similar polymers, like poly(N,N-diethylacrylamide)) is due to the balance of the entropic and enthalpic contributions to solvate these groups. At a temperature below LCST, pNIPAm chains have two different strong interactions with water molecules: one is the hydrogen bond from the amide group and the other one is the clathrate-like repulsion force from the hydrophobic isopropyl groups and polymer hydrocarbon backbones.<sup>33,37</sup> Based on this, negative  $\Delta H$  and  $\Delta S$  values can be observed because this hydration state is not endothermic (does not need external heat energy to activate it) and is more disordered in the system. Between these two forces, the enthalpy effect is dominant at low temperatures, resulting in a negative  $\Delta G$  value and a spontaneous hydration process. As the temperature rises above the LCST, the hydrophobic groups interact with each other in the polymer, and

the hydrophilic groups also form hydrogen bonds with each other. Positive  $\Delta H$  and  $\Delta S$  values can be observed because this dehydration process is endothermic (needs external heat energy to activate it) and is more ordered in the system. However, at high temperatures, the entropy term becomes dominant, resulting in a positive  $\Delta G$  value and an unfavorable dehydration process.

Based on the above theory, the temperature-induced transition from a soluble state to an insoluble state can occur. At temperatures above LCST, the transition from the polymer–water interactions to polymer–polymer interactions forces hydrogels to collapse by squeezing out the water they absorbed.

LCST is the unique temperature of a type of polymer composed of a single type of monomer. There are several factors that can influence the LCST for a polymer network. For example, LCST can rise by adding more hydrophilicity into the hydrogel polymer backbone, while more hydrophobicity will cause a lower LCST.<sup>38</sup> Beside backbone hydrophilicity, the co-solvent, the polymers' crosslinking density, its molecular weight, and its architecture can influence the LCST of a polymer.<sup>39-41</sup>

### **1.3.3 PNIPAm-based Thermoresponsive Polymer**

pNIPAm is the most well-known thermoresponsive polymer. Free radical polymerization generally is used to synthesize the pNIPAm based microgel by simply mixing monomer, initiator, and crosslinkers together in an aqueous solution and reacting them at high temperature. Ammonium persulfate is a typical initiator used at high temperature to generate free radicals to initiate the whole polymerization process. N,N'-methylenebisacrylamide (BIS) is the most commonly used crosslinker in pNIPAm based microgels because of its similar structure with NIPAm. pNIPAm-based microgels can form colloidally stable particles with size ranges from 100 nm to 1  $\mu\text{m}$ . Compared with the bulky counterparts, pNIPAm-based microgels are able to retain the temperature responsive property with a high water absorption ratio, but they also have a much faster response because of their smaller size.

pNIPAm-based microgels can be designed to respond to different stimuli by adding various functionalized comonomers during the polymerization. For example, charged molecules can be added to provide a pH response, metal ion chelate molecules

can be added to provide a metal ion response, and light-responsive molecules can be added to provide a light response. Beside functional groups, it also is easy to change the morphology of microgels to have a hollow or core-shell structure.<sup>42-44</sup>

### 1.3.4 pH Responsive Polymers

pH responsive hydrogels are polyelectrolyte gels that bear ionizable moieties in their backbone. The swelling ratio of polyelectrolyte gels can be significantly higher than the neutral-charged gels because of the Coulombic repulsion between fixed ionic groups and the additional osmotic pressure from mobile counterions. Some ionic monomers, such as acrylic acid (AAc), methacrylic acid (MAA), and N-(3-aminopropyl) methacrylamide hydrochloride (APMAH), can work as a copolymer during the microgel polymerization.

The most used monomer in this thesis is AAc, which has a  $pK_a$  of  $\sim 4.25$ . The pH-induced volume transition of weak PEs generally occurs in a pH range close to the  $pK_a$  of their ionizable moieties because their degree of ionization is different at different pH values. As a result, pNIPAm-co-AAc microgels are neutral-charged when  $pH < 4.25$  and negatively charged when  $pH > 4.25$ . At  $pH > 4.25$ , the carboxylic groups in AAc are deprotonated. The negative charge from the carboxylic groups in the microgel will drive the whole gel to expand. If NaOH is used to modify the pH, sodium ions are also trapped in the microgel, also causing the expansion of the whole network. With the same principle, at  $pH < 4.25$ , the carboxylic groups in AAc are protonated. The electron repulsion force does not exist within the microgel, and this causes the collapse of the whole gel network.

There are several parameters that influence the pH response of this type of polymer. The crosslinking density, hydrophilicity, and hydrophobicity of the polymer chains can influence the sensitivity of the pH response behavior. Ionic strength also can influence the pH response property by ion interference.<sup>45</sup> Keeping other parameters constant, at lower ionic strength, the solution pH (concentration of  $H^+$ ) is the dominant parameter that causes the swelling of the gels. At medium ionic strength, protons from the carboxylic group exchange with the metal ion from the salt, causing increased swelling behavior. At high ionic strength, Debye screening will dominate, and the

whole gel will deswell.<sup>46</sup>

Changing the morphology of the pH responsive polymer can give the polymer a new behavior to fit different demands. A pH response polymer can be linear, branched or have a crosslinked network, as shown in Figure 1-5.

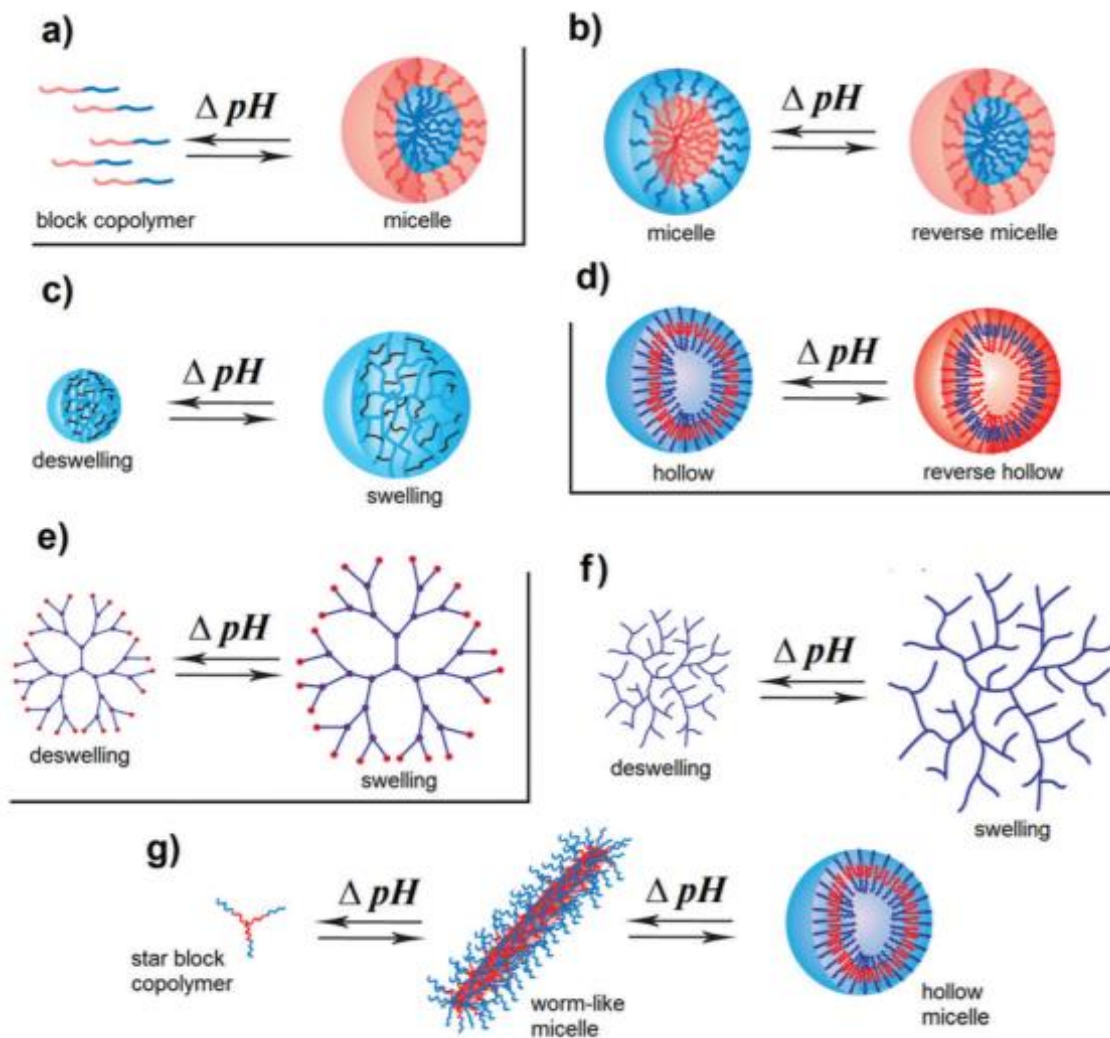


**Figure 1-5.** pH-Responsive polymers of different architectures (pH increase from left to right and pH decrease from right to left): (a) unimer–micelle, (b) micelle reverse micelle, (c) nanogels or microgels, (d) hollow reverse hollow, (e) dendrimer, (f) hyper-branched, (g) micelle morphology changes (from worm-like to hollow). Adapted with permission from Ref.<sup>47</sup> Copyright 2017, The Royal Society of Chemistry.

Their responses to pH, as well as their structural organization, may differ. For example, a pH change can cause protonation/deprotonation of functional groups in a polymer network; it also can cause the precipitation, flocculation, and chain collapse-

extension. The same pH change can result in self-assembly, swelling, and deswelling.<sup>47</sup> Architectures such as block copolymers, branched copolymers, and star copolymers with a pH responsive block respond in some defined ways to the pH of the solution. The changes observed in polymers of different architectures by the pH change of the solution are shown in Figure 1-5.

## **1.4 Anti-fouling Coating with Stimuli-responsive Polymers**

The hydrophilic nature of pNIPAm based polymers makes them useful as an anti-fouling coating in oily wastewater treatment. Surface modification of hydrophobic membranes by means of hydrophilic polymers is preferred. Fouling can be reversible or irreversible. Different cleaning methods can eliminate reversible fouling and recover original flux. Physical cleaning methods are effective at limiting reversible fouling, such as backwashing and air flush. However, physical cleaning methods require additional mechanical processes, which increase the cost for the cleaning process significantly. Chemical cleaning methods, including the use of some chemical agents, like surfactants, can damage the membrane, creating a rougher surface; this can cause more fouling on the membrane surface. The demand for a coating would be both to decrease membrane fouling during oily wastewater treatment and to provide a facile and effective cleaning method to eliminate reversible fouling. A pNIPAm based polymer is the perfect material to achieve this goal. Because of its hydrophilic stimuli responsive property, a modified antifouling membrane can show both an anti-fouling property and a self-cleaning behavior by changing the external environment. There are many ways to modify pNIPAm based polymers on the hydrophobic membrane surface with a different morphology of pNIPAm based polymers.

S. Pourziad et al. used a surface-initiated atom transfer radical polymerization (SI-ATRP) method to graft pNIPAm and PEGMA on the polyvinylidene fluoride (PVDF) membrane. pNIPAm (lower block) was grafted to give the membrane a temperature responsive property in order to provide the membrane with an anti-fouling property and self-cleaning behavior. PEGMA (upper block) was grafted to further improve the anti-fouling property for the membrane since PEGMA is a hydrophilic polymer and can enhance the anti-fouling property. Their results showed that the

pNIPAm-b-PEGMA modified membrane had a 64% decrease in fouling ratio compared to the unmodified PVDF membrane.<sup>48</sup> Although grafting a polymer chain on the surface of the membrane is effective to achieve the anti-fouling and self-cleaning behavior, SI-ATRP still needs a complex polymerization process to react polymers on the membrane. This reaction should be operated under argon and requires CuBr as a catalyst, which can cause problems during the purification process, significantly increasing the synthesis cost. That is the main reason that the SI-ATRP process is not used widely in large scale membrane surface modification.

To avoid a complex polymerization process directly on the membrane surface, an inorganic material grafted temperature response polymer can be used as an anti-fouling and self-cleaning coating for oily wastewater filtration. Silica nanoparticles have been applied widely in modifying PVDF membranes because of their facile operation, good hydrophilicity, and excellent thermal and mechanical stability.<sup>50</sup> Although the silica nanoparticle modified PVDF membranes improved anti-fouling and permeability, the smart self-cleaning for dynamically reversible foulant cannot be achieved further. Y. Zhao et al. developed pNIPAm grafted silica nanoparticles to achieve the anti-fouling and self-cleaning behavior. Atom transfer radical polymerization (ATRP) is used to synthesize the nanoparticle. The developed nanoparticle coated PVDF membrane showed enhanced flux recovery and decreased values in irreversible fouling ratio compared with the bare PVDF membrane.

Compared to silica core-polymer shell nanoparticles, pure pNIPAm based microgels have a higher volume change ratio and a better swell-shrink behavior, driving a better self-cleaning performance on the fouled membrane surface. C. Aksoy et al. used temperature responsive microgels in a foulant cake layer and cleaning it by stimuli-induced size changes of the microgels to remove the foulant on the polyether sulfone (PES) membrane surface,<sup>51</sup> as shown in Figure 1-6.

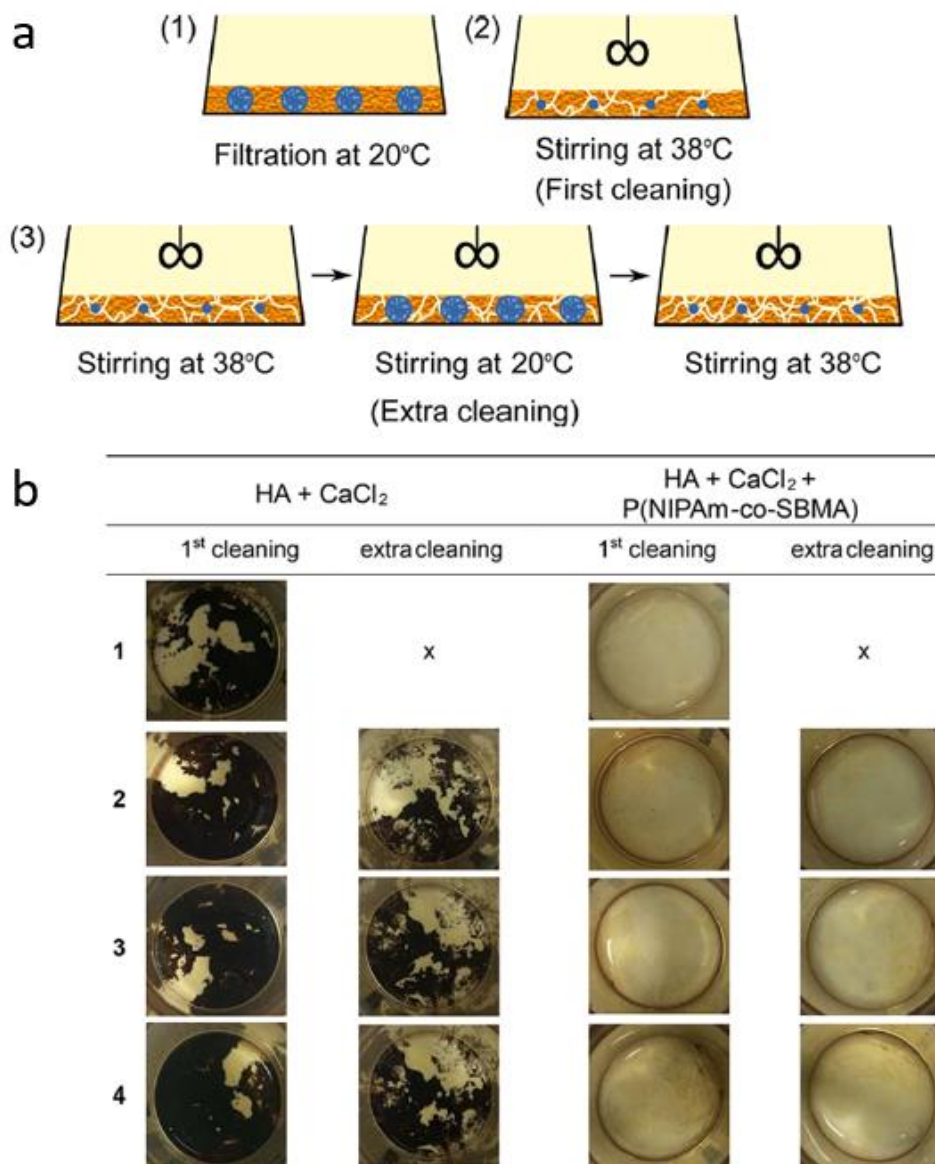


**Figure 1-6.** a) Schematic drawing of the filtration and cleaning procedure. The orange film represents the humic acid deposit, and the blue circles represent the microgels in swollen form (at 20 °C) or collapsed form (at 38 °C). Step (2) represents the first cleaning, and step (3) represents the extra cleaning procedure. b) Photographs of PES membranes after the first (first and third columns) and extra (second and fourth columns) cleaning steps. Reprinted (adapted) with permission from ref. 52. Copyright (2019) American Chemical Society.

pNIPAm based microgels were co-deposited in the feed solution with foulant humic acid and CaCl<sub>2</sub> during filtration, causing the cake on the membrane surface to reduce the water flux. The temperature stimuli response of the microgel extended the distances from the membrane surface; this can remove the thick foulant deposits on the membrane surface. Co-depositing pNIPAm based microgels also showed high fouling

reversibility when a temperature was applied.

In Chapter 3, anti-fouling and self-cleaning properties will be discussed with step pressurized pNIPAm-co-AAc microgel coating on PES membrane.

## **1.5 Water Remediation by PNIPAm Based Microgel**

One of the major problems facing the 21<sup>st</sup> century is the lack of clean drinking water. More than a third of the world's population lacks clean drinking water.<sup>52</sup> Growing urbanization and industrialization demands more effective water remediation technologies to avoid releasing pollutants into the environment. There is unqualified wastewater quality mainly because the wastewater contains excess heavy metals and other organic pollutants. Although the exact impact of pollutants on the prevalence of disease is unknown, about 70–90 % of disease risks are due to changes in the environment.<sup>53</sup> In this regard, researchers are putting more resources into water remediation technologies. Most of the pollutants are not biodegradable; as they are transported through the food chain, human beings can be the ultimate victims. Heavy metal ions are a huge part of the pollutants from industrial wastewater; most of them are toxic or carcinogenic for human beings.

Mercury is a neurotoxin, capable of causing damage to the central and peripheral nervous systems.<sup>54</sup> The inhalation of mercury vapor can result in harmful effects on the nervous, digestive, and immune systems, lungs, and kidneys, and may be fatal. High mercury concentrations result in impairment of kidney function, chest pain, and dyspnea.

Lead is the most common heavy metal pollutant in battery industrial wastewater. Human exposures occur through inhalation of contaminated dust particles and aerosols or by ingesting contaminated food and water. Lead poisoning in humans damages the kidneys, liver, heart, brain, skeleton, and the nervous system. The initial symptoms of poisoning associated with exposure to lead may include headache, dullness, memory loss, and irritability. Lead poisoning may cause disturbance of hemoglobin synthesis and anemia.<sup>55</sup>

Chromium is used widely in metallurgy, electroplating, and in the manufacturing of paints, pigments, preservatives, pulp, and papers, among others. The

introduction of chromium into the environment is often through sewage and fertilizers. The adverse health effects that are associated with mercury and mercuric compounds in humans includes possible carcinogens; damage of the brain, lungs, and kidneys; damage of developing fetuses; high blood pressure or heart rate; vomiting and diarrhea; skin rashes and eye irritation.<sup>56</sup> The guidelines for Canadian water quality for the above metal ions are given in Table 1-1. Data obtained from Health Canada, Guidelines for Canadian Drinking Water Quality—Summary Table; Water and Air Quality Bureau, Healthy Environments and Consumer Safety Branch, Health Canada, Ottawa, Ontario.

**Table 1-1.** Guidelines for Canadian Drinking Water Quality for the Above Heavy Metal Ions

Heavy metal ion	Maximum acceptable concentration (mg/L)
Mercury	0.001
Lead	0.005
Chromium	0.05

With stringent regulations in place, it is necessary to develop strategies for removing and reusing these heavy metals. Different remediation strategies have been explored over the years, such as chemical precipitations, membrane filtration, ion exchange, flotation, electrochemical treatment, and adsorption.<sup>57</sup> pNIPAm-based microgels can be designed to be used in the water remediation process. The electron donor atoms in the microgel can donate the free pair of electrons to the empty d or f orbitals in the heavy metal ion. Beside the pNIPAm itself, other functional groups, such as carboxylic acid and crown ethers, also can be introduced into the microgel to be more effective absorbents for removal of heavy metal ions.

Y. S. Kim et al. developed lithium ion ( $\text{Li}^+$ ) selective pNIPAm based hydrogels to extract  $\text{Li}^+$  from wastewater.<sup>58</sup> They used methacryloyloxymethyl-12-crown-4 (M12C4) functional groups, which have a high selectivity and sensitivity for  $\text{Li}^+$ , as a copolymer during the hydrogel synthesis. The hydrogel droplets show 89%  $\text{Li}^+$  adsorption efficiency, with a high selectivity among several different metal ions from

artificial wastewater and a maximum adsorption of 1.4 mg  $\text{Li}^+$  per g hydrogel achieved within 20 min.<sup>58</sup>

pNIPAm based polymers show high efficiency and selectivity in removing metal ions from wastewater, a process that also is considered as a separation process. This metal ion absorption process can be coupled with a membrane filtration process to enhance the membrane separation performance further. A pNIPAm based polymer to detect and remove trace lead ions ( $\text{Pb}^{2+}$ ) was developed by Z. Liu. Poly(N-isopropylacrylamide-co-acryloylamidobenzo-18-crown-6) copolymer chain is grafted on nylon-6 membranes. Figure 1-7 shows the detecting and removing mechanism.<sup>59</sup>

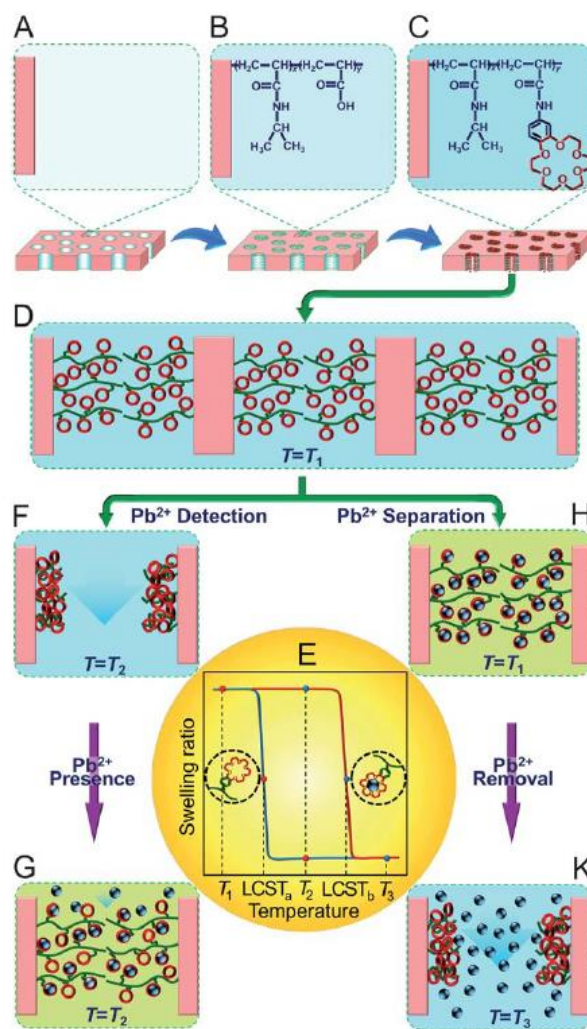


**Figure 1-7.** Schematic illustration of the preparation process (A–C) and the proposed concept of the smart membrane with functional gates for detection and removal of trace  $\text{Pb}^{2+}$  ions (D–K). Reprinted (adapted) with permission from ref. 59. Copyright (2013) The Royal Society of Chemistry.

## 1.6 PNIPAm Based Microgel Synthesis

Different methods have been developed to fabricate pNIPAm microgels.<sup>60,61</sup> Free-radical precipitation polymerization is the method most used, and the process will be discussed next in detail. To synthesize pNIPAm microgels, a solution containing NIPAm, comonomers and BIS is purged with N<sub>2</sub> to remove O<sub>2</sub> and allowed to heat to a temperature which is far above pNIPAm's LCST (45–70 °C), over ~1 h. Then, a solution of APS is added to initiate polymerization. The resulting suspension is filtered to remove any large aggregates and purified via centrifugation. In addition, by adding a surfactant such as sodium dodecyl sulfate (SDS), the microgel's diameter can decrease since SDS helps stabilize microgels at smaller sizes. Free-radical precipitation polymerization has been shown to be advantageous since the size distribution of as-prepared microgels is narrow, and the structure of the particles can be tuned easily. A key prerequisite for the success of this approach is that the monomer can be dissolved in water, while the corresponding polymer is insoluble in water at high temperatures. As shown in Figure 1-4, at high temperatures, APS will decompose and form radicals to react with monomers and crosslinkers to initiate polymerization. Since pNIPAm has an LCST, above a critical length, growing pNIPAm chains will collapse and form precursor particles, which serve as nuclei for particle growth. That is, these precursor particles are not colloidally stable and can coalesce; furthermore, the NIPAm monomer also can deposit onto the surface of the particles. Eventually, they form stable microgels. Since the reactivity for BIS is higher than for the NIPAm monomer, the structure of pNIPAm microgels is not homogeneous and they have higher crosslinking density at the cores compared to their shells.

## 1.7 Conclusion

In this chapter, we introduced star-shaped polymers and stimuli-responsive polymers, some concepts and applications of the temperature-responsive hydrogels and microgels, some concepts of the anti-fouling and water remediation systems based on stimuli-responsive polymers. There are different formations and mechanisms that utilize hydrophilic polymers in anti-fouling and water remediation systems e.g., star-shaped polymer coating, grafted polymer chains, and microgel coating. However, for a star-

shaped polymer and microgel coating anti-fouling system, the coating stability is still a challenge. The hydrophilic nature and charge repulsion caused an unstable coating and decline of anti-fouling for star-shaped polymer and microgel coatings during oily wastewater treatment and washing process.

In this thesis, we will discuss some anti-fouling and water remediation approaches that can provide high stability. Specifically, star-shaped polymer with a silica core was used to prepare the anti-fouling membrane. Although some previous works have been done to develop an anti-fouling coating using hydrophobic polystyrene core star-shaped polymer, we will discuss silica core star-shaped polymers composed membranes and investigated their anti-fouling property with oily wastewater. Then, pNIPAm-based microgels were used to prepare anti-fouling membranes, and we used them as anti-fouling coating and investigated their coating ability with different microgel sizes and coating procedures, anti-fouling properties with different monomer compositions, and coating ability among long-term operations. Although microgel coatings have been reported with high anti-fouling properties, the coating stability is still the biggest challenge. In this thesis, we will discuss the preparation of a pNIPAm-based microgel coated membrane with optimized coating stability and anti-fouling properties by tuning the microgel sizes, compositions, and coating processes. At the same time, the microgel coating was also investigated for water remediation among heavy metal ions. The behaviors of microgels with different compositions will be discussed among three different metal ions,  $\text{Pb}^{2+}$ ,  $\text{Hg}^{2+}$ , and  $\text{Cr}^{2+}$  in solution. The metal ion removal will be further discussed for water remediation application during a filtration process.

This thesis will mainly focus on the methodologies of preparing an optimized coating for membrane with high stability, anti-fouling properties, and metal ion removal behavior, which will provide some new ideas to benefit the wastewater treatment for a better performance.

## CHAPTER 2

### Generation of a Highly Efficient Antifouling Coating of Silica Nanoparticle Core-Polymer Arms Star-Shaped Polymers

This chapter describes how silica core-polymer arm star-shaped polymers have been synthesized and characterized. Anti-fouling membranes have been made by blending the star-shaped nanoparticles with the membrane solution before the phase inversion process. Their antifouling properties were characterized via constant flux filtration, with an oil-in-water emulsion. The filtration flux was recorded during the filtration, and the flux decline illustrates the degree of fouling on the membrane surface and inside the membrane. At the end, the flux recovery after washing was used to indicate the reversibility of the foulant on the anti-fouling membrane surfaces.

#### 2.1 Introduction

Inorganic materials have better thermal stability than pure organic materials. Silica nanoparticles have been used previously for surface modification of filtration membranes because of their hydrophilicity, widespread availability, and low cost.<sup>62-65</sup> Various functionalized silica nanoparticles have been studied as an anti-fouling coating on different types of membranes. For example, amine-functionalized silica nanoparticles were grafted on the nanofiltration membrane surface to give high hydrophilicity and anti-fouling properties,<sup>66</sup> a super hydrophilic silica layer was grown on a membrane substrate to have anti-fouling properties,<sup>64</sup> and a type of zwitterionic silica-based nanogels was copolymerized on a polysulfone membrane to have highly efficient anti-fouling properties.<sup>67</sup> The silica-modified membranes demonstrated exceptional anti-fouling properties against a variety of oil-in-water emulsions containing various pollutants. The flux recovery ratio for silica-modified membranes can be very high after several cycles of wastewater filtration.

Coating silica-based materials on membrane surfaces can be accomplished via various methods, including grafting, covalent bonding, surface mineralization, and

layer-by-layer assembly to tune the membrane permeability, hydrophilicity, surface roughness, and delay membrane fouling without changing the intrinsic membrane structure.<sup>68</sup> For example, a layer of silver chloride was deposited on a membrane surface by applying surface mineralization technique on the membrane, which is an alternate soaking process, to improve the fouling resistance and water flux recovery.<sup>69</sup>

Although inorganic nanomaterial coating methods have been utilized extensively to improve the anti-fouling performance, the techniques still need a complex coating process, large quantities of material, and/or several extra treatment steps with exceptionally challenging operating conditions. These extra coating processes limited their scalability. Moreover, bare inorganic nanoparticles are not directly compatible with hydrophobic membranes, like polysulfone (PSF) and polyethersulfone (PES), by physical deposition because of the lack of interactions between inorganic material and membrane.

There are two strategies to modify inorganic material on a hydrophobic membrane surface. A charged polyelectrolyte can be modified on the inorganic nanoparticles to have hydrophobic–hydrophobic interaction between the coating material and the membrane. Or the coating material itself can be self-assembled with charge modified membrane surface. These coating strategies are also mainly based on electrostatic interaction and largely depend on the nature of the membrane, such as its surface potential and functional groups, which often require surface activation or post-deposition treatment.<sup>70-71</sup> In order to address the issue associated with water permeability, anti-fouling properties, and thermal stability of oily wastewater filtration membranes, silica core-polymer arm nanoparticles have been designed as an anti-fouling coating on the hydrophobic membrane surface

In this chapter, an effective modification approach to fabricate silica core-polymer arm star-shaped polymer nanoparticles modified PES membranes was designed. The reaction schemes are discussed in the experimental section of this chapter. The material synthesis was done by me and Dr. Muhammad Amirul Islam, and the characterization was done by Jae-young Cho. Then, the generated materials were blended with the membrane monomers in the solution before the phase inversion

process, which is the process of transferring the liquid membrane materials to a solid membrane. The membrane synthesis was done by Dr. Muhammad Amirul Islam. Anti-fouling properties were tested using surfactant stabilized oil-in-water emulsion. The anti-fouling experiments were done by me and Dr. Muhammad Amirul Islam.

## 2.2 Experimental Section

*Materials:* All reagents were purchased from Sigma-Aldrich (Oakville, ON, Canada), unless specified otherwise. (3-Aminopropyl) triethoxysilane (APTES, 98%), 2-bromoisobutyryl bromide (BIBB, 98%), triethylamine (TEA, 99%), hexamethyldisilazane (HMDS, 99%), methyl isobutyl ketone (MIBK, 99%), styrene (99%), N,N,N',N'',N''-pentamethyldiethylenetriamine (PMDETA, 99%), anisole (99%), poly(ethylene glycol) methacrylate (PEGMA, average Mn 360), copper(II) bromide (CuBr<sub>2</sub>, 99%), copper(I) bromide (CuBr, 98%), copper(I) chloride (CuCl, 99%), polyethersulfone (PES), 1-methyl-2-pyrrolidinone (NMP, 99%), and Millipore water (18.2 MΩ cm) from a Milli-Q Plus system (Fisher, Z00QSVC01, Toronto, ON, Canada) was used for all experiments.

### 2.2.1 Star-shaped Polymer Synthesis

Synthesis of silica-based ATRP initiator: The atom transfer radical polymerization (ATRP) initiator was prepared by reacting active bromine on the end of (3-aminopropyl) triethoxysilane, as shown in Figure 2-1. Briefly, 30 mmol (3-aminopropyl) triethoxysilane (APTES) and 36 mmol triethylamine (TEA) were dissolved in 50 mL anhydrous dichloromethane (DCM) in a 100 mL round bottom flask equipped with a Teflon-coated stir bar and immersed in an ice bath. Then, 36 mmol of 2-bromoisobutyryl bromide (BIBB) was added dropwise into the solution while stirring. After all the BIBB was added, the reaction was allowed to continue at room temperature for 3 h. The by-product, triethylammonium bromide (white solid), was filtered out, and the solvent DCM was removed by rotavaporation. The final product in this process was named as APTES-Br.

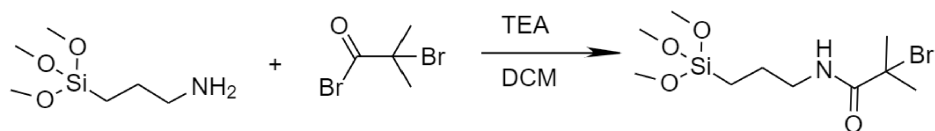


**Figure 2-1.** Schematic of the synthesis of atom transfer radical polymerization (ATRP) initiator.

Immobilization of Initiator onto Silica particles: After the ATRP initiator was synthesized successfully following the above process, the ATRP initiator had to be immobilized on the silica nanoparticles surfaces, as shown in Figure 2-2. Briefly, 13 g of 30 w/w% silica nanoparticles in methyl isobutyl ketone (MIBK) were added into a round bottom flask under an argon atmosphere. Then, 6.75 mmol APTES-Br were dissolved in 5 mL of MIBK and added into the reaction flask dropwise with vigorous stirring (around 500 rpm). The reaction was refluxed at 110 °C and 250 rpm for 24 h under argon protection. After the reaction time have reached, the reaction mixture was cooled down to room temperature and precipitated by adding hexane. The precipitated functionalized silica nanoparticles were collected after a 10 min 4400 rpm centrifugation, and the top layer was decanted.

After the initiator was immobilized successfully on the silica nanoparticle surface, there still are unreacted hydroxy groups on the silica nanoparticles surfaces, which can cause interferences in further reactions. The initiator immobilized silica nanoparticles were reacted further with 2.3 mL hexamethyldisilazane (HDMS) at 35 °C for 16 h to substitute the hydroxy group with trimethylsilyl groups. On completion of the reaction, the mixture was cooled down to room temperature and precipitated by adding hexane. The precipitated silica nanoparticles were collected after a 10 min 4400 rpm centrifugation, and the top layer was decanted. The final product was dried under a vacuum.

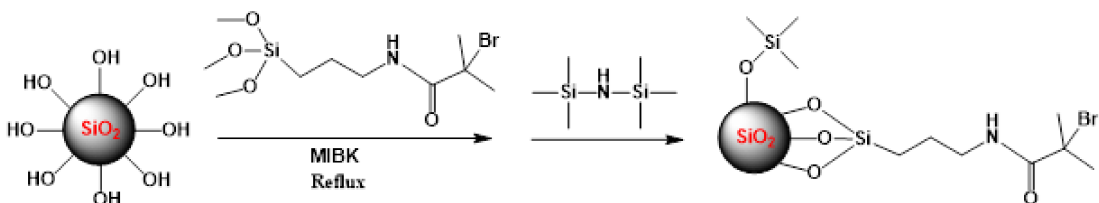


**Figure 2-2.** Schematic of the immobilizing ATRP initiator onto silica nanoparticles.

Grafting polymer arms on silica nanoparticles: Polystyrene (PS) and poly(ethylene glycol) methacrylate (PPEGMA) were grafted from ATRP-initiator immobilized silica nanoparticles for the synthesis of the final amphiphilic star-shaped polymers using conventional Cu(I)-catalyzed ATRP, as shown in Figure 2-3. Briefly, 500 mg of the product synthesized above and 0.29 mmol N,N,N',N'',N''-pentamethyldiethylenetriamine (PMDETA) were dissolved into 6.9 g styrene in a Schlenk flask. Then, three freeze-pump-thaw degassing cycles were used to remove all the oxygen in the reaction mixture. After the last freeze-pump-thaw cycle, 0.13 mmol of catalyst CuBr were added to the reaction under a rapid argon flow. The reaction mixture warmed up to room temperature after two more freeze-pump-thaw cycles. The Schlenk flask was transferred to a pre-heated oil bath at 90 °C, followed by stirring at 250 rpm for 30 h. After the reaction time had been reached, the materials were precipitated by adding methanol. The materials were purified by methanol and water washing and collected by gravity filtration, followed by vacuum drying for 24 h.

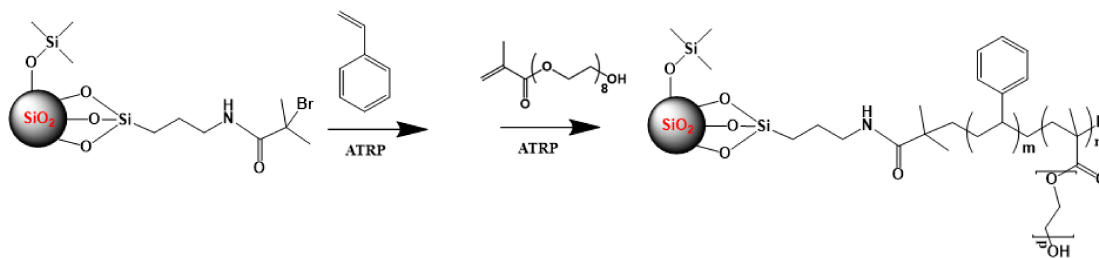


**Figure 2-3.** Schematic of grafting polystyrene and poly(ethylene glycol) methacrylate onto silica nanoparticles.

The materials have been grafted further with highly hydrophilic polymer PEGMA. 500 mg of the product synthesized above were dissolved in 25 mL of anisole and sonicated for 10 min in a Schlenk flask. Then, 0.29 mmol PMDETA and 3.62 g PEGMA were added to the reaction. Next, three freeze-pump-thaw cycles were performed, and 0.13 mmol ground powder of CuCl beads were added to the frozen mixture under a rapid argon flow. The reaction mixture warmed up to room temperature

after two more freeze-pump-thaw cycles. The Schlenk flask was transferred to a pre-heated oil bath at 45 °C, followed by stirring at 250 rpm for 3 h. After the reaction time had been reached, the reaction mixture was cooled down by liquid nitrogen and opened to air. Then, 200 mg of hydroquinone radical inhibitor were added, and the mixture was air blown for 1 h under stirring to inhibit the reactivity of the radicals on the end of polymer arms. Next, the polymer was precipitated by slowly adding to vigorously stirred hexane. The reddish-brown precipitate was dissolved in about 15 mL of THF and precipitated by slowly adding it into vigorously stirred ice-cold diethyl ether. This dissolution and precipitation from ether were repeated three times to a yield white precipitate. The precipitate was redissolved in 1,4-dioxane and freeze-dried for further use.

Characterization: The hydrodynamic diameters of silica nanoparticles, PS grafted silica nanoparticles, and PEGMA and PS grafted nanoparticles (0.04 w/w% aqueous solution) were measured by dynamic light scattering (DLS) using a Malvern Zetasizer Nano ZS - Malvern Instruments Ltd. at 25 °C. The average hydrodynamic diameter was calculated against silica nanoparticles latex standard by performing three series of 11 measurements. Moreover, images taken by a scanning electron microscope (SEM), using JSM-6010LA (JEOL, Peabody, MA), confirm the final particle size.

### **2.2.2 Membrane Preparation**

The membranes used in this study were prepared by the phase inversion process. There are four basic techniques used to create phase inversion membrane: precipitation from the vapor phase, precipitation by controlled evaporation, thermally induced phase separation, and immersion precipitation. The immersion precipitation phase inversion process is the most widely used membrane preparation method. A polymer solution (including organic solvent) is cast on the proper supporting layer and then submerged in a coagulation bath containing the nonsolvent. Due to the solvent and nonsolvent exchange, precipitation appears on the supporting layer. The combination of phase separation and mass transfer can affect the membrane structure. For example, if more hydrophilic polymers are added to the original polymer-solvent before submerging it into nonsolvent, the pore size on the surface and inside the final membrane is bigger

than the non-hydrophilic polymer added membrane.

In this study, star-shaped polymer-coated PES phase inversion membranes were made following the immersion precipitation process, as shown in Figure 2-4. Briefly, PES (4, 3.5, and 3 g for M1, M2, and M3, respectively) and star-shaped polymer (0, 0.5, and 1 g for M1, M2, and M3, respectively), as shown in Table 2-1, were dissolved in 21 g of organic solvent NMP under slow stirring for 24 h to eliminate air bubbles in the organic solvent and prepare a homogeneous PES-NMP solution. Afterward, the homogeneous solution was poured on thick flat glass and cast by a film scraper to a 150  $\mu\text{m}$  thickness. Then, it was immersed in an aqueous bath (2 h) for phase inversion and rinsed several times with Millipore water to remove the residue and solvent. In the end, the membranes were placed in Millipore water again for further use.

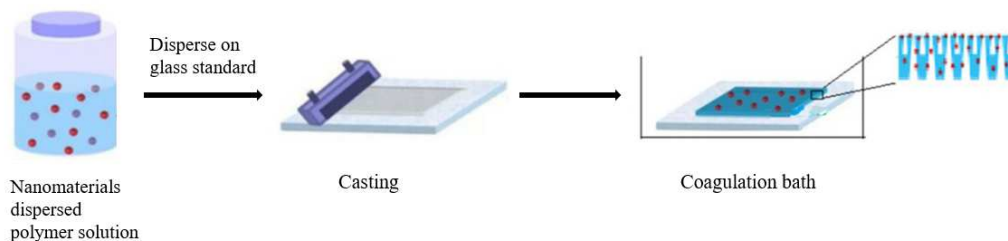


**Figure 2-4.** Schematic of flat sheet membrane preparation by blending and phase inversion technique. Adapted with permission from Ref.72 Copyright 2019, Elsevier Inc.

The hydrophilicity of the SP-blended PES membranes was evaluated by measuring their underwater n-hexadecane captive bubble contact angles. Contact angle measurements were performed using a contact angle analyzer (Data Physics Instruments GmbH) with 6  $\mu\text{L}$  of a captive n-hexadecane bubble in water. First, a 2 cm wide membrane strip was placed, face down, in a custom-made holder. Then, the membrane holder assembly was accommodated in a small, clear cuvette so that the membrane was immersed fully in water. A high-speed computer-controlled camera was focused on the membrane surface, and at least three n-hexadecane bubbles were placed on the membrane surface using a syringe with an inverted needle. Contact angle samples were kept under Millipore water and rinsed before analysis.

**Table 2-1.** Chemical Compositions of Phase Inversion Membrane used for Further Experiment

Membranes	PES (w/w%)	SP (w/w%)	NMP (w/w%)
M1	16	0	84
M2	14	2	84
M2	12	4	84

### 2.2.3 Filtration Experiments

To operate the filtration experiment, a 400 mL dead-end filtration cell (Amicon, UFSC40001), a nitrogen inlet, a stir plate, and a digital weighing balance (ME4002, Mettler Toledo) were used, as shown in Figure 2-5.

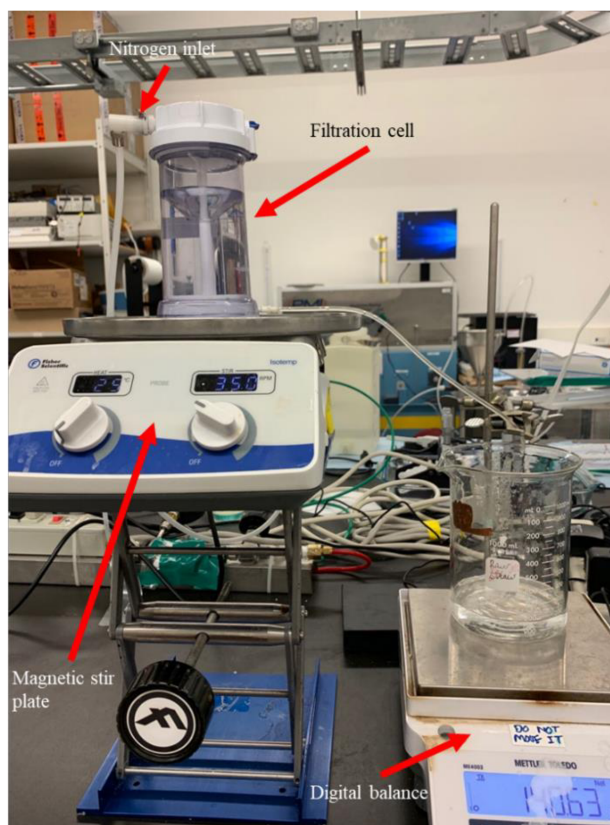


**Figure 2-5.** A side view of the filtration experiment basic setup.

Firstly, the pure water flux was measured using this setup. The membrane was

cut into the same size as the filtration cell and put at the bottom of the cell. Then, the filtration cell was filled with 450 ml DI water. Nitrogen gas was used to pressurize water through the membrane at 10 psi to obtain a stable water flux. The pure water flux of the membrane was calculated using the following equation:

$$J_w = m/\rho A_m \Delta t \quad (2-1)$$

where  $\underline{J}_w$  is pure water flux in L m<sup>-2</sup> of the membrane per hour (LMH),  $m$  is the mass of the permeate water (kg),  $\rho$  is water density (kg m<sup>-3</sup>),  $A_m$  is the effective area of the membrane (45.4 cm<sup>2</sup>), and  $\Delta t$  is the time of permeation (h).

The anti-fouling performance of bare and modified PES membranes was studied using surfactant stabilized hexadecane oil-in-water emulsion as the simulated oily wastewater. To prepare surfactant stabilized 1000 ppm hexadecane oil-in-water emulsion, 1 drop (~0.75 mg) of Tween 80 surfactant was dissolved in 300 mL of DI water. Then, 0.5 g of hexadecane were blended in this surfactant solution, and the mixture was homogenized with a homogenizer at the highest speed for 4 min. Another 200 mL of DI water were added to this emulsion and homogenized for a further 4 mins to generate 500 mL 1000 ppm hexadecane oil-in-water emulsion.

To evaluate the anti-fouling performance, the pure water flux for different membranes was tuned to the same value by changing the nitrogen gas pressure. After 30 mins of constant initial pure water flux (around 120 LMH), 400 mL of hexadecane oil emulsion were added to the cell, and the filtration was performed for 1 h at 350 rpm to record the permeate flux while the cell was refilled with the permeate on demand. At the end of oil filtration, after recording the permeate flux for the fouled membrane, the oil emulsion was discarded, and the membrane was rinsed with 400 mL of DI water for 20 min at 350 rpm. Then, recovered pure water flux was recorded for 30 mins to evaluate the flux recovery. The flux decline ratio (FDR) at the end of the oil filtration period and the flux recovery ratio (FRR) after a simple wash was calculated by Equation 2-2 and 2-3.

$$FDR (\%) = (1 - J_f/J_{wi}) \times 100 \quad (2-2)$$

$$FRR (\%) = (J_{wf}/J_{wi}) \times 100 \quad (2-3)$$

As the equation demonstrates, the FDR is the ratio of water flux decline from

initial pure water flux ( $J_{wi}$ ) to the permeate flux after steady-state fouling ( $J_f$ ) over the initial pure water flux ( $J_{wi}$ ), which helps to determine the extent of fouling upon filtration of targeted wastewater. Similarly, FRR is the ratio of recovered water flux ( $J_{wf}$ ) after washing over the initial pure water flux ( $J_{wi}$ ), which calculates the extent of flux recovery after an intermittent washing cycle with water.

### 2.3 Results and Discussion

The SEM images and DLS data indicated that the particles have been synthesized successfully following the synthesis procedures above. DLS measurements showed the hydrodynamic diameters of  $7 \pm 4$ ,  $30 \pm 10$ ,  $60 \pm 20$  nm for bare silica nanoparticles, PS grafted silica nanoparticle, and PS and PEGMA grafted silica nanoparticles, respectively. The bare silica nanoparticles show the smallest diameter as 7 nm. After grafting PS, particles grew from 30 nm to 60 nm after further grafting with PEGMA on PS arms. To verify the size of the particle, an SEM image was taken, as shown in Figure 2-6. Based on the SEM image, star-shaped nanoparticles show a diameter of  $32 \pm 2$  nm. The diameter result based on SEM is smaller than the result based on DLS because the polymer arms are extended underwater forming a solvent corona and increasing the overall size.

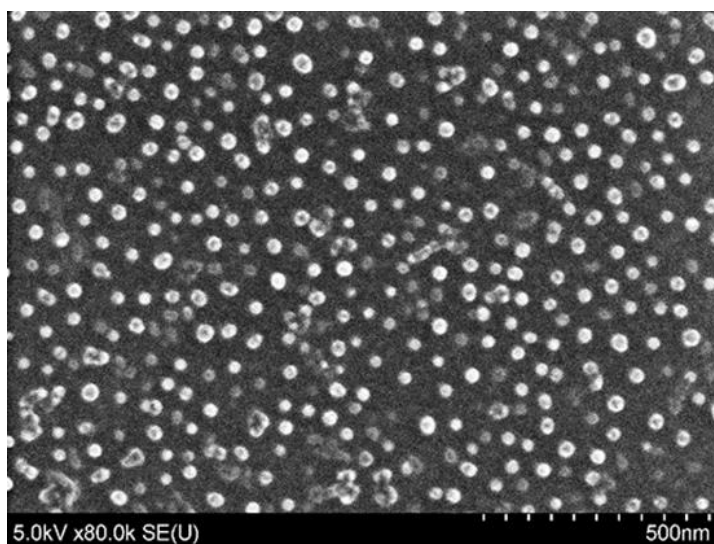


**Figure 2-6.** SEM image for final star-shaped polymers.

The antifouling coating material for the membrane should be hydrophilic,

which brings challenges with their coating on the hydrophobic membrane, such as PES. During the phase inversion process, star-shaped polymer nanoparticles were blended with the polymer solution and stirred overnight to remove the bubbles in the membrane solution. The air bubbles in the membrane solution can cause holes through the membrane after phase inversion process. The membrane solution was cast on a glass support and then submerged in a DI water bath. During the solvent and nonsolvent exchange, precipitation appears on the supporting layer while the amphiphile star-shaped particles were partially inside the solid membrane and partially in contact with the insolvent water. Because of the hydrophilic nature of the PEGMA arms, the hydrogen bond and dipole-dipole interaction between PEGMA arms and water molecules drives the star-shaped polymer molecule outside the solid membrane, while the hydrophobic-hydrophobic interaction between polystyrene and membrane drives the star-shaped polymer to stay in the solid membrane due to the hydrophobic nature of the polystyrene. Because the star-shaped polymer can be coated partially on the membrane surface during the phase inversion process, the PEGMA hydrophilic arms can bond with the water molecules in the solution forming a highly hydrophilic layer on the membrane surface, which can cause the anti-fouling behavior during oily wastewater filtration.

Although the star-shaped polymers have blended already during the phase inversion process, there are still chances for the hydrophilic material to fall off during the DI water washing. The membranes were soaked and rinsed by DI water to remove all the unbonded star-polymers. The oleophobicity of the star-shaped polymer-coated membrane surfaces were evaluated from the underwater n-hexadecane captive bubble contact angle measurements, as shown in Figure 2-7. The contact angles are  $61 \pm 3$ ,  $73 \pm 1$ , and  $83 \pm 2$  ° for M1, M2, and M3, respectively. The increasing contact angles indicate increasing hydrophilicity on the membrane surface, which supports the star-shaped polymers that were coated partially on the membrane surface to increase the hydrophilicity on the membrane surface. Moreover, this result also indicated that more star-shaped polymers added into the membrane solution can cause more hydrophilicity on the membrane surface. More star-shaped polymers addition can cause higher coating

density of star-shaped polymers and higher hydrophilicity on the membrane surface.

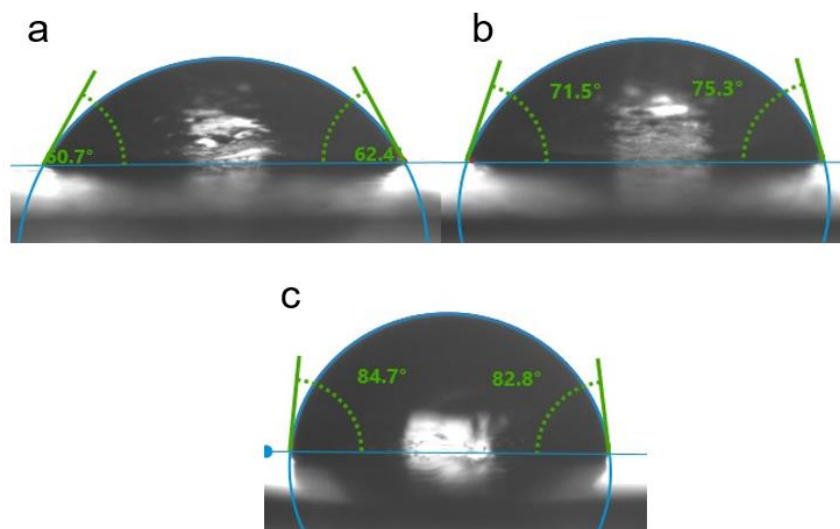


**Figure 2-7.** Evaluation of the blended SP membrane from representative underwater n-hexadecane captive bubble contact angles measurement. a) Bare PES membrane (M1), b) 2 w/w% star-shaped polymer-modified PES membrane, and c) 4 w/w% star-shaped polymer-modified PES membrane.

The anti-oil-fouling properties of the membranes were evaluated by filtering a highly concentrated hexadecane oil-in-water emulsion. The oil emulsion filtration was carried out under a constant water flux mode. The permeate flux was recorded for 1 h, as shown in Figure 2-8. At the end of the 1 h oil emulsion filtration period, the permeate flux was recorded after steady-state fouling on the membrane surface. The flux decline ratio (FDR) can be calculated by Equation 2-2. The flux decline for bare PES membrane is 114 LMH (92%), while the flux decreased only by 55 LMH (46%), and by 30 LMH (26%) for 2 w/w% and 4 w/w% star-shaped polymer blended PES membranes, respectively. A 2- and 4-times lower flux decline ratio (FDR) than the bare PES membrane is outstanding for the ultrafiltration of a highly concentrated oil emulsion since the fouling phenomenon reduces the water permeation and FDR represents the percentage of reduction in water flux due to fouling. This high anti-fouling property is endowed by an anti-fouling barrier created by the highly hydrated and hydrophilic PEGMA arms.

Another important factor in determining the membrane's antifouling properties is the flux recovery ratio (FRR), which is the percentage of flux that can be recovered

after the intermittent washing cycle. The FRR indicates if the fouling is reversible or irreversible. After a 1 h oil emulsion filtration, the membranes were washed with DI water for 20 min at 350 rpm and rinsed three times to remove the reversible fouling. The final water flux was recorded for another 30 min, as shown in Figure 2-8. Almost no flux recovery was observed for the bare PES membrane, which gives a low FRR value of 13 %. FRR values are and 62.7% and 91.3% for 2 and 4 w/w% star-shaped polymer blended PES membranes, respectively. The high FRR values indicate that most of the fouling is reversible. However, the water flux kept increasing after washing. The main reason might be the surfactant-induced washing and subsequent detachment of star-shaped polymer particles from the membrane. Since the particles have fallen from membranes, water permeability increase due to the membrane becomes “hollower”, which causes the increasing flux after washing.

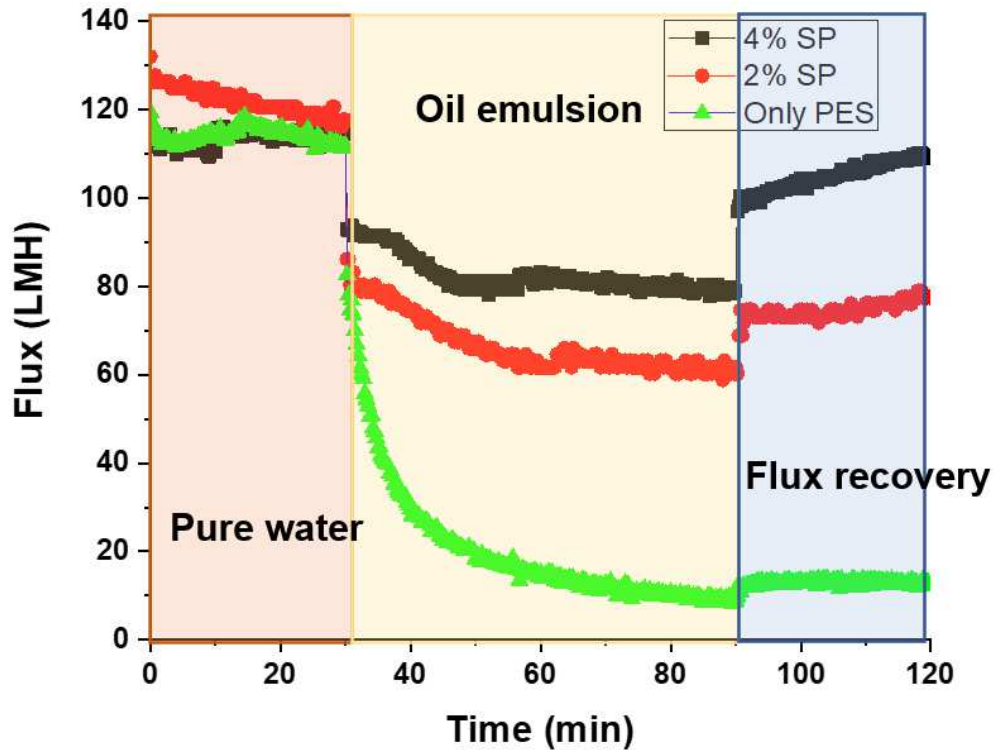


**Figure 2-8.** Evaluation of antifouling properties against hexadecane oil-in-water emulsion with initial pure water flux (red region), oil emulsion filtration (yellow region), and pure water flux recovery (blue region)

## 2.4 Conclusion

In summary, star-shaped polymers with silica core, hydrophobic polystyrene, and hydrophilic poly (ethylene glycol) methacrylate arms were synthesized to develop and optimize a stable and versatile anti-fouling PES membrane. The star-shaped polymers in the membrane provided substantial enhancement in the surface hydrophilicity and antifouling properties against a model organic foulant (i.e., hexadecane oil). Star-shaped polymer composited PES membranes exhibited higher surface wettability and lower flux decline properties against oil emulsion than bare PES membranes. A higher composition of star-shaped polymer can result in a higher hydrophilicity on the membrane surface. The 4 w/w% star-shaped polymers composited PES membrane provided the best anti-fouling performance. However, some of the star-shaped polymers fall off during the washing process, which can cause the membrane to lose its anti-fouling property and increase the cleaning and replacing cost. In the next chapter, pNIPAm microgel coated PES membranes have been designed to have better anti-fouling performance and self-cleaning properties.

## CHAPTER 3

### **Improved Anti-fouling and Self-cleaning Ability of Polyethersulfone Membranes Coated with PNIPAm-based Microgels for Oily Water Treatment**

This chapter describes how different sizes and copolymer compositions pNIPAm-based microgels have been synthesized and characterized. Coating performance has been optimized by tuning the microgel sizes and coating procedure. Anti-fouling membranes have been made through a stepwise pressurized coating process and optimized by using microgels with different copolymer compositions. Their anti-fouling properties were characterized by constant flux filtration of oil-in-water emulsion. The filtration flux was recorded during the filtration, and the flux decay illustrated the degree of fouling on the membrane surface and inside the membrane. The coating stability also was characterized by the images before and after long-term filtration. At last, self-cleaning properties were characterized by comparing the pure water flux before and after alternative warm–cold water washing. The pure water flux was recorded before and after DI water washing, and the flux recovery illustrated the degree of reversible foulant that has been removed from the membrane surfaces during the self-cleaning process.

#### **3.1 Introduction**

The cross-linked nature of stimuli-responsive polymer networks resembles a porous membrane structure and allows for selective mass transport through the polymer network. Due to their hydrophilicity, selectivity, and stimuli-responsivity, stimuli-responsive polymers have been studied intensively in membrane science. Stimuli-responsive polymers have been tested for various applications, such as responsive membranes<sup>73,74</sup> and anti-fouling coatings.<sup>48-50</sup> So far, stimuli-responsive polymers have been applied in membrane science as functional elements in different morphologies, such as polymer brushes, hydrogels, and microgels. Hydrogels are three-dimensional cross-linked networks of stimuli-responsive polymers. The physical and chemical properties of the hydrogels, like mesh sizes, stimuli conditions, and hydrophilicity, can

be tuned by changing the polymerization conditions to adapt to different separation desires. For example, mesh sizes can be tuned by changing the crosslinker ratio during the polymerization. Hydrogels with different mesh sizes composited membranes can provide adjustable permeability during filtration.<sup>75,76</sup> Pure hydrogel membranes have shown switchable permeability and are used for controlled drug release applications.<sup>77</sup> The mechanical stability for hydrogel membranes is still the main challenge for wastewater treatment application because of the soft nature of the hydrogel materials. Therefore, hydrogels composed of conventional membranes have shown great potential in the field of oily wastewater treatment. However, most of the hydrogel composite membranes have shown slow response and relatively low anti-oil-fouling properties. In contrast to the bulk hydrogel composed membranes, microgel composed membranes show outstanding anti-fouling and self-cleaning behaviors.

Microgels are spherical hydrogels with colloidal dimensions, which is a great advantage over bulk hydrogels. The micrometer-sized colloidal structure provides better flexibility since microgels can be used as building blocks for membrane coating and faster response, based on the higher surface-to-volume ratio. In membrane science, microgels play a role in tuning mass transport as an active layer, improving anti-fouling behavior, and controlling permeability.<sup>78,79</sup> Stimuli-responsive microgels that exhibit a reversible volume phase transition by the external environment trigger have been a focus of considerable scientific investigation due to their potential application in drug delivery,<sup>80</sup> sensing, biosensing,<sup>81</sup> and anti-fouling coating.<sup>82</sup> The stimuli-responsive behavior is of special relevance for the membrane since each microgel can act as a micro-scale membrane by selectively mass transporting inside the microgel network. The most intensively studied stimuli-responsive polymer for membrane modification is poly-(N-isopropylacrylamide) (pNIPAm), which is known to undergo a reversible phase change at a low critical solution temperature (LCST) of 32 °C, where the polymer switches from the fully water-soluble free coil (below 32 °C) to a non-water-soluble collapsed globular state (above 32 °C). Microgels based on pNIPAm are highly soluble and swollen when the solution  $T < 32$  °C, while they collapse, expelling their water of solution at  $T > 32$  °C. A schematic representation of the microgels thermoresponsive

behavior is displayed in Figure 3-1. The co-polymerization with different monomers enables the adjustment of the volume phase transition temperature (VPTT) and further addition of stimuli-responsive elements. Increasing the overall hydrophilicity of copolymers is known to lower the LCST, while increasing the overall hydrophobicity tends to raise the LCST to a higher temperature. A common co-monomer is acrylic acid (AAc) with a  $pK_a$  of 4.25, leading to an increase of the VPTT due to the higher hydrophilicity and a pH-responsive swelling above a pH of 4.25. Since charged co-monomers can increase the hydrophilicity of microgels, charged microgels can provide better anti-fouling properties as a membrane coating material in oily wastewater treatment. Moreover, the charges of the gel itself allows them to adjust the separation performance of the membrane for charged solutes.

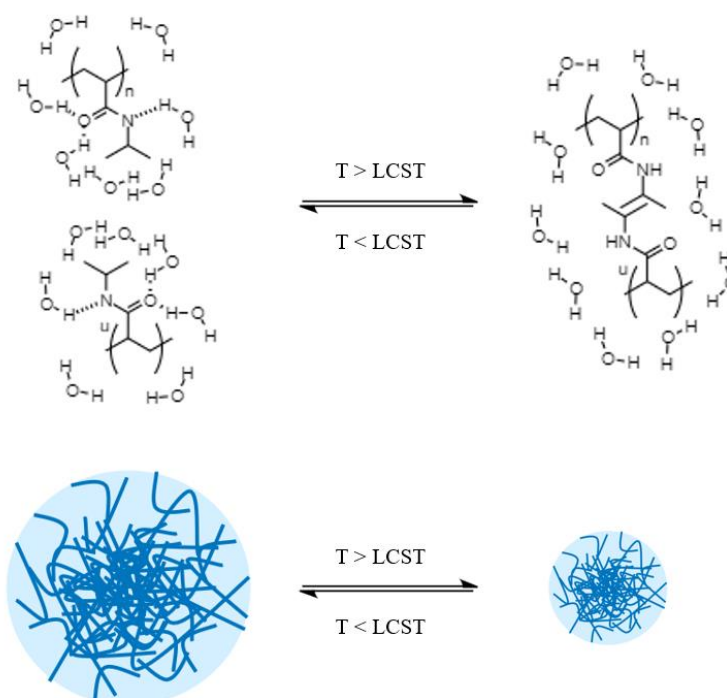


**Figure 3-1.** Swelling/shrinking mechanism of pNIPAM chains in microgels and illustration of the conformational change induced by temperature changes on pNIPAM based microgel particles.

A variety of researchers have explored rendering membrane surfaces resistant to foulant adsorption. Stimuli-responsive polymers have been used previously on membrane surfaces for fouling removal by blending microgels in the membrane solution during preparation,<sup>51</sup> grafting microgels on the membrane surface after preparation,<sup>83</sup> or

crosslinking microgels after depositing them on the membrane surface to have a higher coating stability.<sup>84</sup> Temperature was used as the most common stimulus. Poly(N-isopropylacrylamide)-co-acrylic acid (PNIPAm-co-AAc) microgel was the most commonly used stimuli-responsive polymer as an anti-fouling material, based on its ability to prevent or remove foulants due to its highly hydrophilic nature and size change with temperature or pH stimulus. Membrane surfaces with pNIPAm-co-AAc microgels have been shown to clean proteins,<sup>85</sup> natural organic matters,<sup>86</sup> and oil droplets<sup>87</sup> effectively upon cleaning with an alternating temperature below and above the LCST of the polymer.

Due to the repulsive forces between pNIPAm-co-AAc microgels, simple adsorption of a stable microgel layer on the membrane surface is not possible.<sup>88</sup> However, most chemical protocols for membrane functionalization with pNIPAm-co-AAc microgels need advanced coating procedures. For example, Bell et al. has developed a thin layer composited PES membrane with a crosslinked pNIPAm based microgel. Microgels were crosslinked with each other after depositing on the porous membrane support.<sup>84</sup> Although chemical crosslinking provides a highly stable coating ability on the membrane surfaces, the extra crosslinking process needs to be controlled carefully on the membrane surfaces. Since microgel networks are highly hydrophilic and able to hold water inside, chemical residuals processed during chemical coating may become one of the major concerns for these methods. Instead of chemical bonding, physical coating processes can offer controlled anti-fouling properties on membranes without affecting the permeation properties if the material is designed properly.<sup>15</sup> In this chapter, a stable pNIPAm-co-AAc microgel coating has been developed by a stepwise pressurized coating process. Three different sizes of pNIPAm-co-AAc microgels were used to investigate the microgels' behavior during the pressurized coating process. Furthermore, the anti-fouling, permeability, and self-cleaning performances were explored. Four different AAc composed pNIPAm-based microgels were investigated, with pNIPAm-co30%AAc microgels coated membrane showing the best anti-fouling property. Finally, the microgel coated membranes were used for a long-term operation to explore their coating stability for industry applications.

## 3.2 Experimental Section

*Materials:* N-isopropylacrylamide (NIPAm) monomer was purchased from TCI (Portland, Oregon) and purified by recrystallization from hexanes (ACS reagent grade, EMD, Gibbstown, NJ) before use. N,N'-Methylenebisacrylamide (BIS, 99%), acrylic acid (AAc, 99%), ammonium persulfate (APS,  $\geq 98\%$ ), sodium dodecyl sulfate (SDS, 99%), and sodium hydroxide (NaOH) were obtained from Sigma-Aldrich (Oakville, Ontario) and were used as received. Hydrochloric acid (HCl) was purchased from Caledon Lab (Georgetown, Ontario). Whatman #1 paper filters were obtained from GE Healthcare (U.K.). Oil emulsion was prepared by n-hexadecane (99%, Fisher Scientific, Canada) and tween 80 surfactant (Bio-Rad, Hercules, CA). Deionized (DI) water with a resistivity of 18.2 M $\Omega$  cm was obtained from a Milli-Q Plus system and was used for all experiments. Polyethersulfone (PES) membrane of average 100 nm surface pore size with polypropylene backing was provided by Solecta membranes (Oceanside, CA) and was used to study the effect of microgels coating on the anti-fouling properties.

### 3.2.1 PNIPAm-based Microgel Synthesis

Microgels were synthesized by free radical precipitation polymerization, following a previously published procedure. Three different sizes and four different compositions of acrylic acid (AAc) microgels were synthesized. Briefly, for pNIPAm microgels with different sizes, NIPAm (13.3 mmol) and BIS (0.7 mmol) were weighed and dissolved with 99 mL DI water in a 250 mL beaker. The mixture was stirred for 0.5 h on a stir plate and filtered through an 0.2  $\mu$ m filter into a 3-neck round-bottom flask. The flask was equipped with a reflux condenser, a temperature probe, and a needle for introducing N<sub>2</sub> gas into the reaction mixture. The reaction mixture was bubbled with N<sub>2</sub> gas and heated to 70 °C for 1 h. SDS (0, 3.5, 7, 14 mmol for MG-1, NG-1, NG-2, and NG-3, respectively) was dissolved in 1 mL of DI water and added to the reaction mixture in one aliquot. The polymerization was initiated immediately by the addition of APS (0.2 mmol) in 1 mL of DI water. The solution turned turbid after  $\sim$ 1 min, indicating the successful initiation. The polymerization was allowed to proceed at 70 °C for 4 h under an N<sub>2</sub> environment. The resulting suspension was allowed to cool

overnight with continuous stirring, followed by filtration through glass wool to remove any large aggregates. The MG-1 microgel solution was distributed into centrifuge tubes and purified via centrifugation at ~10000 rpm for ~30 min to form a pellet, followed by removing the supernatant and resuspending the pellets in DI water. This purification process was repeated six times. The NG-1, NG-2, and NG-3 microgel solutions were placed into a dialysis bag (20kD, Spectra, CA) and dialyzed against DI water for 14 d, with periodic DI water replacement every 24 h. For pNIPAm microgels with different copolymer compositions, NIPAm (13.3, 11.9, 10.5, and 9.1 mmol, for 0AAc, 10AAc, 20AAc, 30AAc MG, respectively) and BIS (0.7 mmol) were weighed and dissolved with 99 mL DI water in a 250 mL beaker. The mixture was stirred for 0.5 h on a stir plate and filtered through a 0.2  $\mu\text{m}$  filter into a 3-neck round-bottom flask. The flask was equipped with a reflux condenser, a temperature probe, and a needle for introducing  $\text{N}_2$  gas into the reaction mixture. The reaction mixture was bubbled with  $\text{N}_2$  gas and heated to 70  $^\circ\text{C}$  for 1 h. AAc (0, 1.4, 2.8, and 4.2 mmol for 0AAc, 10AAc, 20AAc, and 30AAc MG, respectively) and SDS (3.5 mmol) were added to the heated reaction mixture in one aliquot, and the polymerization was initiated immediately by the addition of APS (0.2 mmol) in 1 mL of DI water. The polymerization was allowed to proceed at 70  $^\circ\text{C}$  for 4 h under an  $\text{N}_2$  environment. The resulting suspension was allowed to cool overnight with continuously stirring, followed by filtration and purification by centrifugation. All the microgels synthesized and purified above were freeze-dried for further use.

### **3.2.2 Stepwise-pressurized Coating**

The 100 nm pore size PES membrane was pretreated to remove the protective coating layer by soaking it into isopropyl alcohol for 30 min with gently stirring, followed by rinsing with DI water at least three times. To coat the membranes by the pressure-assisted method, a pretreated PES membrane was placed at the bottom of the 400 mL dead-end filtration cell and 800 mL of DI water were passed through the membrane under 2 psi to remove the excess isopropyl alcohol, which might remain inside the membrane. At the same time, the microgel solution was prepared by resuspending 25 mg freeze-dried microgels with 200 mL DI water in a 500 mL beaker. The microgel

solution and another 200 mL DI water were placed on a hot plate and heated to 55 °C. After 800 mL of room-temperature DI water had passed through the pretreated membrane, the whole dead-end filtration cell was rinsed three times with 55 °C DI water, and the rest of the 55 °C DI water was passed through the membrane for 20 min to have a stable coating temperature. Then, the 55 °C microgel solution was filtered through the membrane at 2 psi at 350 rpm. After the permeate flux became constant for 2 min, the pressure was increased to 5 psi. The pressure was increased stepwise to 10, 15, 20, 30, 40, 50 psi after the permeate flux became constant for 2 min. The permeate flux was recorded after the microgel solution was filtered under 50 psi for 5 min to have a stable permeate flux. Next, the microgel solution was poured out, and the membrane was kept under a nitrogen pressure for 30 min for drying. Another 400 mL of room-temperature DI water were added gently into the filtration to allow microgel swelling for 2 h. Then, the membrane and the cell were rinsed gently with three portions of 100 mL of room-temperature DI water to remove the uncoated microgel on the membrane surface. The membrane was kept under 400 mL of room-temperature DI water and stirring at 150 rpm for 2d with periodic DI water replacement every 24 h. The membrane was rinsed gently with DI water before further characterizations and filtration tests.

### **3.2.3 Oily Wastewater Filtration**

The basic oily wastewater filtration procedure was introduced in Chapter 2, Section 2.2.3. Briefly, membranes and filtration cells were rinsed with 100 mL of room-temperature DI water three times. Then, the filtration cell was filled with 450 mL of DI water. Nitrogen gas was used to pressurize water through the membrane at 10 psi to obtain a stable pure water flux. Then, the nitrogen pressure was tuned slightly until a constant initial pure water flux (around 150 LMH) has been reached for a comparison of the quantitative anti-fouling performance of an unmodified membrane and a microgel coated membrane. While waiting for the pure water flux recording, a surfactant-stabilized hexadecane oil-in-water emulsion was prepared as a simulated oily wastewater sample. To prepare a surfactant stabilized 1000 ppm hexadecane oil-in-water emulsion, 1 drop (~ 0.75 mg) of tween 80 surfactant was dissolved in 300 mL

of DI water. Then, 0.5 g of hexadecane were blended in this surfactant solution, and the mixture was homogenized with a homogenizer at the highest speed for 4 min. Another 200 mL of DI water were added to this emulsion and homogenized for a further 4 min to generate 500 mL of 1000 ppm hexadecane oil-in-water emulsion. After recording the pure water flux for 30 min, 400 mL of a hexadecane oil emulsion were added to the cell, and the filtration was performed for 1 h at 350 rpm to record the permeate flux, while the cell was refilled with the permeate on demand. At the end of oil filtration, after recording the permeate flux for the fouled membrane, the oil emulsion was discarded, and the membrane was rinsed with 400 mL of DI water for 20 min at 350 rpm. Then, the recovered pure water flux was recorded for 10 min to evaluate the flux recovery. The flux decline ratio (FDR) at the end of the oil filtration period and the flux recovery ratio (FRR) after a DI water wash were used to evaluate the anti-fouling properties.

### **3.2.4 Long-term Filtration Stability Tests**

The coating stability was investigated by a long-term filtration experiment. After the oil filtration experiment operated above, another 400 mL of hexadecane oil emulsion were added to the cell. The filtration was kept in operation under atmospheric pressure and 150 rpm stirring for a week with a periodic oil emulsion replacement every 24 h. After a week, the membrane was soaked in 400 mL of 150 ppm tween 80 surfactant solution at 350 rpm for 2 h to examine the removal of microgels from the surface. After decanting the surfactant solution and three times gentle rinsing with DI water, fresh 400 mL of 150 ppm tween 80 surfactant solution were added to the cell and passed through the membrane to remove the microgels from the membrane pore. The membranes were rinsed gently with DI water before further characterizations.

### **3.2.5 Self-cleaning by an Alternative Wash with Different Temperatures**

To investigate the self-cleaning behavior, filtrations have been operated at both below and above the LCST temperature of the polymer, followed by cleaning also with alternating temperatures. For the filtration operated below LCST, 30 min of pure water flux were recorded. The pressure also was tuned to obtain a 150 LMH pure water flux.

After 30 min recording, 400 mL of freshly prepared hexadecane oil emulsion were added to the cell, and the filtration was performed for 1 h at 350 rpm to record the permeate flux while the cell was refilled with the permeate on demand. At the end of the oil filtration, the membrane was rinsed first with 100 mL of 55 °C DI water three times, followed by washing with 400 mL of 55 °C of DI water for 20 min at 350 rpm. Then, the membrane was rinsed with 100 mL of room-temperature DI water three times, followed by washing with 400 mL of room-temperature DI water for 20 min at 350 rpm. This washing process was repeated three times. After the three-washing cycle finished, another 400 mL of 55 °C DI water were added into the filtration cell, and the hot-water flux was recorded. In the end, another 400 mL of room temperature of DI water were added into the filtration cell, and the cold-water flux was recorded. The FDR at the end of the oil filtration period and the FRR after an alternative cleaning with different temperature DI water washing were used to evaluate the self-cleaning behavior. After the washing process, two more filtrations were operated at both 55 °C and 25 °C. The FRR was used to determine the coating stability after the self-cleaning process.

### **3.2.6 Characterization of Microgels and Membranes**

The hydrodynamic diameters of microgels were measured by dynamic light scattering (DLS) using a Malvern Zetasizer Nano ZS - Malvern Instruments (Westborough, MA, USA) equipped with a 633 nm light source. The average hydrodynamic diameter result was reported as the average value of three measurements, where each measurement had 13–15 scans with an acquisition time of 4–5 sec. The light scattering intensity was detected at 173 °.

The oleophobicity of the microgel-coated PES membranes was evaluated by measuring their underwater n-hexadecane captive bubble contact angle. Contact angle measurements were performed using a contact angle analyzer (Data Physics Instruments GmbH) with a 6 µL captive n-hexadecane bubble in water. A 2 cm wide membrane strip was placed first, face down, in a custom-made holder. Then, the membrane holder assembly was accommodated in a small, clear cuvette so that the membrane was immersed fully in water. A high-speed computer-controlled camera was

focused on the membrane surface, and at least three n-hexadecane bubbles were placed on the membrane surface using a syringe with an inverted needle. Contact angle samples were kept under DI water and rinsed before analysis.

The topography of unmodified and microgel-coated membranes by the pressure-assisted method and non-pressure-assisted method was evaluated using SEM. Samples were sputter-coated with Au/Pd for 100 s at 50  $\mu$ A prior to the analysis of the surface morphologies using SEM. The SEM was operated at 5 kV accelerating voltage and 10  $\mu$ A emission current on an ultra-high resolution Hitachi S-4800 cold field emission SEM.

### **3.3 Results and Discussion**

To control the final sizes of microgels, inorganic salts and ionic surfactants are a couple of agents that are used. Typically, a higher concentration of salt can increase the particle sizes, while a higher concentration of surfactant would decrease the particle sizes. Based on the surface electrical double layer theory,<sup>90</sup> increasing the ionic strength can cause the decrease of the double layer thickness around the microgel particles, which induces the aggregation to larger particles. Surfactants can stabilize the small particles and prevent aggregation, resulting in smaller microgels. PNIPAm microgels were synthesized by free radical precipitation polymerization with four different amounts of surfactant, measured and characterized by DLS. The hydrodynamic diameters of the microgels in DI water were measured using DLS at 25 °C and 55 °C. The DLS results can be found in Table 3-1. The microgel sizes decreased by increasing the surfactant concentration. During the microgel synthesis, interfaces were created between the microgel particle surfaces and solvent water. The surfactant molecule was adsorbed on the microgel surface because of its amphiphilic nature. The microgel cannot keep growing after the surfactant occupies the whole microgel surface. The hydrophobic tail of the surfactant has adsorbed on the membrane surface since the microgel is also hydrophobic above LCST while the negatively charged ionic head of the surfactant covered the microgel surface. The highly negatively charged surface inhibits the active radical on the end of polymer chains, resulting in stopping the microgel growth. A higher surfactant concentration can inhibit the microgel growth when it is small since

the smaller microgels have a higher surface area that needs more surfactant molecules to inhibit the surface radical. MG-1 exhibits a hydrodynamic radius of  $870 \pm 30$  nm (25 °C) and  $290 \pm 20$  nm (55 °C). Likewise, NG-1 showed a diameter of  $520 \pm 20$  nm (25 °C) and  $230 \pm 20$  nm (55 °C); NG-2 showed a diameter of  $250 \pm 20$  nm (25 °C) and  $80 \pm 10$  nm (55 °C); and NG-3 showed a diameter of  $60 \pm 10$  nm (25 °C) and  $23 \pm 4$  nm (55 °C).

To optimize the coating ability of microgels on the 100 nm pore size PES membrane surface, four different microgels with different sizes, MG-1, NG-1, NG-2, and NG-3, were studied to observe the microgel behaviors during the stepwise coating process. The permeate flux was recorded during the coating process to predict the microgel behavior during the coating process, as shown in Figure 3-2.

**Table 3-1.** Hydrodynamic Diameter and Standard Deviations for the Investigated Microgels

Microgels	Hydrodynamic Diameter (nm)	
	at 25 °C	at 55 °C
MG-1	$870 \pm 30$	$290 \pm 20$
NG-1	$520 \pm 20$	$230 \pm 20$
NG-2	$250 \pm 20$	$80 \pm 10$
NG-3	$60 \pm 10$	$23 \pm 4$

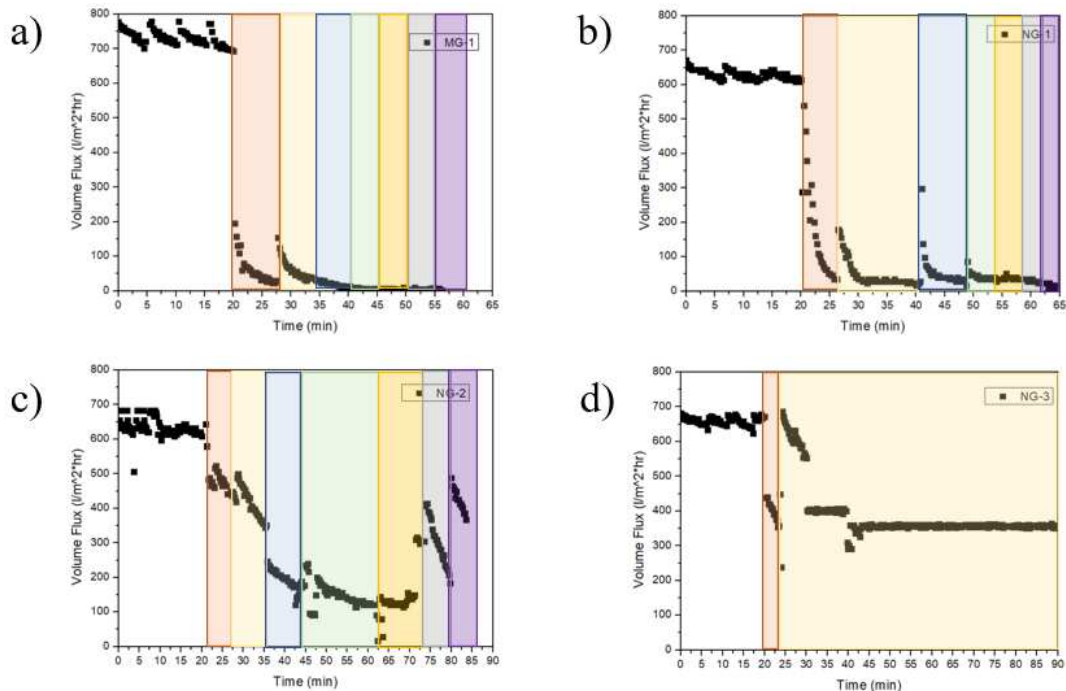


**Figure 3-2.** The permeate flux during stepwise pressurized coating for (a) MG-1, (b) NG-1, (c) NG-2, and (d) NG-3 at 2 psi (red region), 5 psi (yellow region), 10 psi (blue region), 20 psi (green region), 30 psi (orange region), 40 psi (grey region), and 50 psi (purple region).

The detailed stepwise pressurized coating process has been discussed in Section 3.2.2. Briefly, a 55 °C microgel solution was filtered through the membrane with a stepwise increasing pressure from 2, 5, 10, 15, 20, 30, 40, to final 50 psi. Firstly, 20 min of 55 °C pure water flux at 2 psi were recorded to warm up the filtration cell. The periodic fluctuation of pure water flux during the first 20 min was caused by the refill with 55 °C DI water. For the filtration operated in this section, the driving force included two parts: nitrogen gas pressure and water pressure in the filtration cell. During the filtration, the water pressure decreased with the feed solution past the membrane, which can cause decreased pressure and flux. After refilling the filtration cell with 55 °C DI water, the flux suddenly increased with the water pressure on the membrane. After 20 min of 55 °C pure water flux have been recorded, a 55 °C microgel solution was filtered firstly at 2 psi. For MG-1, as shown in Figure 3-2(a), the permeate flux dramatically decreased after the microgel solution was added since some of the microgels blocked the pores on the membrane surface. After the flux was stabilized for 17 min at 2 psi, the pressure was increased to 5 psi, which caused the dramatic flux increase. After the pressure had

been reached at 5 psi, the filtration system was stabilized for 10 min. However, after a 10-psi pressure was applied to the filtration system, the flux did not increase with the pressure change. Finally, after 20 min of microgel filtration, there was no permeate coming through the membrane.

The pores on the membrane surface of the biggest microgel, MG-1, are fully blocked, with the result that the pressure change cannot influence the flux and no permeate comes through the membrane in the end. Although the MG-1 coating has high stability, it is not suitable for further experiments because of its low permeability. For the second biggest microgel, NG-1, as shown in Figure 3-2(b), the flux still increased after a change to a higher pressure after increasing the pressure to 10 psi, and stabilized at the same level (around 40 LMH) until 40 psi. This reveals that the NG-1 microgel coating has a high stability and retains the permeability for further filtration experiments. For the second smallest microgel, NG-2, as shown in Figure 3-2(c), the flux needed a longer time to stabilize. In the beginning, the flux decreased slowly because the microgels were passing slowly through the membrane. During the first 2, 5, 10, 20, and 30 psi, some of them remained on or inside the membrane, while some of them passed through, resulting in a slow decrease in the permeate flux. However, after the pressure increased to 40 and 50 psi, all the microgels that remained on or inside the membrane passed through the membrane, resulting in a sudden increase in flux. The flux increase over 40 psi indicates that the coating is not stable enough for further experiments. For the smallest microgel, NG-3, as shown in Figure 3-2(d), the flux decreased at 2 psi and suddenly increased by changing it to 5 psi. Then, the flux stabilized at 350 LMH at 5 and 10 psi. The observation indicates that NG-3 microgels were coated on the membrane at 2 psi. However, microgels fall out by slightly by increasing the pressure to 5 psi. Since the NG-3 microgels cannot change the membrane structure, the permeate flux is stabilized at a higher flux level. MG-1 has the best stability but no permeability, while NG-2 and NG-3 coatings have high permeability but low stability. Among the four microgels with different sizes, NG-1 is the best option to optimize both the coating stability and the membrane permeability for further experiments.

NG-1 was investigated further by three different coating processes to confirm that the

stepwise coating process can provide a uniform and stable coating on a 100 nm PEM membrane. Firstly, SEM images for an uncoated PES membrane were taken as a control group. The pretreated PES membrane was soaked at room temperature for 48 h, with periodic DI water replacement every 24 h, and rinsed for further characterization, as shown in Figure 3-2 (a). Then, constant pressurized coating, followed by drying, and step-wise pressurized coating, followed by drying have been investigated to optimize a uniform and stable coating on the membrane surface. The general coating processes were the same. Briefly, 25 mg of freeze-dried microgels were resuspended in 200 mL of DI water and heated to 55 °C. Then, the 55 °C microgel suspension was filtered through the membrane under pressure. For the constant pressure coating process, a constant 10 psi pressure was applied during the whole coating process. On completion of the coating, one membrane was rinsed immediately with DI water to wash out the unstable microgel, as shown in Figure 3-2 (b). Another membrane went through an additional drying process under 10 psi pressure for 30 min, followed with a DI water rinse, as shown in Figure 3-2 (c). Both membranes were stored in the filtration cell with room-temperature DI water and continuous stirring at 150 rpm for 48 h, with periodic DI water replacement every 24 h, and rinsed for further characterization. The SEM images in Figure 3-2 (b) and (c) revealed that the NG-1 microgels have coated successfully on the membrane by the constant pressure process in comparison with the non-microgel coated PES membrane. However, the NG-1 microgel coating did not show high uniformity and stability. During the constant pressure coating process, microgels were coated on the membrane under pressure. Because of the hydrophilic and hydrophobic nature of microgels below and above the LCST, the coating process above LCST (at 55 °C) can increase the hydrophobic–hydrophobic interaction between the microgels and membrane. After the temperature decreased below LCST (at 25 °C), the microgels showed a hydrophilic nature and weaker interactions with the membrane. With 25 °C DI water washing, the weakly coated microgels were rehydrated and resuspended in water, resulting in a low coating stability. The additional drying process slightly enhanced the hydrophobic–hydrophobic interaction between the microgels and membrane because microgels undergo an extra dehydration process. The hydrogen

bonds in water between the carbonyl and the secondary amine groups with water molecules were broken during the drying process, resulting in the further collapse of the microgel and some aggregates on the membrane. The aggregate surface can hydrate easily with DI water, while the surface that interacted with the membrane cannot, therefore, it cannot be washed off easily from the membrane surface. However, some of the microgels cannot form aggregates during the drying process and were washed off, causing the ununiform coating on the membrane surface.

For the stepwise pressurized coating, a step-wise increasing pressure was applied from 2, 5, 10, 15, 20, 30, 40, to the final 50 psi during the coating process, following by a drying process under 10 psi pressure for 30 min. Then, the membrane was rinsed also with room-temperature DI water and stored in the filtration cell with room-temperature DI water and continuous stirring at 150 rpm for 48 h, with periodic DI water replacement every 24 h, and rinsed for further characterization. The SEM images in Figure 3-2 (d) revealed that the stepwise pressurized coating process can generate a uniform and stable coating layer. The step-wise pressure enabled the microgels to form a more compressed coating layer on the membrane surface. The first layer of microgels was coated on the membrane at low pressure. After the flux became constant, which means that the dynamic microgel adsorption is at equilibrium, the increasing pressure can compress the first layer of microgels, causing the permeability to decrease. Another layer of microgels was deposited on top of the first layer since the first layer already had been compressed. These compressing and coating processes were repeated seven times to obtain a uniform and high stable coating, as shown in Figure 3-3 (d). The coating generated by the step-wise coating process was uniform for the whole membrane area because the microgel layers already had been packed well before the drying process. The drying process did not lead to aggregates since the microgels on the bottom layers already had been compressed. The coating exhibited a high stability during the rehydration process since the step-wise pressure compressed the microgels into a three-dimensional network. The microgel layer that interacted with the membrane surface was less hydrated because of its lower contact area with water, which adhered to the microgel coating network on the membrane surface. The top

microgel layers were hydrated fully for further anti-fouling and self-cleaning performance.

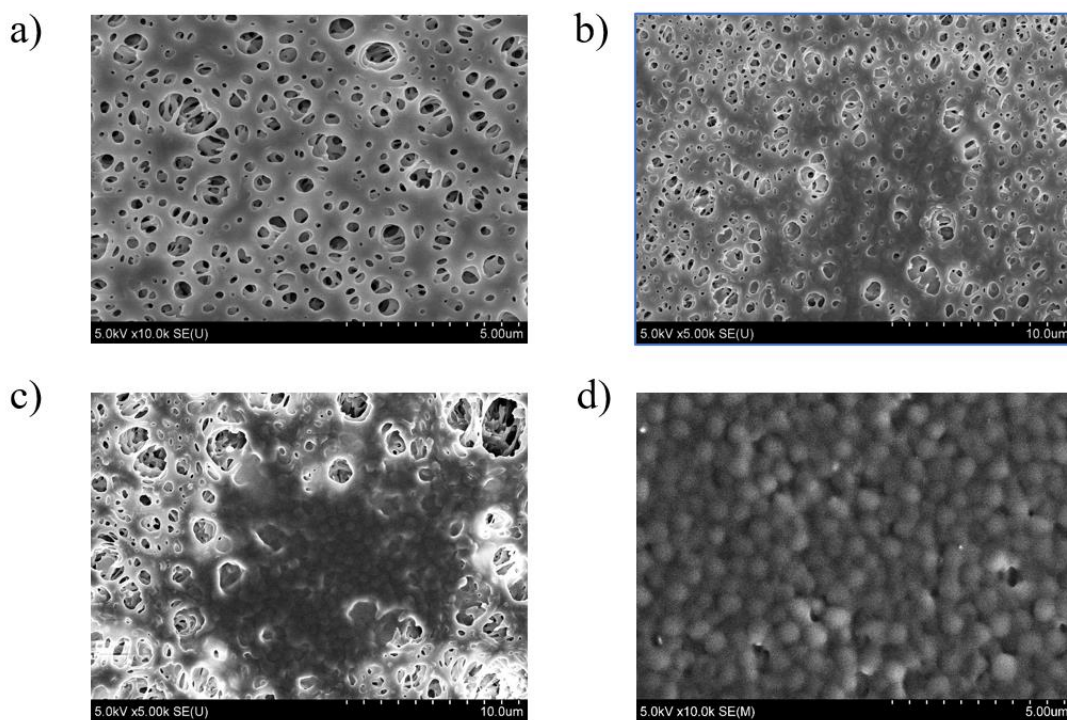


**Figure 3-3.** The SEM images for (a) an unmodified PES membrane and an NG-1 coated PES membrane via (b) constant pressure coating, (c) constant pressure coating, followed by drying, and (d) stepwise pressure coating followed by drying

To optimize the anti-oil-fouling property, ionic functional groups can be modified in microgels to enhance hydrophilicity and anti-fouling properties. The addition of functionality to microgels can be accomplished by two approaches: direct (copolymerization) and indirect (post-polymerization modification). In the direct approach, functional monomers are copolymerized directly with the primary monomer, NIPAm, during the free radical polymerization process. The indirect approach is preferred in cases where a small molecule, which can be absorbed by a microgel particle, is present with the desired functionality or the conditions for the direct polymerization approach are unfavorable to the functional comonomer. To increase the hydrophilicity of microgels, acrylic acid (AAc) was used to copolymerize directly with NIPAm. Four sets of microgels were prepared with NIPAm as the main monomer, with 0%, 10%, 20%, and 30% AAc comonomers during polymerization (named as 0AAc,

10AAc, 20AAc, and 30AAc, respectively) to optimize the anti-fouling performance for oil filtration.

As the coating ability has been optimized by microgels with different sizes, all the microgels for further filtration were designed to be the same size as NG-1. During the polymerization, 3.5 mmol of surfactant also were used to tune the microgel size for the best coating performance for a 100 nm PES membrane. DLS measurements indicate hydrodynamic diameters of  $520 \pm 20$ ,  $550 \pm 10$ ,  $590 \pm 20$ , and  $620 \pm 30$  nm for 0, AAc, 10AAc, and 20AAc, respectively, at pH 5.5. The increasing sizes with AAc compositions were caused by the electron repulsion force among the deprotonated acrylic groups in the microgel. FTIR spectra also were used to characterize the pNIPAM-co-AAc microgels, and the results are shown in Figure 3-4. The expected vibrational frequencies from FTIR analysis are shown in Table 3-2.

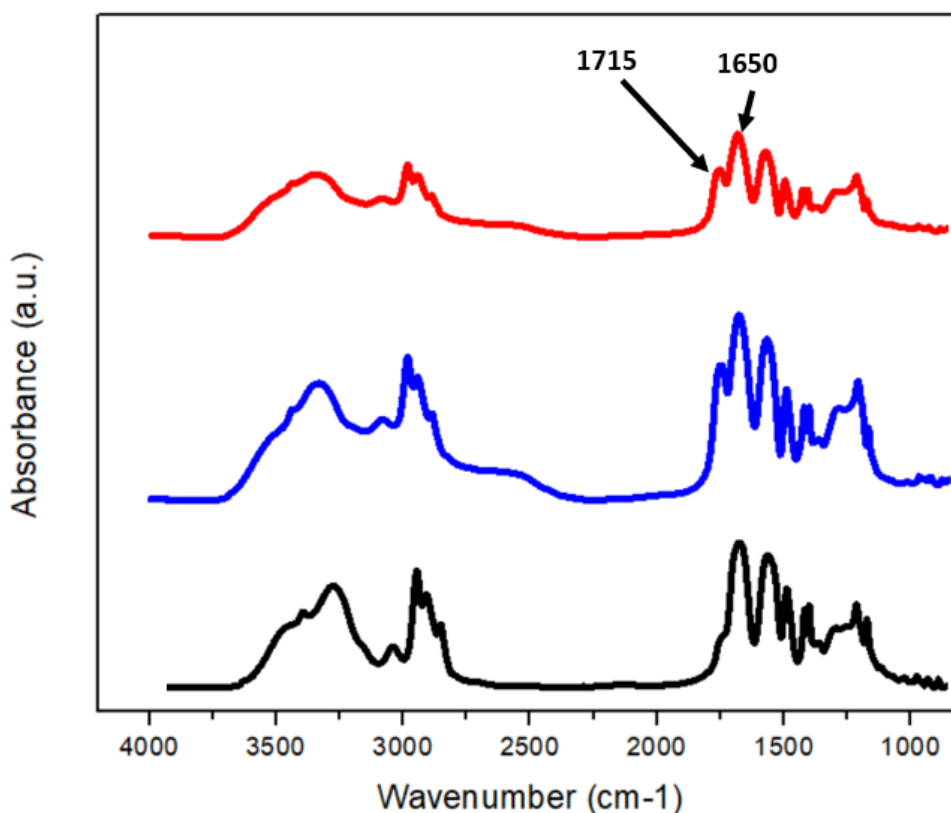


**Figure 3-4.** FTIR spectra of 10AAc (black), 20AAc (red), and 30AAc (blue).

**Table 3-2.** Distinctive IR Functional Groups and Their Representative Vibrational Frequencies for PNIPAm-co-AAc Microgels

Functional groups	Wavenumbers (cm <sup>-1</sup> )
N-H stretching	3440
O-H stretching	3320
=C-H stretching	3070
-C-H stretching	2972
carboxylic acid C=O stretching	1715
amide C=O stretching	1650
N-H bending	1536
C-H bending	1459
C-O stretching	1172

Based on Beer's law, the absorbance is the product of molar absorptivity, molar concentration of chemical species, and path length. However, in FTIR measurements with a KBr pellet, the molar concentration and path length are hard to control. The absolute absorbance is not reliable to estimate the actual AAc composition in pNIPAm-co-AAc microgels. Since we need only the information of the AAc ratio in the microgels, the ratio of the absorbance at 1717 cm<sup>-1</sup> (carboxylic acid C=O, representing for NIPAm) to that at 1645 cm<sup>-1</sup> (amide C=O, representing for AAc) can represent the AAc composition in the microgel. Based on the results shown in Table 3-3, the actual AAc composition in the microgel synthesized above is not as we expected. The result shows that the actual composition is 12.2% for the microgel to which 10% AAc was added during the synthesis. This result is not reliable because the 1717 cm<sup>-1</sup> peak, which represents the carboxylic acid C=O, is too weak and overlapped in the FTIR spectrum. The other two microgels show a lower actual composition than the AAc added during

the synthesis because not all the AAc has been polymerized in the microgels. Some of the AAc monomers did not polymerize in the microgels and washed away during the purification process.

**Table 3-3.** The NIPAm to AAc Monomer Ratios in Different AAc Composed Microgels

<i>Microgel</i>	<i>Absorbance at 1717 cm<sup>-1</sup></i>	<i>Absorbance at 1645 cm<sup>-1</sup></i>	<i>Ratio</i>	<i>Actual Composition</i>
<i>10AAc</i>	0.0378	0.2739	0.14	12.2%
<i>20AAc</i>	0.132	0.566	0.23	19.0%
<i>30AAc</i>	0.1057	0.315	0.34	25.4%

All four sets of microgels were used in further oily wastewater filtration. As discussed above, similar-sized microgels were used as coating on the 100 nm pore size membrane surface. To characterize the oleophobicity of the microgel coated membrane surface, underwater n-hexadecane captive bubble contact angles were measured, as shown in Figure 3-5. The contact angles are  $61 \pm 3$ ,  $126 \pm 1$ ,  $137 \pm 1$ , and  $145 \pm 5$  ° for unmodified PES membranes and 0, AAc, 10AAc, and 20AAC for microgel coated membranes. The contact angles of the 20AAc coated membranes have a higher standard deviation because the n-hexadecane droplet could not be adsorbed on the surface by simple contact. A mechanical force had to be added to force the droplet to stick on the membranes, causing the irregular bubble shape and higher uncertainty. The absence of the contact angle measurement is because the n-hexadecane droplet cannot be absorbed by the membrane surface, even with additional mechanical pressure. The largest increase ( $65$  °) in contact angle was observed for 0AAc coated PES membranes, followed by 10AAc (ca.  $11$  °) and 20AAc (ca.  $8$  °)-coated membranes. Pure pNIPAm microgel coated PES membranes exhibit a much higher surface hydrophilicity on the coated membrane surface. As higher AAc composed microgels were coated, higher surface hydrophilicity was observed. The increasing contact angles indicate increasing hydrophilicity on the membrane surface, which may have higher anti-fouling behavior

during further experiments.

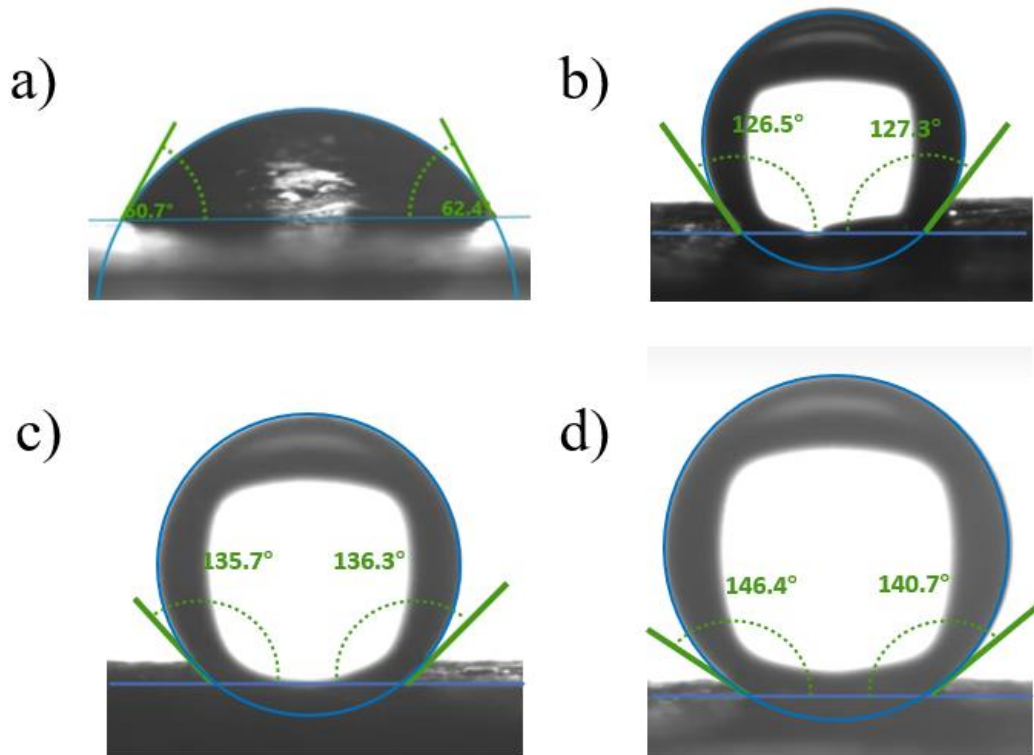


**Figure 3-5.** Evaluation of the microgel coated membrane from representative underwater n-hexadecane captive bubble contact angles measurements. a) Bare PES membrane, b) 0AAc microgel coated PES membrane, c) 10AAc microgel coated PES membrane, and d) 20AAc microgel coated PES membrane.

The anti-oil-fouling properties of the membranes were evaluated by filtering a highly concentrated (ca. 1000 ppm) hexadecane oil-in-water emulsion. The oil emulsion filtration was carried out under constant initial pure water flux mode, with the permeate flux recording for 1 h, as shown in Figure 3-6. The initial pure water fluxes were tuned by slightly changing the pressure to the 150 LMH level and keeping it constant for the following experiments. At the end of an oil emulsion filtration period of 1 h, the flux decline for unmodified PES membrane was 113 LMH (75%), while the flux decreased only by 52 LMH (35%), 45 LMH (29%), 43 LMH (27%), and 23 LMH (15%) for 0AAc, 10AAc, 20AAc, and 30AAc-coated PES membranes, respectively.

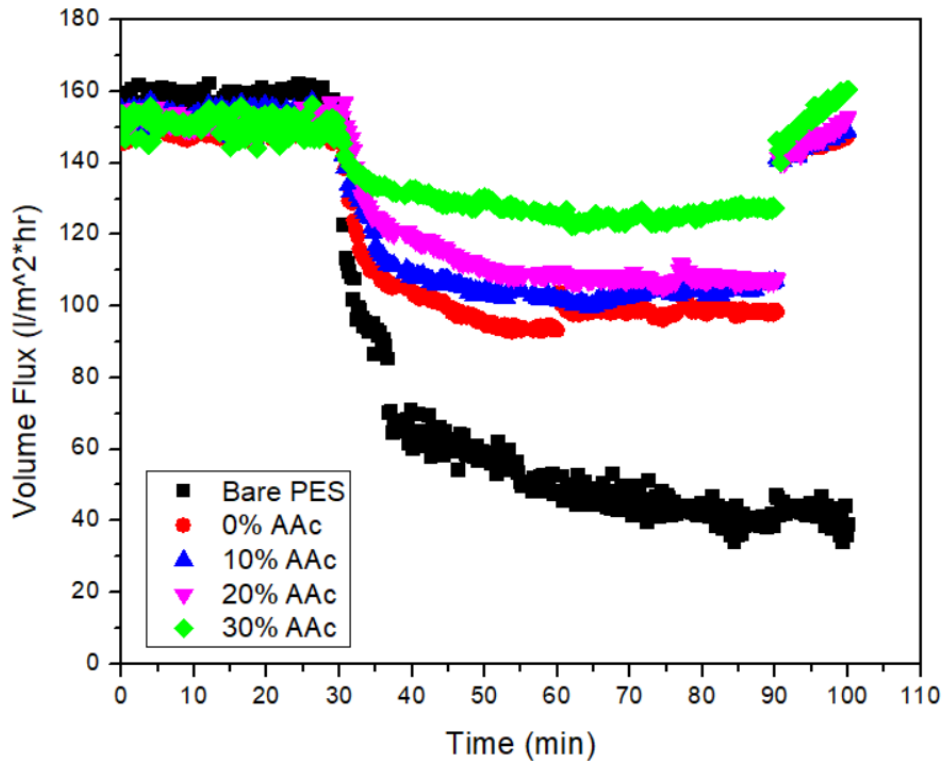


**Figure 3-6.** Evaluation of antifouling properties against hexadecane oil-in-water emulsion using unmodified PES membrane (black), and 0AAc-(red),10AAc-(blue), 20AAc-(pink), and 30AAc-(green) coated PES membranes.

The PES membrane is one of the most susceptible membranes to organic fouling, and oil is known as one of the most severe organic foulants. A 2–5 times lower flux decline ratio than the unmodified PES membrane is outstanding for the ultrafiltration of a highly concentrated oil emulsion. Such a high antifouling property of microgel-coated membranes is endowed by an antifouling barrier created by the highly hydrated microgel layer and negatively charged surface potential. Another important factor in determining the membrane’s antifouling properties is the flux recovery ratio, which is the percentage of flux that can be recovered after the intermittent washing cycle. No flux recovery was observed for the unmodified PES membranes, whereas the flux recovery ratio was 89, 92, 95, and 105% for 0AAc, 10AAc, 20AAc, and 30AAc-coated PES membranes, respectively. All the microgel coatings exhibits a high recovery ratio, which indicates that most of the oil fouling on the membrane surface is reversible. However, the flux recovery ratio for 30 AAc-coated membranes is higher than 100%.

First, the surfactant, which is used to stabilize the oil emulsion, can align with microgels on the membrane to increase the hydrophilicity of the coated membrane surface further, causing a higher recovery flux. Another reason might be the detachment of some microgel coating from the membrane surface, which also causes the flux to increase after washing. Comparing the slope for the 10 min recovery flux, the 0AAc coated membrane has the flattest flux, and the 30AAc coated membrane exhibits a significant increase in the flux. Because of the high charge density of 30AAc microgels, the charge repulsion force between the microgels on the coating layer can cause the fully hydrated microgel on the top layer to detach from the compressed three-dimensional coating network. The detachment of microgels increased the permeability of the coated membrane, resulting in a significant increase in the water flux after washing.

Both the 20AAc and 30AAc coated membranes were chosen to investigate the coating stability for long-term operation. Based on the observation of the flux recovery above, 20AAc coated membranes have similar increasing flux as other microgels coated membranes, and 30AAc coated membranes exhibit a significant flux increase. Briefly, after the oil filtration experiment operated above, both membranes were kept operating for a week under atmosphere pressure, with periodic oil emulsion replacement every 24 h. Membranes were washed by a surfactant solution to remove the unbonded microgel and soaked in DI water for another 48 h before further characterizations, as shown in Figure 3-7.

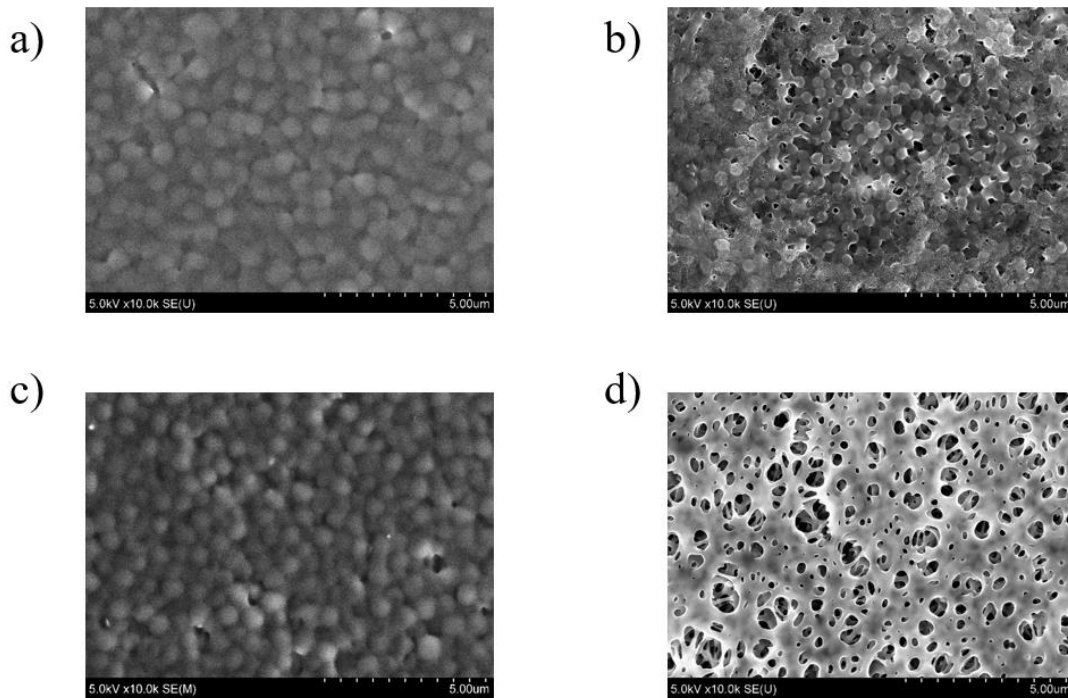


**Figure 3-7.** The SEM images for a 20AAc coated PES membrane (a) before and (b) after one-week filtration under atmosphere pressure and 30AAc coated PES membrane, and (c) before and (d) after one-week filtration under atmosphere pressure.

Comparing (a) and (b) in Figure 3-7, 20AAc microgels still were coated tightly on the PES membrane surface. The microgel coated surface was seen before the oily wastewater filtration. After a long-term operation, the microgels cannot be seen clearly because the membrane surface had been fouled by n-hexadecane. Some areas showed a clear microgel coating layer on the surface, like the center of the SEM shown in Figure 3-7 (b). Some areas only roughly showed the general microgel sphere shape without a clear boundary between microgels, like the left area in Figure 3-7 (c). The oily foulant on the membrane surface can cause the fuzzy boundary since the foulant is covered on the coating surface. By comparing (c) and (d) in Figure 3-7, the 30AAc coating did not show a high stability during the long-term operation. The 30AAc was coated tightly on the membrane at the beginning, as shown in Figure 3-7 (c), even after washing in DI water for 48 h. However, after one week of low-pressure filtration, followed by surfactant washing, almost all the microgels detached from the membrane surface, which confirms the observation of the significant flux increase during the flux

recovery process. Based on the detachment fact for the 30AAc microgel coating, only 20AAc coated PES membranes were used for the further self-cleaning experiment.

The self-cleaning behavior was studied by observing the flux change before and after alternative DI water washing with 55 °C and 25 °C temperatures. To compare the self-cleaning behavior with an unmodified PES membrane and a 20AAc coated PES membrane, both membranes underwent a warm-cold water washing process. Briefly, the unmodified PES membrane was washed by alternate 55 °C and 25 °C water right after the 55 °C or 25 °C oil filtration. No flux recovery was observed after washing for the unmodified PES membrane, as shown in Figure 3-7 (a). For the 20AAc coated PES membrane, a pure water flux at 25 °C was recorded for 30 min right after the long-term filtration with the same pressure applied for the anti-fouling experiment, and the pressure was kept constant for the following experiment. Then, 55 °C and 25 °C DI water was used to wash the membrane, following the procedure discussed in the experimental section. The periodic fluctuation of flux was caused by the refill with 55 °C DI water. For the filtration operated in this section, the driving force included two parts: nitrogen gas pressure and water pressure in the filtration cell. During the filtration, the water pressure decreased with the feed solution past the membrane, which can cause decreased pressure and flux. After the refill, the suddenly increased water pressure caused a higher flux, which resulting in a spike on the graph. Then, a pure water flux at 25 °C also was recorded to investigate the self-cleaning. Another cycle of oil-in-water filtration was operated at the end to confirm the 20AAc coating stability after long-term operation. As shown in Figure 3-8(c), the membrane was fouled by the oil during the long-term operation because the pure water flux significantly declines to around 35%. However, after washing at 55 °C and 25 °C DI water, the pure water flux showed a high recovery ratio of around 90%, which indicates that most of the foulant on the coating surface has been removed during the washing process. The alternating washing with the temperature below and above LCST can cause the volume change on the microgel coated surface. The mechanical force caused by the volume change on the membrane drives the foulant detachment from the coating surface, resulting in a high flux recovery ratio. However, the flux increase can also be caused by the detachment

of microgel coating, as discussed for 30AAc coated microgel. Another oil emulsion filtration cycle at 55 °C and 25 °C was operated to test the coating stability after a long-term operation and washing process, as shown in the yellow, blue, and green region in Figure 3-7 (b). The fluctuation of flux at 55 °C can be explained by the reason above with the water pressure change during the refilling. After both filtration processes, followed by washing, the water flux has increased slightly by 2 LMH. This small flux increase can be caused by the further detachment of foulant on the coating surface during the washing process. The flux did not keep increasing over time, which indicates the coating has outstanding stability even after long-term operation.

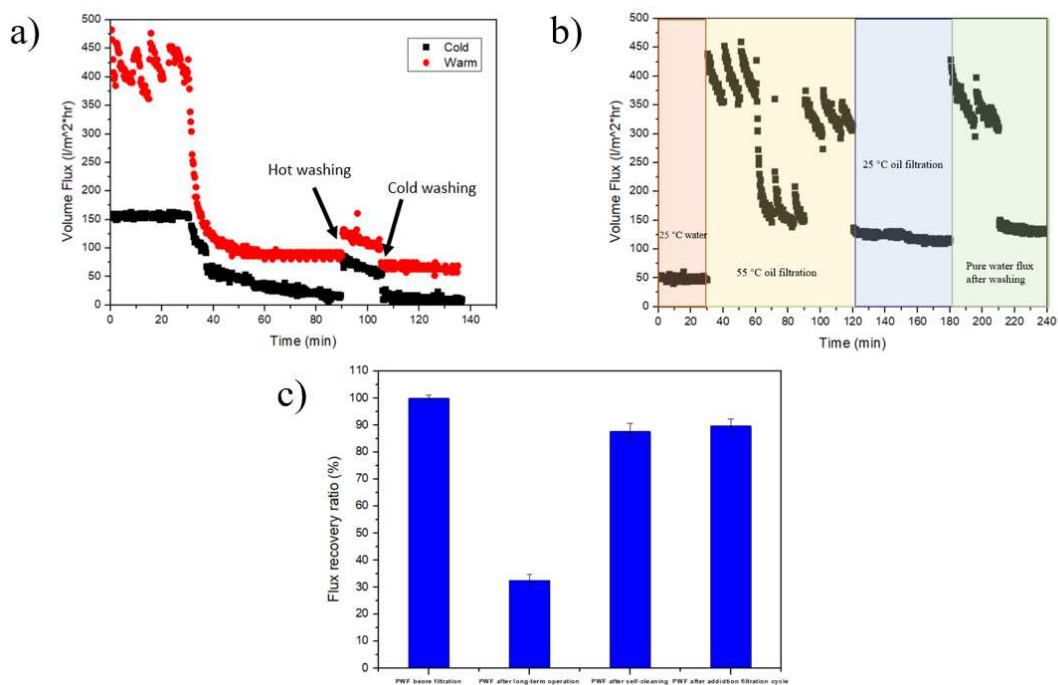


**Figure 3-8.** Evaluation of self-cleaning behavior with alternative 55 °C and 25 °C DI water washing for (a) an unmodified PES and (b) a 20AAc coated PES membrane. Firstly, a 25 °C flux was recorded (red region). Then, an oil filtration was operated at 55 °C (yellow region) following by another oil filtration at 25 °C (blue region). At last, the pure water flux at both 55 °C and 25 °C was recorded (green region). (c) The percentage flux recovery before and after alternative 55 °C and 25 °C DI water washing, followed by further 55 °C and 25 °C oil filtration cycles.

### 3.4 Conclusion

In summary, microgels with variable size were synthesized, followed by various coating processes to develop and optimize a stable coating on a hydrophobic PES

membrane with a 100 nm pore on the surface. The NG-1 sized microgel provides the best coating stability among the other three sizes. In comparison, bigger microgels, like MG-1, block the pores on the membrane, leading to the permeability decrease, while the smaller microgels, like NG-2 and NG-3, passed through the membrane, leading to a weak coating density and stability. The stepwise coating process provided the best coating stability among constant pressure coating, with or without the drying process. Moreover, microgels with variable AAc compositions were synthesized to develop and optimize a stable and highly antifouling stable coating, with a self-cleaning behavior on a hydrophobic PES membrane with a 100 nm pore on the surface. The pNIPAm-co-AAc microgels coating provided substantial enhancement in the surface hydrophilicity and antifouling properties against a model organic foulant (i.e., hexadecane oil). PNIPAm-base microgel coated membranes exhibited similar surface wettability. The flux decline and recovery properties against oil emulsion are due to the AAc composition in a microgel. Microgels with a higher AAc composition exhibit better anti-fouling properties. The 30AAc and 20AAc coating stability were tested by long-term filtration, followed by washing with a surfactant. It was found that the 30AAc coating was loosely bound on the membrane surface and easily washed off. The 20AAc coating provides the best stability and self-cleaning behavior via alternate water wash above and below LCST. This study provides valuable insight into the fabrication of fouling resistant membranes by tailoring the size and composition of microgels.

## CHAPTER 4

### **Poly (N-Isopropylacrylamide) based Microgels as Sorbents for Pb<sup>2+</sup>, Hg<sup>2+</sup> and Cr<sup>3+</sup> Removal for Filtration Application**

Previously, the Serpe group has used poly (N-isopropylacrylamide)-based microgels and their assemblies as an absorbent for the remediation of organic dyes.<sup>91-95</sup> In this chapter, the microgel behaviors have been studied in metal ion solutions. The influence of microgel compositions on microgel behaviors was investigated with increasing metal ion concentrations, both in the solution or on a surface. Moreover, these microgels were studied as sorbents for the removal of recalcitrant contaminants in the wastewater, using Pb<sup>2+</sup>, Hg<sup>2+</sup>, and Cr<sup>2+</sup> as models. The heavy metal ion removal was studied in solution and on a permeable membrane surface during a filtration process.

#### **4.1 Introduction**

Though natural causes exist, increased industrialization and anthropogenic activities have been the major contributors to environmental issues. The rising population and urbanization cause a scarcity of quality water. The water crisis is a health crisis. Nearly one million people die each year from unclean water.<sup>96</sup> Access to safe water and sanitation contributes to improved health and helps prevent the spread of infectious diseases. As we face the COVID-19 pandemic, more than ever, access to safe water is critical to the health of families around the world.<sup>96</sup> The presence of heavy metals in wastewater also has been increasing with the increased industrialization and anthropogenic activities, e.g., plating and electroplating industry, batteries, pesticides, mining industry, rayon industry, metal rinse processes, tanning industry, fluidized bed bioreactors, textile industry, metal smelting, petrochemicals, paper manufacturing, and electrolysis applications.<sup>97</sup> Because of the non-biodegradable and carcinogenic nature, heavy metals are classified as toxic and capable of accumulating in the organism's body through the food chain and cause diseases and disorders in human metabolism systems. Some of the emerging contaminants of great concerns are lead (Pb<sup>2+</sup>), mercury (Hg<sup>2+</sup>),

and chromium ( $\text{Cr}^{3+}$ ). Industrial wastes from lead smelting, lead mining, dyeing, printing, and rubber production have contributed to the increased sources of lead in wastewater, and these sometimes find their way into the environment. Exposure to higher lead levels in drinking water can cause poisoning in humans and damages the kidneys, liver, heart, brain, skeleton, and nervous system.<sup>55</sup> Mercury enters wastewater from a variety of sources, including dental practice wastes, fertilizers, landfill leachate, paints, domestic waste inputs, groundwater infiltration, and stormwater drainage contributions.<sup>98</sup> A high mercury concentration in the human body can result in impairment of kidney function, chest pain, and dyspnea. The environmental important form of chromium is  $\text{Cr}^{3+}$  because the  $\text{Cr}^{2+}$  will be oxidized rapidly by  $\text{O}_2$  in the air. Chromium is used widely in metallurgy, electroplating, and in the manufacturing of paints, pigments, preservatives, pulp, and papers, and it can cause damage to the brain, lungs, kidneys, and developing fetuses, and high blood pressure or heart rate, vomiting and diarrhea, skin rashes, and eye irritation.<sup>56</sup>

Heavy metal contaminations of the aquatic system are a serious environmental issue. Therefore, the development of an efficient, fast, and environmentally friendly technology to remove heavy metals from wastewater systems is necessary. There is evidence in the numerous works that have been done using various water remediation technologies for wastewater, including membrane filtration,<sup>99,100</sup> precipitation,<sup>101</sup> coagulation,<sup>102</sup> and absorption.<sup>103-104</sup> However, most of the technologies required additional chemical treatment with high capital and operational cost and may leave by-products with potential hazards for drinking water. Membrane filtration combined with absorption has been optimized as the method of choice in water remediation because of its high efficiency, low cost, and ease of operation. Various absorbents have been used for the removal of heavy metals by absorption, such as carbon foam,<sup>105</sup> activated carbon,<sup>106</sup> zeolite,<sup>107</sup> clay minerals,<sup>108,109</sup> and biochar.<sup>110</sup> One of the greatest drawbacks to these materials is reusability. The cost of regenerating these materials for reuse is comparable to producing fresh absorbents, resulting in new materials being used every time and increasing the cost.

Microgels can be investigated as sorbents because of their facile means of

synthesis and reusability. Due to the porous network, high surface-to-volume ratio, and reversible volume phase transition nature of a microgel, pNIPAm-based microgels have been shown to remove heavy metal ions.<sup>111,112</sup> The microgel three-dimensional network structure entraps contaminants at temperatures below the lower critical solution temperature (LCST) of 32 °C. Contaminants are pushed out above the LCST because of the collapse of the polymer chains in the microgel. Above the LCST, a hydrophobic–hydrophobic interaction is dominant between the polymer chains. The repulsed water molecules carrying contaminants are pushed out of the microgel. This system can act as a capture and release system for contaminants. Because of the positive charge nature of our target, heavy metal ions, negatively charged monomer acrylic acid (AAc) can be copolymerized with NIPAm monomers to increase the absorbability for heavy metal ions. The additional electrostatic repulsive forces from the charged comonomer need to be considered besides the thermal-responsive behavior, as discussed in Chapter 3. A schematic representation of the microgels' behaviors in containing the AAc response to pH variations is displayed in Figure 4-1(a). When the solution  $\text{pH} > \text{p}K_{\text{a}}$ , most of the carboxylic acid groups in AAc are deprotonated. The negative charges on the deprotonated carboxylic acid groups cause microgel swelling because of the charge–charge repulsions in the microgel structure and increase in the osmotic pressure. However, when the solution  $\text{pH} < \text{p}K_{\text{a}}$ , most of the carboxylic acid groups are protonated, and the microgels shrink. Based on the pH-responsive behavior, the absorbability of heavy metal ions is also pH-dependent. Because the AAc monomer has a  $\text{p}K_{\text{a}}$  of 4.25, microgels composed of AAc are negatively charged at  $\text{pH} > 4.25$ , therefore, these microgels are ionized and present a larger charge density for enhanced absorption. Moreover, the deprotonated carboxylic group at high pH enhances the absorption of metal ions through coordination as well as via electrostatic interactions. The absorption capacity of metal ions can be increased upon lowering the pH to below the  $\text{p}K_{\text{a}}$  of AAc with the deprotonated nature, as shown in Figure 4.1(b).

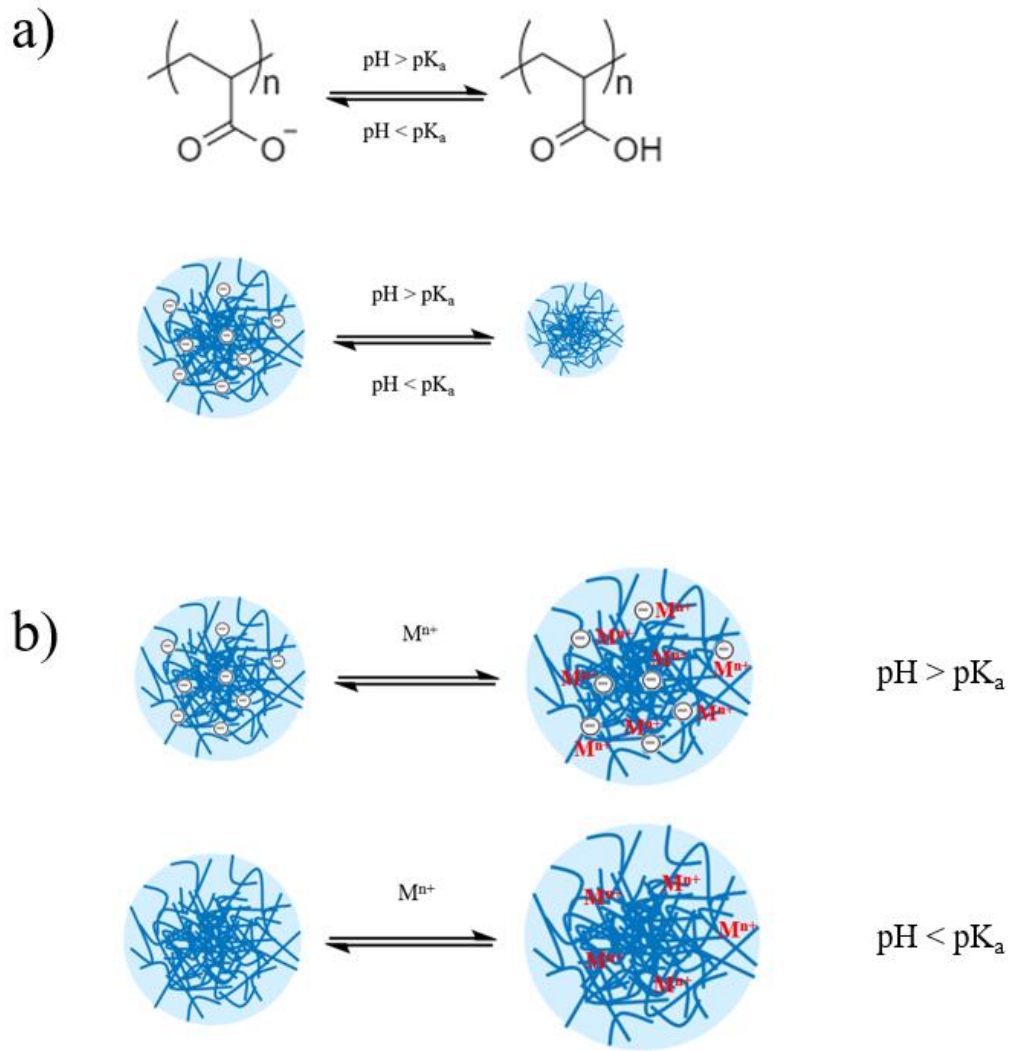


**Figure 4-1.** (a) Swelling/shrinking mechanism of acrylic molecules in microgels and illustration of the conformational change induced by pH changes on pNIPAm-co-AAc microgel particles. (b) The swelling mechanism of microgels is driven by the interaction between acrylic acid molecules and heavy metal ions.

A variety of researchers have explored stimuli-responsive polymer-coated membrane surfaces with a specific metal detection and removal behavior. For example, poly(N-isopropylacrylamide-co-acryloylamidobenzo-18-crown-6) chains were grafted on a membrane surface.<sup>59</sup> The 18-crown-6 crown ether has a high affinity to absorb the  $\text{Pb}^{2+}$  in the solution because of the chelating effect and suitable space size inside the crown. However, this grafting process required additional chemical treatment to graft polymer chains on the membrane surface, which usually is with a complex purification

process, high operational cost, by-products residual, and an increase of potential hazards for drinking water. In contrast, physical coating processes can be controlled more easily than chemical reactions on a membrane surface.

As shown in Chapter 3, the AAc composed microgels can be coated on a membrane surface by a physical stepwise pressure coating process with high stability. This chapter demonstrates how this microgel difference in compositions resulted in different behaviors against heavy metal ions, such as  $\text{Pb}^{2+}$ ,  $\text{Hg}^{2+}$ , and  $\text{Cr}^{3+}$ . The microgel shrink/swell behavior was studied with different pHs in the solution, on the gold slides, and in a microfluidic system. Microgels made of varying compositions of NIPAm and AAc were synthesized by free radical precipitation polymerization; they were characterized previously in Chapter 3. The microgel behavior among  $\text{Pb}^{2+}$ ,  $\text{Hg}^{2+}$ , and  $\text{Cr}^{3+}$  was investigated by the microgels in the solution, microgels coated on a gold slide, and microgels coated on a membrane at different pHs. The absorption efficiency was quantified using an inductively coupled plasma-optical emission spectrometer (ICP-OES).

## 4.2 Experimental Section

*Materials:* N-isopropylacrylamide (NIPAm) monomer was purchased from TCI (Portland, Oregon) and purified by recrystallization from hexanes (ACS reagent grade, EMD, Gibbstown, NJ) before use. N,N'-methylenebisacrylamide (BIS, 99%), acrylic acid (AAc, 99%), ammonium persulfate (APS,  $\geq 98\%$ ), sodium dodecyl sulfate (SDS, 99%) and sodium hydroxide (NaOH) were obtained from Sigma-Aldrich (Oakville, Ontario) and were used as received. Hydrochloric acid (HCl) was purchased from Caledon Lab. (Georgetown, Ontario). Whatman #1 paper filters were obtained from GE Healthcare (U.K.). The heavy metal feed solutions were prepared by lead chloride ( $\text{PbCl}_2$ , J.T. Baker, 99.7%), mercury chloride ( $\text{HgCl}_2$ , Sigma-Aldrich, 99.5%), and chromium chloride ( $\text{CrCl}_2$ , J.T. Baker, 99.8%). In 1987, Brynildson et al<sup>114</sup> investigated the hydrolysis of chromium in aqueous solution.  $\text{Cr}^{2+}$  ions are oxidized rapidly to  $\text{Cr}^{3+}$  by  $\text{O}_2$  in the air without  $\text{N}_2$  or Ar protection.<sup>114</sup> Deionized (DI) water with a resistivity of 18.2  $\text{M}\Omega$  cm was obtained from a Milli-Q Plus system and was used for all experiments. A pH meter (JENCO 6173, San Diego, CA) was used to tune the feed

solution pH. The microfluidic chips and sealing foils were obtained from the microfluidic ChipShop (Jena, Germany). Cr flakes (99.999%) were obtained from ESPI (Ashland, OR), and Au (99.99%) was obtained from MRCS Canada (Edmonton, AB). Polyethersulfone (PES) membrane of average 100 nm surface pore size with polypropylene backing was provided by Solecta membranes (Oceanside, CA) and was used to study microgels as heavy metal ion absorbents on the membrane surface.

#### **4.2.1 PNIPAm-based Microgel Synthesis**

Microgels were synthesized through free radical precipitation polymerization, as discussed on Chapter 3. Briefly, four different compositions of pNIPAm-co-AAc microgels were synthesized. NIPAm (13.3, 11.9, 10.5, and 9.1 mmol, for 0AAc, 10AAc, 20AAc, and 30AAc MG, respectively) and BIS (0.7 mmol) were weighed and dissolved with 99 mL DI water in a 250 mL beaker. The mixture was stirred for 0.5 h on a stir plate and filtered through a 0.2  $\mu\text{m}$  filter into a 3-neck round-bottom flask. The flask was equipped with a reflux condenser, a temperature probe, and a needle for introducing  $\text{N}_2$  gas into the reaction mixture. The reaction mixture was bubbled with  $\text{N}_2$  gas and heated to 70  $^\circ\text{C}$  for 1 h. AAc (0, 1.4, 2.8, 4.2 mmol for 0AAc, 10AAc, 20AAc, and 30AAc MG, respectively) and SDS (3.5 mmol) were added to the heated reaction mixture in one aliquot. Then, the polymerization was initiated immediately by the addition of APS (0.2 mmol) in 1 mL of deionized water. The polymerization was allowed to proceed at 70  $^\circ\text{C}$  for 4 h under an  $\text{N}_2$  environment. The resulting suspension was allowed to cool overnight with continuous stirring, followed by filtration to remove any large aggregates. The microgel solution was distributed into centrifuge tubes and purified by centrifugation at  $\sim 10000$  rpm for  $\sim 30$  min to form a pellet, followed by removing the supernatant and resuspending the pellets in deionized water; this process was repeated six times. All the microgels synthesized and purified above were freeze-dried for further use.

#### **4.2.2 Microgel Behaviors in Solution**

A 10 mg/mL 30%AAc microgel solution at pH 6.5 with ionic strength 4 mM was prepared by adjusting the pH with 1.0 M NaOH and the ionic strength with NaCl. Different concentrations of  $\text{Pb}^{2+}$ ,  $\text{Hg}^{2+}$ , and  $\text{Cr}^{3+}$  solutions were prepared from a 10 ppm

stock solution by adjusting the pH to 6.5 with 1.0 M NaOH. The 0.5 mL of 10 mg/mL microgel solution were spiked into 5 mL of different concentrations of heavy metal solutions. The microgel behaviors in a solution were studied by suspending 0.2 mg/mL microgels with final heavy metal solutions from 5 ppb to 2 ppm, while the suspensions were allowed to stir on a gyration shaker for 24 h to allow the microgels in the solution to interact fully with the metal ions. The microgel behaviors were characterized by the absorbance spectrum obtained from the UV-vis spectrometer.

### 4.2.3 Microgel Behaviors on Au Substrate

The microgel behaviors have been studied further on Au substrates and microfluidic systems. A typical Fabry–Pérot etalon can be used to characterize the shrink/swell behavior of microgels on substrates. The schematic illustration of a typical Fabry–Pérot etalon is displayed in Figure 4-2(a). It consists of two parallel reflective surfaces separated by a thin dielectric layer. Their optical properties are a result of multiple-beam interference between the two reflecting surfaces. The reflection light undergoes multiple internal reflections, resulting in constructive and destructive interference and specific wavelengths of light being reflected/transmitted. The distance changes between two reflection surfaces, caused by the microgels size changes, can indicate the path length differences between the transmitted/reflected wavelengths. Constructive interference occurs when the transmitted/reflected wavelengths are in phase, and can be predicted using Equation 4-1:

$$\lambda m = 2d\eta\cos\theta \quad (4.1)$$

where  $\lambda$  is the maximum reflected/transmitted wavelength,  $m$  is an integer for constructive interference (or order of reflection),  $\eta$  is the refractive index of the dielectric material,  $d$  is the distance between the two reflective mirrors, and  $\theta$  is the angle of incident light. The stimuli-responsive microgels can be used as the dielectric material with the tunable and controllable distance between the two reflective mirrors.

To obtain etalons, 625 mm<sup>2</sup> cover glasses (0.15 mm thickness) were washed using ethanol/DI water and dried over a stream of N<sub>2</sub> gas. Then, 2 nm Cr (as an adhesion layer) and 15 nm Au were deposited onto the cover glasses using a thermal evaporator system (Torr International Inc., New Windsor, NY) at a rate of 0.17 Å s<sup>-1</sup> and 0.22 Å s<sup>-1</sup>

<sup>1</sup>, respectively. The Au coated glass substrates were placed onto a hot plate set at 35 ° C, where an aliquot of 200 μL of the desired concentrated microgel solution was deposited and painted on the substrate glass surface coated with Au until it was covered fully. The microgel film was allowed to air-dry for 2 h, followed by rinsing with a copious amount of DI water to remove any excess microgel. Next, the glass substrates were incubated in DI water overnight and rinsed again with DI water, then dried over a stream of N<sub>2</sub> gas. A second layer of 2 nm Cr/5 nm Au was deposited, yielding 625 mm<sup>2</sup> etalon optical devices. The structure of the device is shown in Figure 4-2(b).

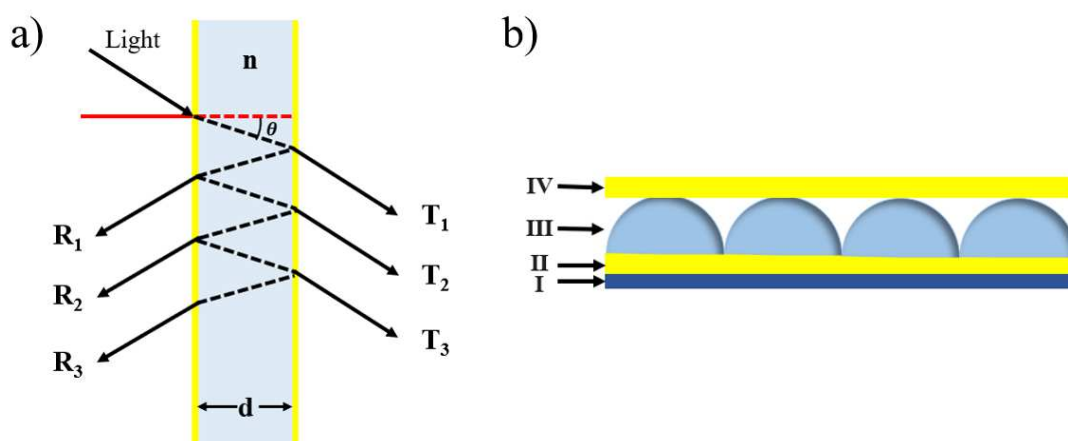


**Figure 4-2.** (a) Schematic illustration of a typical Fabry–Pérot etalon composed of two reflective mirrors (vertical yellow lines) separated by a dielectric material with refractive index  $\eta$  and thickness of  $d$ . Incident light (black arrows) striking the etalon at an angle  $\theta$  enters its cavity and undergoes multiple internal reflections, where constructive and destructive interferences occur in the transmitted ( $T_1$ ,  $T_2$ , and  $T_3$ ) or reflected ( $R_1$ ,  $R_2$ , and  $R_3$ ) waves. (b) The structure of the microgel-based etalon device is composed of two reflective Au layers (II and IV) separated by a microgel layer (III) and constructed on a glass substrate (I).

Reflectance spectra were used to characterize the microgel behavior in the etalon. The resulting etalons showed characteristic peaks in the visible range, as shown in Figure 4-3(a); they are modulated by the actual microgel size, based on Equation 4.1. For example, from Equation 4.1, the peaks in the reflectance spectra are expected to shift to higher wavelengths (red shift) when the microgel swells, while the reflectance peaks are expected to shift to lower wavelengths (blue shift) when the microgel layer shrinks, as shown in Figure 4-3(b). Similarly, varying the solution temperature above/below the microgels' LCST can lead to blue/red shifts in the reflectance peaks,

respectively.

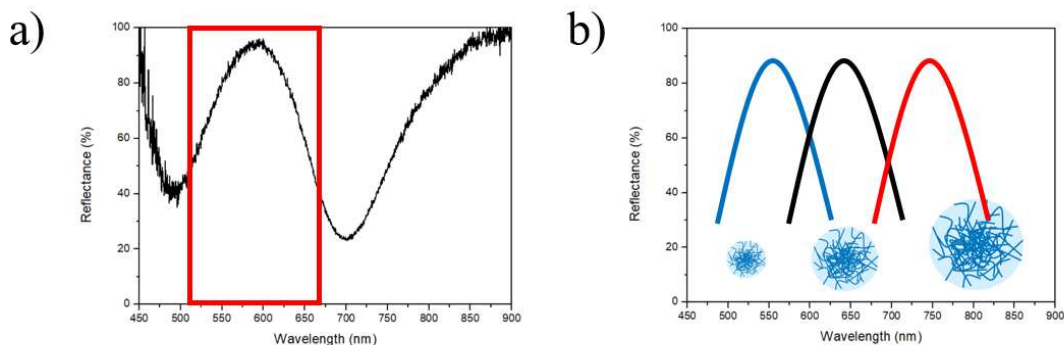


**Figure 4-3.** (a) Representative spectra for an etalon composed of pNIPAm-co-AAc microgels. (b) The peaks shift to higher wavelengths (red shift) when the microgel swells, while the peaks shift to lower wavelengths (blue shift) when the microgel layer shrinks.

The etalon devices made above were placed in a microfluidic system to obtain the microgel behavior using a reflection spectrometer under a heavy metal ion solution. The microfluidic system was designed as shown in Figure 4-4(a). Etalons were placed in the small chamber in the middle of the microfluidic system. There are three inlet channels and one outlet channel to let the metal ion solution go through the small chamber that contains the etalon device. The inlet was connected to a syringe that contained a targeted heavy metal solution, while the outlet was connected to a waste beaker. A syringe pump was used to drive the solution through the microfluidic system. After the microfluidic system was assembled, DI water was pumped through and filled the whole microfluidic chamber along with the etalon device. The etalon device was soaked in DI water overnight to allow the microgel to get hydrated fully, while the inlet and outlet channels were wrapped and sealed with parafilm to avoid evaporation. Firstly, different concentrations of  $\text{Pb}^{2+}$ ,  $\text{Hg}^{2+}$ , and  $\text{Cr}^{3+}$  solutions were prepared from a 10 ppm stock solution by adjusting the pH to 6.5 with 1.0 M NaOH and the ionic strength to 4 mM with NaCl. Then, the heavy metal solution with the lowest concentration was loaded into a syringe and pumped through the microfluidic system at 0.05 mL/min while the reflection spectrum was being recorded in real-time mode. The microgel-based etalon system may take more than 30 min to stabilize. When the reflection spectrum had no significant peak shift over 10 min, the reflection spectrum was

recorded. Then, the solution with a higher concentration was loaded into the syringe and pumped through the microfluidic system at 0.05 mL/min while the reflection spectrum was being recorded in real-time mode. When the reflection spectrum stabilized, the reflection spectrum was recorded. This process was repeated until the highest concentration has been reached for each  $\text{Pb}^{2+}$ ,  $\text{Hg}^{2+}$ , and  $\text{Cr}^{3+}$  solution. The peak shift in the reflection spectrum has been used to investigate the microgel behavior on a substrate.

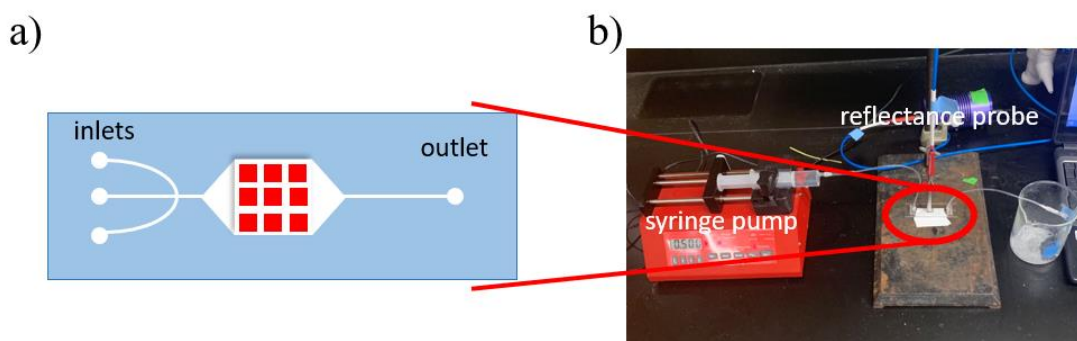


**Figure 4-4.** (a) Structure of the microfluidic device loaded with an etalon sensor in the middle (b) A side view of the etalon sensing experiment basic setup.

#### 4.2.4 Direct Absorption Experiment

A 10 mg/mL microgel solution at pH 6.5 with ionic strength of 4 mM was prepared by adjusting the pH with 1.0 M NaOH and the ionic strength with NaCl. A feed solution that contained 1ppm  $\text{Pb}^{2+}$ , 1ppm  $\text{Hg}^{2+}$ , and 1ppm  $\text{Cr}^{3+}$  was prepared from a 10 ppm stock solution by adjusting the pH to 6.5 with 1.0 M NaOH. The 0.2 mL of 10 mg/mL microgel solution were spiked into 5 mL of feed solution. The sorbent dose was studied by loading the feed solution with 2 mg microgel, which was allowed to stir on a gyration shaker for 1 h and then centrifuged at 10000 rpm for 30 min at 23 °C. The supernatant was removed carefully and analyzed for  $\text{Pb}^{2+}$ ,  $\text{Hg}^{2+}$ , and  $\text{Cr}^{3+}$  by ICP-OES after acidification with 2% (w/v%)  $\text{HNO}_3$ . Calibration curves were established from standard  $\text{Pb}^{2+}$ ,  $\text{Hg}^{2+}$ , and  $\text{Cr}^{3+}$  solutions to estimate the actual metal ion concentration in the suspension and to calculate the amount of metal ion that had been absorbed. The removal percentage of heavy metal ions by the microgel was calculated by Equation 4.2, where  $C_0$  is the initial concentration of sorbate and  $C_e$  is the equilibrium

concentration:

$$\text{Uptake \%} = (C_0 - C_e)/C_0 \times 100 \quad (4.2)$$

#### 4.2.5 Filtration Absorption Experiment

The membrane was obtained by the stepwise pressurized coating process discussed in Chapter 3. Briefly, the 100 nm pore size PES membrane was pretreated to remove the protective coating layer. The pretreated PES membrane was placed at the bottom of the 400 mL dead-end filtration cell. Then, the 55 °C microgel solution was filtered through the membrane under 2 psi at 350 rpm. After the permeate flux became constant for 2 min, the pressure was increased to 5 psi. The pressure was increased stepwise to 10, 15, 20, 30, 40, 50 psi after the permeate flux became constant for 2 min, and the permeate flux was recorded. After the microgel solution had been filtered under 50 psi for 5 min to have a stable permeate flux, the microgel solution was poured out and the membrane was kept under nitrogen pressure for 30 min for drying. Another 400 mL of room-temperature DI water was added gently into the filtration to allow microgel swelling for 2 h. Then, the membrane and the cell were rinsed gently with three portions of 100 mL of room-temperature DI water to remove the uncoated microgel on the membrane surface. The membrane was kept under room-temperature DI water and 150 rpm stirring for 2 d, with periodic DI water replacement every 24 h. The membranes were gently rinsed with DI water before further experiments.

A feed solution that contained 1 ppm  $\text{Pb}^{2+}$ , 1 ppm  $\text{Hg}^{2+}$ , and 1 ppm  $\text{Cr}^{3+}$  was prepared from a 10 ppm stock solution by adjusting the pH to 6.5 with 1.0 M NaOH. The sorbent dose was studied for the filtration feed solution at both atmosphere pressure and 2 psi. 400 mL of feed solution were added to the cell, and the filtration was performed until all the solution passed through the membrane at 150 rpm to allow the metal ion to interact fully with the microgel on the membrane surface. The permeate was collected and further analyzed for  $\text{Pb}^{2+}$ ,  $\text{Hg}^{2+}$ , and  $\text{Cr}^{3+}$  removal percentage by ICP-OES after acidification with 2% (w/v%)  $\text{HNO}_3$ . The removal percentage of heavy metal ions by the microgel was calculated by Equation 4.2.

### 4.3 Results and Discussion

As shown in Chapter 3, the microgels made of varying compositions of NIPAm and AAc were synthesized by free radical polymerization. Four sets of microgels were prepared with NIPAm as the main monomer, with 0 %, 10 %, 20 %, and 30 % AAc comonomers during polymerization (named as 0AAc, 10AAc, 20 AAc, and 30AAc, respectively). They were characterized previously in Chapter 3. DLS measurement indicates hydrodynamic diameters of  $520 \pm 20$ ,  $550 \pm 10$ ,  $590 \pm 20$ , and  $620 \pm 30$  nm for 0AAc, 10AAc, 20 AAc, respectively, at pH 5.5. The increasing sizes with AAc composition are caused by the electron repulsion force among the deprotonated acrylic groups in the microgel. The actual compositions of AAc in the microgel were verified by the ratio of two absorbance peaks from the C=O group for the amide group in NIPAm to the C=O group for the carboxylic acid groups in AAc from FTIR. As shown in Table 3-3, the actual AAc compositions in the microgels are 12.2 %, 19.0 %, and 25.4 % for 10AAc, 20AAc, and 30AAc, respectively.

One of the hypothesized sorption mechanisms between the heavy metal ions (e.g.,  $\text{Pb}^{2+}$ ,  $\text{Hg}^{2+}$ , and  $\text{Cr}^{3+}$ ) and the microgels is electrostatic interaction, as shown in Figure 4-5 (a). Microgels composed with AAc swell at  $\text{pH} > \text{p}K_a$  for AAc ( $\sim 4.25$ ) and shrink at  $\text{pH} < \text{p}K_a$  for AAc ( $\sim 4.25$ ). The carboxylic acid groups from AAc are in the protonated state at  $\text{pH} < 4.25$ , where the microgels have no charge. At higher  $\text{pH} > 4.25$ , the carboxylic acid groups from AAc are in the deprotonated state, where the microgels are negatively charged. The additional electrostatic interaction between the negatively charged microgel and the positively charged metal ions can increase the absorption cavity. All microgel behavior and absorption ability experiments were investigated at  $\text{pH} = 6.5$ , where the carboxylic acid groups were deprotonated with increased AAc-metal ion interaction. The other hypothesized sorption mechanism between the heavy metal ions and the microgels is the chelation by a coordinate covalent bond between the metal ion and the molecules in microgels, as shown in Figure 4-5(b) and (c). The chelation involves the formation or presence of two or more separate coordinate bonds between electron donor groups with free lone pair electrons and a single central metal atom. Based on the Ligand field theory, the lone pair electrons from the N and O atoms from the NIPAm monomer and BIS crosslinker were donated to the unoccupied d or f

orbital on the center metal atom.

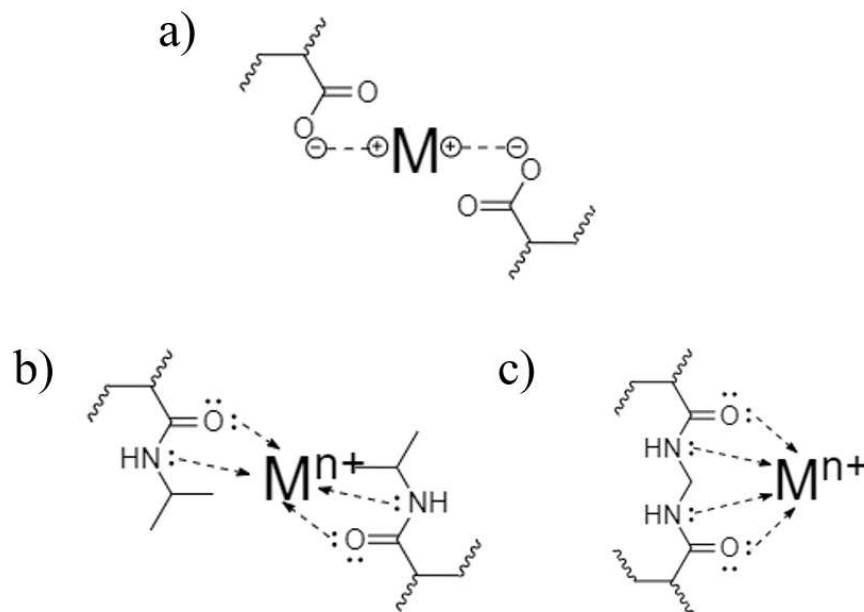


**Figure 4-5.** Proposed sorption mechanism for (a) an electrostatic interaction between the metal ion and AAc in the microgel and for (b) a coordinate covalent bond between the metal ion and NIPAm and (c) BIS.

Because of the incorporation of the interactions discussed above, the microgel composed with AAc acted differently among different metal ions at a constant pH and ionic strength. The dominant interaction can be estimated by the Hard-Soft Acid-Base (HSAB) Theory. “Hard” applies to species which are small, have a high charge density, and weakly polarized. “Soft” applies to species which are big, have a low charge density, and strongly polarized. The chemical hardness ( $\eta$ ) is defined by Pearson in 1988<sup>113</sup> with Equation 4.3:

$$\eta = 0.5 \times (\partial^2 E / \partial N^2) \times Z \quad (4.3)$$

The chemical hardness is defined as being proportional to the second derivative of the total energy of a chemical system with respect to changes in the number of electrons in a fixed nuclear environment. Based on Equation 4.3, the hardness for the eventual metal ions in the solution that I investigated follows an increasing trend of  $Hg^{2+}(7.7) > Pb^{2+}(8.46) > Cr^{3+}(9.1)$ . Following the same theory, all Lewis bases in the solution, including  $OH^-$ ,  $R-COO^-$ , and the electron donors (O and N atom), are

classified as hard acids. However, the Lewis bases from the NIPAm and BIS molecules exhibit higher softness than the ions in the solution. Based on the HSAB theory, in general, hard atoms interact with more electrostatic character, and soft atoms interact with more covalent character, which means that the harder ion,  $\text{Cr}^{3+}$ , is more favorable to the electrostatic interaction and the softer ion,  $\text{Hg}^{2+}$ , is more favorable to the coordinate covalent bond.

To investigate the microgel behavior with heavy metal ions, the 30AAc microgel was soaked in solutions containing different metal ion concentrations at constant  $\text{pH} = 6.5$  and ionic strength = 4mM. The absorbance spectrum for the microgel in each concentration were recorded at 25 °C. Based on Equation 4.4, the absorbance from the UV-vis spectrometer can be defined into two parts: absorbed light intensity and scattered light intensity:

$$A = aN_p l + \tau l \quad (4.4)$$

where  $A$  is the total absorbance output from the UV-vis spectrometer,  $a$  is the absorptivity,  $N_p$  is the number of particles,  $\tau$  is the turbidity, and  $l$  is the path length of the cell. The relationship between turbidity  $\tau$  and particle size is defined by Equation 4.5:

$$\tau \propto \text{constant} \times N_p \times d_p^2 \times \lambda^{-2} \quad (4.5)$$

where  $d_p$  is the particle diameter and  $\lambda$  is the incident light wavelength. The total absorbance contains both absorbed light and scattered light, and the absorbance without absorbed light only contains scattered light.

As shown in Figure 4-6(a), the spectrum from 250 to 450 nm was used to estimate the microgel behavior in a metal ion solution, where the microgel solution does not absorb, and the factor  $a$  is 0. According to Equation 4.4 and 4.5, as  $a$  is 0 and the microgel concentration is constant, the total absorbance is proportional to the square of the microgel size at the same wavelength. For example, the shrinkage of microgel can cause an absorbance decrease in the absorbance spectrum. The absorbance at 400 nm for  $\text{pH} = 6.5$  and ionic strength = 4 mM solution with a 30AAc microgel was used as a standard for further calculations. The ratio of the absorbance at 400 nm is proportional to the square of the ratio of the microgel diameter in the solution, and the

microgel diameter ratio was calculated further by the square root of the ratio of the absorbance at 400 nm, as shown in Figure 4-6(b), (c), and (d).

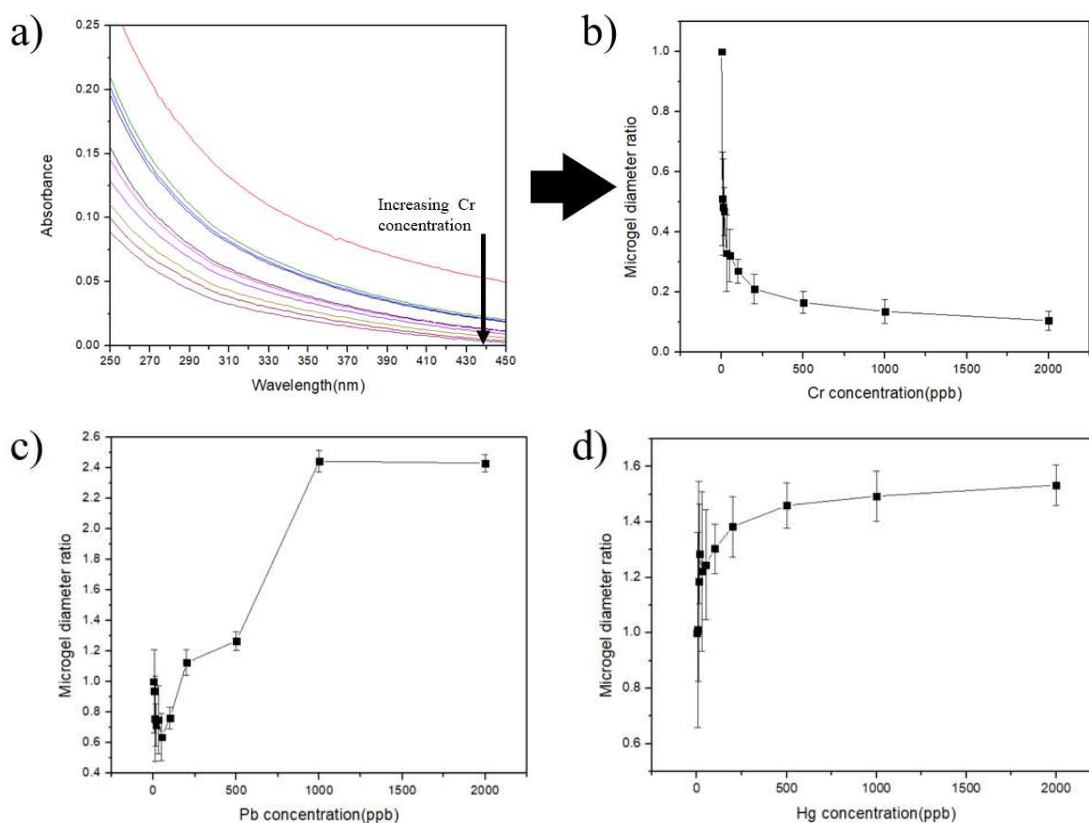


**Figure 4-6.** (a) Representative absorbance spectrum obtained of a 30AAc microgel in the chromium solution with different concentrations. The microgel diameter ratio changes with increasing metal ion concentration were calculated by the square root of the absorbance ratio at 400 nm for (b)  $\text{Cr}^{3+}$ , (c)  $\text{Pb}^{2+}$ , and (d)  $\text{Hg}^{2+}$ .

As the pH and ionic strength are constant, the only factor that influences the microgel sizes is the metal ion. As shown in Figure 4-6(b), (c), and (d), the 30AAc microgel was responsive to all the metal ions used. The metal ions can affect the physical or chemical conformation of the microgel, causing the absorbance spectrum change. Furthermore, we observed different microgel behaviors among the harder Lewis acid  $\text{Cr}^{3+}$ , intermediate Lewis acid  $\text{Pb}^{2+}$ , and softer Lewis acid  $\text{Hg}^{2+}$ .

As shown in Figure 4-6(b), the microgel behavior to a  $\text{Cr}^{3+}$  solution was assessed by monitoring the absorbance of the absorbance spectrum at 400 nm with a UV-vis spectrometer;  $\text{Cr}^{3+}$  yielded microgel size decrease. Following the HSAC theory, we were expecting a hard-hard interaction between the Lewis acid  $\text{Cr}^{3+}$  and the Lewis

base in the solution or microgel. The observation of microgel diameter decrease in  $\text{Cr}^{3+}$  solution supported this hypothesis. Because the hard-hard interaction (electrostatic interaction) is more favorable for the  $\text{Cr}^{3+}$  ion, the negatively charged deprotonated AAc groups in the microgel interacted with the positively charged chromium(III) complex at  $\text{pH} = 6.5$ . The ligand extraction substituted the  $\text{H}_2\text{O}$  ligand to the  $\text{COO}^-$ . Since the multiple  $\text{H}_2\text{O}$  ligands in the  $\text{Cr(III)}$  complex can be substituted by the ligand  $\text{COO}^-$ , it acted as a crosslinker in the microgel, based on the charge attraction, resulting in the microgel shrinkage. Simultaneously, the negative charge in the 30AAc microgel at  $\text{pH} = 6.5$  was neutralized by the interacted  $\text{Cr}^{3+}$  ion. The swelling, based on the electron repulsion at  $\text{pH} = 6.5$ , was absent in the presence of  $\text{Cr}^{3+}$  ion, which caused a further size decrease of the microgel. As the  $\text{Cr}^{3+}$  ion concentration increased, further shrinkage was caused by the increased crosslinker concentration. After all the deprotonated AAc groups interacted with the  $\text{Cr}^{3+}$  ion, additional  $\text{Cr}^{3+}$  ions did not influence the microgel.

As shown in Figure 4-6(d), the microgel behavior to an  $\text{Hg}^{2+}$  solution was assessed by the same method;  $\text{Hg}^{2+}$  yielded microgel size increase. Based on HSAC theory, we were expecting a soft-soft interaction between  $\text{Hg}^{2+}$  and the Lewis base in the solution or microgel. The observation of microgel diameter increase in  $\text{Hg}^{2+}$  solution supported this hypothesis. Although the N and O electron donors in NIPAm and BIS are classified as hard, they were the softer Lewis bases among all the Lewis bases in the solution. Because the coordinate covalent bonds were more favorable for the  $\text{Hg}^{2+}$  ion, the lone pair electrons from NIPAm and BIS molecules in the microgel are donated to the empty orbitals on the  $\text{Hg}^{2+}$  ion to form a coordinate covalent bond in the microgel. The empty space in the microgel was occupied by the large  $\text{Hg}^{2+}$  ion by coordinate covalent bonds, resulting in the microgel swelling. The swelling of the microgel also can be caused by the charge repulsion from the positively charged  $\text{Hg}^{2+}$  ion in the microgel. As the  $\text{Hg}^{2+}$  ion concentration increased, more  $\text{Hg}^{2+}$  ions occupied the space in the microgel, resulting in further swelling. After NIPAm and BIS molecules captured all the  $\text{Hg}^{2+}$  ions, additional  $\text{Hg}^{2+}$  ions did not influence the microgel.

As shown in Figure 4-6(c), the microgel behavior to a  $\text{Pb}^{2+}$  solution was

assessed by the same method;  $\text{Pb}^{2+}$  yielded a complex microgel behavior. The microgel shrinks with low  $\text{Pb}^{2+}$  concentration and swells as the  $\text{Pb}^{2+}$  concentration increases. Because of HSAC theory, we were expecting that  $\text{Pb}^{2+}$  can undergo both electrostatic interaction and a coordinate covalent bond with a Lewis base in the solution or microgel. Because both types of interaction appear for the  $\text{Pb}^{2+}$  ion, the negatively charged deprotonated AAc groups and the lone pair electrons from N and O atoms in NIPAm and BIS both interacted with the  $\text{Pb}^{2+}$  ion. At a low  $\text{Pb}^{2+}$  concentration, it acted as a crosslinker in the microgel, based on the charge attraction, resulting in microgel shrinkage. As the  $\text{Pb}^{2+}$  ion concentration increased, all the negative charges were neutralized by the positive charge from metal ions. The excess  $\text{Pb}^{2+}$  ions after electrostatic attraction were captured by the NIPAm and BIS molecules via coordinate covalent bonds, resulting in the swelling, which explains the shrink-swollen behavior for microgel with the increase in  $\text{Pb}^{2+}$  concentration.

To further verify the pNIPAm-based microgel behavior among  $\text{Cr}^{3+}$ ,  $\text{Hg}^{2+}$ , and  $\text{Pb}^{2+}$ , microgels with different AAc compositions were used to fabricate etalon devices to quantitatively characterize the microgel size changes in heavy metal ion solutions. A microfluidic system was combined with a reflectance probe to quantify the microgel size change on Au substrates. According to Equation 4.1, as the other parameters are constant, the maximum reflected/transmitted wavelength  $\lambda$  is proportional to the distance between the two reflective mirrors  $d$ , which represent the microgel diameter. Either maximum reflected or transmitted wavelength can be used to monitor the microgel behavior in etalons, where the maximum reflected wavelength was shown as the crest and the maximum transmitted wavelength as the trough in the reflection spectrum. The blue shift (decreased  $\lambda$ ) indicates the microgel size decreasing while the red shift (increased  $\lambda$ ) indicates the microgel size increasing. For example, Figure 4-7(a) shows a representative blue shift for the etalon device. The peak at 705 nm shifts to a lower value by increasing the  $\text{Cr}^{3+}$  concentration. The peak shifts were calculated by the actual wavelength for the peak minus the wavelength for the same peak when the microgel is at standard pH = 6.5 and ionic strength = 4 mM solution. The negative peak shifts represent the blue shift with the microgel shrinkage, while the positive peak

shifts represent the red shift with the microgel swollen. The peak shifts were plotted against the metal ion concentration for  $\text{Cr}^{3+}$ ,  $\text{Hg}^{2+}$ , and  $\text{Pb}^{2+}$ , as shown in Figure 4-7 (b), (c), and (d).

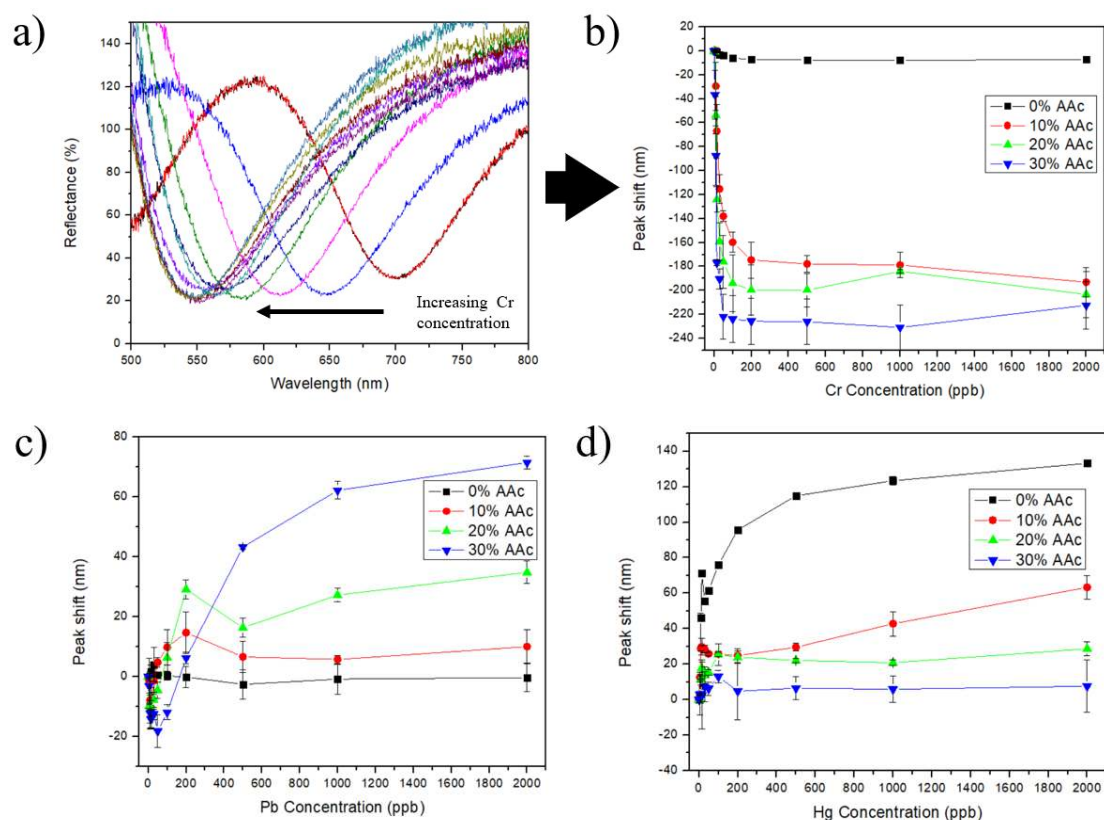


**Figure 4-7.** (a) Representative reflectance spectrum showing a blue shift upon exposure to  $\text{Cr}^{3+}$  solution with increase in concentration. The peak shifts from different etalons made of 0AAc(black), 10AAc(red), 20AAc(green), and 30AAc(blue), along with increasing metal ion concentration for (b)  $\text{Cr}^{3+}$ , (c)  $\text{Pb}^{2+}$ , and (d)  $\text{Hg}^{2+}$ .

The microgel behaviors in heavy metal solutions were discussed above. As shown in Figure 4-7(b), (c), and (d), microgels were responsive in the same way to the expectation based on HSAB theory. Briefly, the harder Lewis acid  $\text{Cr}^{3+}$  is more favorable to interact with the negatively charged AAc group by electrostatic interaction, resulting in microgel shrinkage; the softer Lewis acid  $\text{Hg}^{2+}$  is more favorable to interact with the N and O atoms by coordinate covalent bonds, resulting in microgel swelling; the borderline Lewis acid  $\text{Pb}^{2+}$  is favorable to both interactions, resulting in microgel shrinking at low concentration and swelling at high concentration. This hypothesis on the microgel behavior was confirmed further with a variety of AAc compositions.

Specifically, as shown in Figure 4-7(b), the 0AAc microgels barely were responsive to  $\text{Cr}^{3+}$ . Because of the absence of AAc in the 0AAc microgel, microgels do not contain any negative charged group. The 0AAc microgel was not responsive to  $\text{Cr}^{3+}$  because there is no electrostatic interaction and ligand extraction between 0AAc and  $\text{Cr}^{3+}$ . With increasing AAc composition in the microgel, the  $\text{Cr}^{3+}$  can interact with more negative charges and the  $\text{COO}^-$  ligand in the microgel, which means that the microgel has a higher crosslinker density with the higher AAc composition. Higher crosslinker density causes microgel shrinkage to a smaller size. In contrast, as shown in Figure 4-7(d), the microgels with high AAc composition barely were responsive to  $\text{Hg}^{2+}$ . The 0AAc microgel with no AAc has the biggest response. 0AAc microgels that were polymerized only by NIPAm monomer and BIS crosslinker had the biggest composition of softer Lewis base. Because the  $\text{Hg}^{2+}$  ions are favorable to form coordinate covalent bonds with the N and O atoms from NIPAm and BIS, the occupied space and electron repulsion force drive the 0AAc with the highest NIPAm composition to show the biggest swollen size. The decreased response with increase in AAc composition was caused by two reasons:  $\text{Hg}^{2+}$  ions captured by the NIPAm and BIS also interacted with the negatively charged AAc group; the decrease of NIPAm composition caused a decrease in  $\text{Hg}^{2+}$  capacity in the microgel. For  $\text{Pb}^{2+}$  ions, as shown in Figure 4-7(c), microgels composed with AAc show shrink-swollen behavior, while 0AAc only shows slight swelling. At the microgel shrinkage region where  $\text{Pb}^{2+}$  concentration is low, microgels with a higher AAc composition have a higher shrinkage ratio. The electrostatic interaction dominated at low  $\text{Pb}^{2+}$  concentration. Because the electron density increased with the AAc composition in a microgel, the  $\text{Pb}^{2+}$  crosslinker density also increased, resulting in decreasing microgel sizes. At the microgel swollen region where the  $\text{Pb}^{2+}$  concentration is low, the microgel with a higher AAc composition also shows a higher swollen ratio, based on the electron repulsion force by the  $\text{Pb}^{2+}$  ions captured by the NIPAm molecules.

Based on the microgel behavior in heavy metal ion solutions, the metal ion absorbability was investigated further. Solutions containing 1 ppm  $\text{Cr}^{3+}$ , 1 ppm  $\text{Hg}^{2+}$ , and 1 ppm  $\text{Pb}^{2+}$  at pH = 6.5 and ionic strength = 4mM were used as a feed solution.

The metal ion absorbability was investigated with a microgel solution and a filtration membrane coated with microgel. The heavy metal concentration was measured by the inductively coupled plasma-optical emission spectrometer. Calibration curves have been generated with standard solutions, as shown in Figure 4-8.

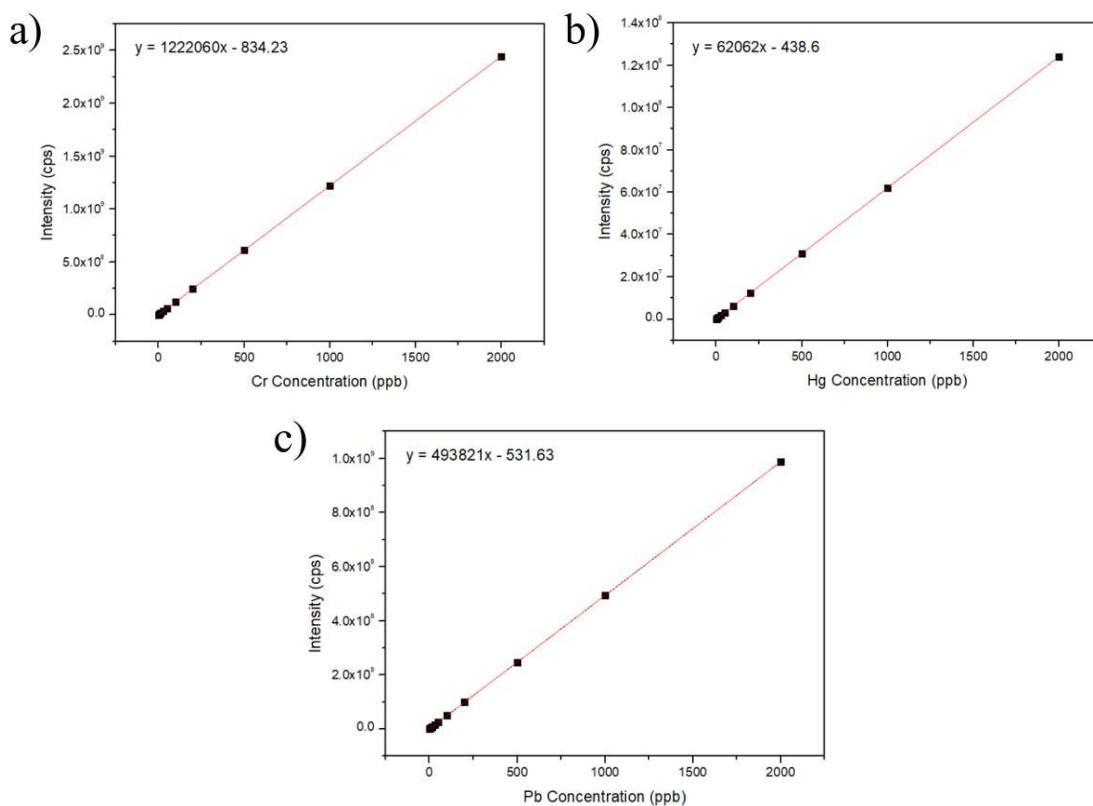


**Figure 4-8.** Calibration curves for (a) Cr<sup>3+</sup>, (b) Hg<sup>2+</sup>, and (c) Pb<sup>2+</sup> used to quantify the amount of Cr<sup>3+</sup>, Hg<sup>2+</sup>, and Pb<sup>2+</sup> sorbed by the microgels. The straight line in each plot is a linear fit to the data using OriginLab Pro version 8.5 program software.

Based on the microgel behaviors discussed above, the heavy metal absorbability can vary in different pHs below or above the  $pK_a$ . The electrostatic interaction between the microgel and heavy metal ions can be influenced significantly by the protonated or deprotonated AAc groups in the microgel. Therefore, it was important to identify the role that pH plays in the removal of these heavy metal ions. The effect of pH on the absorption of Cr<sup>3+</sup>, Hg<sup>2+</sup>, and Pb<sup>2+</sup> was studied at pH values 3.5 and 6.5. To study the effect of pH on metal ion absorption, the metal ion solution and the microgel solutions were adjusted to pH 3.5 and 6.5, followed by adjusting the ionic strength to 4 mM. Calibration curves, as shown in Figure 4-8, were established from

standard  $\text{Cr}^{3+}$ ,  $\text{Hg}^{2+}$ , and  $\text{Pb}^{2+}$  solutions, from which the amounts of  $\text{Cr}^{3+}$ ,  $\text{Hg}^{2+}$ , and  $\text{Pb}^{2+}$  absorbed were calculated. Then, the percentage uptake of amounts of  $\text{Cr}^{3+}$ ,  $\text{Hg}^{2+}$ , and  $\text{Pb}^{2+}$  absorbed by microgels was calculated using Equation 4.2.

Because of the incorporation of AAc groups in the microgels, the solution pH played a critical role in the adoption capacity of heavy metal ions. An increase in the solution pH above the  $\text{pK}_a$  caused the deprotonation of the carboxylic acid groups. There was an overall increase in absorption capacity at  $\text{pH} = 6.5$  because of the electrostatic interaction. The protonation of the carboxylic acid groups at  $\text{pH} = 3.5$  left only coordinate covalent bonds from the N and O atoms on NIPAm and BIS in microgels to capture the heavy metal ions in the solution; this caused the low binding capacity at  $\text{pH} = 3.5$ . At the same time, the low binding capacity at  $\text{pH} = 3.5$  also is caused by the competition between hydronium ions and the target heavy metal ions for their active sites in microgels. In contrast, as the pH is higher than the  $\text{pK}_a$  (at  $\text{pH} = 6.5$ ), high absorption capacities were observed. At  $\text{pH} = 6.5$ , competition from the electrostatic repulsion force and the hydronium ions both decreased; hence, a gradual increase in uptake efficiency was observed. This trend was expected because, at  $\text{pH} = 6.5$ , the microgels are in their deprotonated states and can interact with metal ions via electrostatic interaction.

Specifically, for  $\text{Cr}^{3+}$ , the microgel composited with AAc groups shows significantly higher absorptivity than the microgel without AAc groups, which was expected based on the microgel behavior discussed above. The  $\text{Cr}^{3+}$  ions have a high affinity for the electrostatic interactions with AAc in microgel. 0AAc, which does not contain the AAc group, showed low absorption capacity at both low and high pH because no electrostatic interaction appears. The microgel contains ionizable groups that exhibit increased absorption capacity with increase in AAc composition, based on the increase of negative charge density with the active electrostatic binding positions for  $\text{Cr}^{3+}$  in the microgel. The absorption capacity also increased with pH increase because of the deprotonation of the AAc groups. At  $\text{pH} = 6.5$ , AAc groups were deprotonated and generated more negative charges to capture the  $\text{Cr}^{3+}$  in the solution. In contrast, AAc groups were protonated and contained fewer charges, resulting in

lower absorption capacity. The ~6% absorption of  $\text{Cr}^{3+}$  at  $\text{pH} = 3.5$  may be caused by the incomplete protonation of AAc groups in the microgel. The unprotonated AAc groups with negative charges still can capture  $\text{Cr}^{3+}$  in the solution.

For  $\text{Hg}^{2+}$ , the microgel composited with AAc groups shows similar absorptivity as the microgel without AAc groups, which was expected based on the microgel behavior discussed above.  $\text{Hg}^{2+}$  ions have a high affinity to form coordinate covalent bonds with the lone pair electrons from N and O atoms in the microgel. All microgels with varying AAc compositions contained similar amounts of NIPAm and BIS groups. They showed similarities among each other because a similar amount of coordinate covalent bond can form. However, the absorptive capacity is decreased slightly with increased AAc composition because the NIPAm composition decreased with AAc composition increase. Lower NIPAm composition can cause the less coordinated covalent bonds formed to capture the  $\text{Hg}^{2+}$  in the solution. The absorption capacity also increased with  $\text{pH}$ , but with less increase compared with  $\text{Cr}^{3+}$ . Based on the electrostatic repulsion force between the hydronium ions and  $\text{Hg}^{2+}$ , the competition between two positively charged ions caused the  $\text{Hg}^{2+}$  absorption capacity to decrease. Since the hydronium ions have higher concentrations at lower  $\text{pH}$  and are relatively smaller than  $\text{Hg}^{2+}$  ions, it is easier for hydronium ions to enter the microgel than  $\text{Hg}^{2+}$ .

As discussed above, the  $\text{Pb}^{2+}$  behavior was influenced by both electrostatic interactions and coordinate covalent bonds. The microgel composited with AAc groups shows significantly higher absorptivity than the microgel without AAc groups at low  $\text{pH}$ , while the microgel without AAc groups shows similar absorption capacity as the microgel with AAc. At  $\text{pH} = 6.5$ , the absorption capacity slightly increased with increasing AAc composition for  $\text{Pb}^{2+}$  since AAc groups were deprotonated and generated more negative charges to capture the  $\text{Pb}^{2+}$  in the solution. However, the electrostatic attraction force is not the only force that causes the absorption for  $\text{Pb}^{2+}$ .  $\text{Pb}^{2+}$  ions also were captured by the coordinate covalent bonds. The coordinate covalent bond captured  $\text{Pb}^{2+}$  ions inhibit the electrostatic interactions between deprotonated AAc group and  $\text{Pb}^{2+}$  because of the electrostatic repulsion force. The incorporation of the electrostatic interaction and coordinate covalent bonds resulted in a slightly increased

absorption capacity. At pH = 3.5, the absorption capacity significantly increased with increasing AAc composition for Pb<sup>2+</sup>. The unprotonated AAc groups with negative charges can capture Pb<sup>2+</sup> in the solution, while the hydronium ions were inhibited by the Pb<sup>2+</sup> captured by the electrostatic interaction. Moreover, because of the relatively large ion size, Pb<sup>2+</sup> diffused slower than Cr<sup>3+</sup>, resulting in lower absorption capacity than Cr<sup>3+</sup> in the same amount of time.

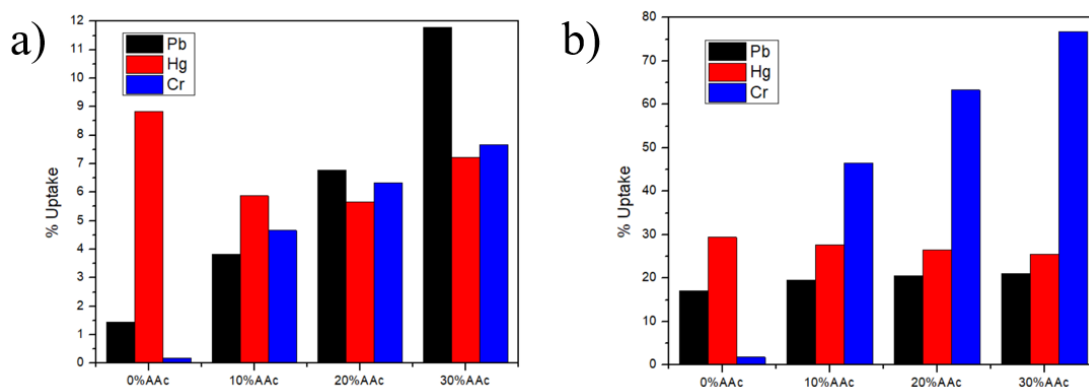


**Figure 4-9** pH comparison of the removal efficiency at pH (a) 3.5 and (b) 6.5 for Cr<sup>3+</sup> (blue), Hg<sup>2+</sup> (red), and Pb<sup>2+</sup> (black). A sorbent dose of 2 mg of microgel was used in a 10 mL total volume, with 1 ppm Cr<sup>3+</sup>, 1 ppm Hg<sup>2+</sup>, and 1 ppm Pb<sup>2+</sup> initial concentrations of the ions.

The heavy metal ion absorption capacity was investigated further on a membrane surface. As shown in Chapter 3, microgels showed the best coating stability at the size of ~500 nm with the stepwise pressurized coating process. Membranes were made following the coating process discussed in Chapter 3. The microgel immobilized membranes were used to filtrate the feed solution containing 1 ppm Cr<sup>3+</sup>, 1 ppm Hg<sup>2+</sup>, and 1 ppm Pb<sup>2+</sup>. Based on the result discussed above, pH = 6.5 provides a much higher absorption capacity than pH = 3.5. The feed solution was tuned to pH = 6.5, followed by adjusting the ionic strength to 4 mM. During the filtration process, the feed and the permeate were collected for metal ion absorption analysis using ICP-OES. The pressure may enhance the interaction between the microgel and metal ions; therefore, it was important to identify the role that pressure plays in the removal of these heavy metal ions during filtration. The effect of pressure on the absorption capacity of Cr<sup>3+</sup>, Hg<sup>2+</sup>, and Pb<sup>2+</sup> during filtration was studied at atmosphere pressure and 20 psi. The same calibration curves, as shown in Figure 4-8, were established from standard Cr<sup>3+</sup>, Hg<sup>2+</sup>,

and  $\text{Pb}^{2+}$  solutions, from which the amounts of  $\text{Cr}^{3+}$ ,  $\text{Hg}^{2+}$ , and  $\text{Pb}^{2+}$  absorbed were calculated. Then, the percentage uptake of amounts of  $\text{Cr}^{3+}$ ,  $\text{Hg}^{2+}$ , and  $\text{Pb}^{2+}$  absorbed by microgels was calculated using Equation 4.2.

Based on the filtration, a higher pressure can result in multiple pathways in the membrane. As the microgel has a hollow structure, the feed solution was able to pass through. However, under low pressure, the external pressure was lower than the osmotic pressure inside the microgel, which resulted in the feed solution passing through the membrane on the side of the microgel. Only the molecules on the microgel surfaces can capture the heavy metal ions in the solution. In contrast, high pressure, which is higher than the osmotic pressure inside the microgels, can force the feed solution to pass through the microgel. Molecules inside the microgel can be involved in the absorption of heavy metal ions. As shown in Figure 4-10, the filtration under 20 psi showed significantly higher absorption capacity than the filtration under atmosphere pressure, which supports the hypothesis.

Specifically, the absorption capacity among different AAc composited microgels was similar to the direct absorption experiment discussed above. Briefly, the absorption capacity for  $\text{Cr}^{3+}$  increases with the increased AAc composition, based on the increasing electrostatic interaction between the negatively charged AAc group and  $\text{Cr}^{3+}$ . The absorption capacity for  $\text{Hg}^{2+}$  decreases with the increased AAc composition, based on the decreasing coordinate covalent bonds with the decreased composition of NIPAm in microgel. The absorption capacity for  $\text{Pb}^{2+}$  slightly increases because of the incorporation of electrostatic interaction and coordinate covalent bonds. This absorption capacity behavior among these four types of microgels was significant at low pressure. The absorption mechanism for filtration at low pressure worked in the same way as the direct absorption because metal ions diffused into the microgel. In contrast, filtration at higher pressure has a significantly high metal absorption capacity. Because the 20 psi pressure is higher than the osmotic pressure inside the microgel, metal ion solutions simply did not diffuse into the microgels. The metal ion solution was forced by pressure through the microgels on the membrane surface, which means that most metal ions had chances to contact the molecules inside the microgel, resulting

in a significant increase in absorption capacity among all metal ions.

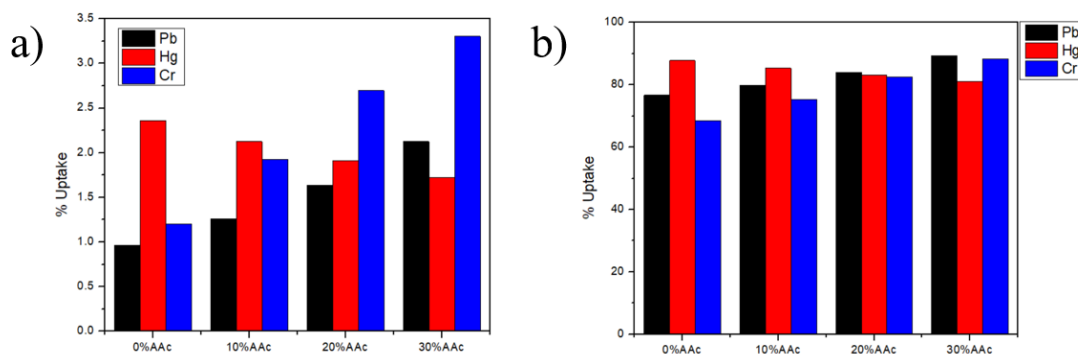


**Figure 4-10.** Pressure comparison on removal efficiency with (a) atmosphere pressure and (b) 20 psi for Cr<sup>3+</sup> (blue), Hg<sup>2+</sup> (red), and Pb<sup>2+</sup> (black). A sorbent dose of 45.4 cm<sup>2</sup> microgel coated membrane was used in a 400 mL total volume, with 1 ppm Cr<sup>3+</sup>, 1 ppm Hg<sup>2+</sup>, and 1 ppm Pb<sup>2+</sup> initial concentrations of the ions.

## 4.4 Conclusion

In summary, pNIPAm-co-AAc microgels sorbents have been synthesized and evaluated for their metal ion binding ability. The porous nature of the microgels made them attractive for the removal of contaminants, while the presence of ionizable groups presented binding sites for heavy metal ion uptake. The microgel behavior can be explained using the HSAB theory. The “hard” Lewis acid Cr<sup>3+</sup> has a high affinity to the harder Lewis base (AAc) in the microgel, while electrostatic interaction dominated. The “soft” Lewis acid Hg<sup>2+</sup> has a high affinity to the softer Lewis base (NIPAm and BIS) in the microgel, while the coordinate covalent bond was dominant. The intermediate Lewis acid Pb<sup>2+</sup> can interact with both a harder Lewis base (AAc) and a softer Lewis base (NIPAm and BIS). The incorporation of electrostatic interactions and coordination influence the microgel behavior with Pb<sup>2+</sup>. The absorption capacity was studied further with various pH and filtration pressures. The deprotonation of the carboxylic groups in microgels increases the metal absorption capacity with more negative charges. The 20 psi pressure during filtration shows almost 80% absorption capacity of 1 ppm metal ions because the external pressure is higher than the osmotic pressure inside the microgel.

## Chapter 5

### Conclusions and Future Outlook

This thesis was primarily focused on the use of polymer-based membranes and materials for water remediation applications. In Chapter 2, the star-shaped polymer was designed to enhance the anti-fouling properties of oily water treatment membranes. Silica-core polymer-arm star-shaped polymers were designed to have both high stability and anti-fouling properties. The silica core and the hydrophilic poly(ethylene glycol)methacrylate arms provided substantial enhancement of the surface hydrophilicity and anti-fouling properties against organic foulants. The hydrophobic polystyrene chains in the arm provide high coating stability through hydrophobic-hydrophobic interaction with the membrane. It was observed that star-shaped polymer composited PES membrane exhibited anti-fouling properties with high surface wettability and low flux decline. However, some of the star-shaped polymers are removed from the membrane as a result of the filtration and washing process, resulting in the inhibition of the anti-fouling properties of the star-shaped polymer. To improve the coating stability and further enhance the anti-fouling properties, a layer-by-layer assembly process can be used. The star-shaped polymer can be designed composited both positive or negative charges in the polymer arms. The positive charge groups have a higher affinity to the membrane since the membrane has a slightly negative surface charge. Then, another layer of negative charged star-shaped polymer can be coated on the membrane surface through the electrostatic interactions to form more stable coating layers. Besides, charge groups on the membrane surface can also provide high hydrophobicity and surface wettability, which can further enhance the anti-fouling properties. Furthermore, other inorganic core materials can also be used to give the star-shaped polymer more functions as required. For example, magnetic particles can be used as the core of the star-shaped polymer. Then, the star-shaped polymer can be coated on the membrane using a magnetic field, which can enhance the coating stability. Titanium is also a candidate for the core of the star-shaped polymer for anti-bacteria

properties.

In Chapter 3, a pNIPAm-based microgel coated membrane surface was developed and optimized with high anti-fouling properties and stability. The pNIPAm-based microgels were coated on PES membranes through a stepwise pressurized coating process with tuned temperature. The coating was done at a temperature higher than pNIPAm's LCST to force the microgels to fully dehydrate and fill pores and the surface of the membrane. The membranes were soaked in DI water at a temperature lower than LCST to force the microgels to be fully hydrated and "locked" in the membrane. Microgels with different sizes were used to optimize the coating stability. The coating processes were also compared to generate the best coating performance. The stepwise pressurized coating process exhibit the best coating stability among regular coating processes. Moreover, with the optimized microgel size above, microgels with variable AAc compositions were used to develop and optimize a stable and highly antifouling coating with self-cleaning behavior. Microgels with higher AAc composition exhibit better anti-fouling properties. 30AAc and 20AAc coating stability was tested by long-term filtration followed by washing with surfactant. 20AAc coating provides the best stability and self-cleaning behavior via alternate water wash above and below LCST. In the future, post coating treatments can be used to further optimize the anti-fouling properties. Because the coating stability decreased with the increased AAc compositions, 30AAc coating shows low stability during long-time operation although it shows the best anti-fouling properties. To obtain both high anti-fouling properties and coating stability, post-coating treatments can be used. For example, the AAc groups in the microgel can further react with glycidyl methacrylate to generate the vinyl groups on the microgel surfaces. The vinyl groups can be further activated with initiator APS to generate free radicals and crosslink each other to form a stable microgel network, which increases the coating stability.

In Chapter 4, the microgel sorbents were investigated for their metal ion binding ability. The porous nature of the microgels made them attractive for use as sorbents for water remediation applications. Microgels behaved differently at different pHs and metal ions following the HSAB rule. Briefly, for hard metal ion  $\text{Cr}^{3+}$ , hard Lewis base

AAc groups in microgel have high affinity through electrostatic interaction, causing the microgel shrink. For soft metal ion  $\text{Hg}^{2+}$ , soft Lewis base NIPAm and BIS groups in microgel have high affinity through coordinate bonds, causing the microgel swollen. For intermediate metal ion  $\text{Pb}^{2+}$ , both hard and soft Lewis groups interacted with the metal ion. With the cooperation of both interactions, microgels exhibited a shrinking-swelling behavior with increasing  $\text{Pb}^{2+}$  concentration. With the same theory, the microgels were investigated as sorbents in a metal ion solution and during filtration with a microgel coated membrane. The absorption capacity was influenced by the solution pH. The microgels have high metal ion capacity at pH 6.5 because of the deprotonated AAc group. Moreover, the microgel has higher metal ions absorption capacity at 20 psi than at atmospheric pressure during filtration because 20 psi is much higher than the osmotic pressure inside the microgel, resulting in the metal ions fully interacting with the whole microgel and high absorption capacity. In contrast, the metal ions only diffused into the mgel, resulting in low absorption capacity. Based on the microgel behaviors among different metal ions, etalon-based heavy metal ion sensor arrays can be designed. The combination of etalons made by microgels with different functional groups, which react differently with metal ions, can be used to identify the metal types in the solution. Furthermore, the incorporation of functional groups with selectivity to metal ions can be designed for specific metal ion sensing. For example, the polymerizable crown ether 4-acrylamidobenzo 18-crown-6 can incorporate into the microgel to impact  $\text{Pb}^{2+}$  selectivity to the microgels. Moreover, it would be interesting to analyze the details of the response kinetics for heavy metal ions and investigate how ion exchange with the polymer occurs.

## References

1. Shannon, M.A.; Bohn, P.W.; Elimelech, M.; Georgiadis, J.G.; Marinas, B.J.; Mayes, A. M. Science and Technology for Water Purification in the Coming Decades, *Nature* **2008**, *452*, 301–310.
2. Zhang, D., Karkooti A., Liu L., Sadrzadeh M., Thundat T., Liu Y., Narain R. Fabrication of antifouling and antibacterial polyethersulfone (PES)/cellulose nanocrystals (CNC) nanocomposite membranes, *J. Membr. Sci.* **2017**, *549*, 350–356.
3. Khorshidi, B., Hajinasiri, J., Ma, G., Bhattacharjee, S., Sadrzadeh, M. Thermally resistant and electrically conductive PES/ITO nanocomposite membrane, *J. Membr. Sci.* **2016**, *500*, 151–160.
4. Jhaveri, J.H., Murthy, Z.V.P. A comprehensive review on anti-fouling nanocomposite membranes for pressure driven membrane separation processes, *Desalination* **2016**, *379*, 137–154.
5. Goosen, M.F.A., Sablani, S.S., Al-Hinai, H., Al-Obeidani, S., Al-Belushi, R., Jackson, D. Fouling of reverse osmosis and ultrafiltration membranes: a critical review, *Separ. Sci. Technol.* **2004**, *39*, 2261–2298.
6. Pasmore, M., Todd, P., Smith, S., Baker, D., Silverstein, J.A., Coons, D., Bowman, C.N. Effects of ultrafiltration membrane surface properties on *Pseudomonas aeruginosa* biofilm initiation for the purpose of reducing biofouling, *J. Membr. Sci.* **2001**, *194*, 15–32
7. Huang, S., Ras, R.H.A., Tian, X. ScienceDirect Antifouling membranes for oily wastewater treatment: interplay between wetting and membrane fouling, *Curr. Opin. Colloid Interface Sci.* **2018**, *36*, 90–109
8. Yuan, T., Meng, J., Hao, T., Wang, Z., Zhang, Y. A scalable method toward superhydrophilic and underwater superoleophobic PVDF membranes for effective oil/water emulsion separation, *ACS Appl. Mater. Interfaces* **2015**, *7*, 14896–14904.
9. Gorouhi, E., Sadrzadeh, M., Mohammadi, T. Microfiltration of oily wastewater using PP hydrophobic membrane, *Desalination* **2006**, *200*, 319–321
10. Gebreslase, G.A., Bousquet, G., Bouyer, D., Review on membranes for the filtration of aqueous based solution: oil in water emulsion, *J. Membr. Sci. Technol.* **2018**, *8*.
11. Miller, D.J., Paul, D.R., Freeman, B.D. An improved method for surface modification of porous water purification membranes, *Polymer* **2014**, *55*, 1375–1383.
12. Lau, W.J., Ismail, A.F., Misdan, N., Kassim, M.A. A recent progress in thin film composite membrane: a review, *Desalination* **2012**, *287*, 190–199
13. Rana, D., Matsuura, T. Surface modifications for antifouling membranes, *Chem. Rev.* **2010**, *110*,

2448–2471.

14. Arahman, N.; Mulyati, S.; Fahrina, A.; Muchtar, S.; Yusuf, M.; Takagi, R.; Matsuyama, H.; Nordin, N. A. H.; Bilad, M. R. Improving Water Permeability of Hydrophilic PVDF Membrane Prepared via Blending with Organic and Inorganic Additives for Humic Acid Separation. *Molecules* **2019**, *24*, 4099.
15. Shamaei, L.; Khorshidi, B.; Islam, M. A.; Sadrzadeh, M. Industrial Waste Lignin as an Antifouling Coating for the Treatment of Oily Wastewater: Creating Wealth from Waste. *J. Cleaner Prod.* **2020**, *256*, 120304.
16. Hong, S. U.; Bruening, M. L. Separation of Amino Acid Mixtures Using Multilayer Polyelectrolyte Nanofiltration Membranes. *J. Membr. Sci.* **2006**, *280*, 1–5.
17. Zhu, Z.; Feng, X.; Penlidis, A. Self-Assembled Nano-Structured Polyelectrolyte Composite Membranes for Pervaporation. *Mater. Sci. Eng., C* **2006**, *26*, 1–8.
18. Wang, L.; Ji, S.; Wang, N.; Zhang, R.; Zhang, G.; Li, J.-R. One-Step Self-Assembly Fabrication of Amphiphilic Hyperbranched Polymer Composite Membrane from Aqueous Emulsion for Dye Desalination. *J. Membr. Sci.* **2014**, *452*, 143–151.
19. Huang, A.; Chen, L.-H.; Kan, C.-C.; Hsu, T.-Y.; Wu, S.-E.; Jana, K. K.; Tung, K.-L. Fabrication of Zinc Oxide Nanostructure Coated Membranes for Efficient Oil/Water Separation. *J. Membr. Sci.* **2018**, *566*, 249–257.
20. Omi, F. R.; Choudhury, M. R.; Anwar, N.; Bakr, A. R.; Rahaman, M. S. Highly Conductive Ultrafiltration Membrane via Vacuum Filtration Assisted Layer-by-Layer Deposition of Functionalized Carbon Nanotubes. *Ind. Eng. Chem. Res.* **2017**, *56*, 8474–8484.
21. Choi, W.; Choi, J.; Bang, J.; Lee, J.-H. Layer-by-Layer Assembly of Graphene Oxide Nanosheets on Polyamide Membranes for Durable Reverse-Osmosis Applications. *ACS Appl. Mater. Interfaces* **2013**, *5*, 12510–12519.
22. Diep, J.; Tek, A.; Thompson, L.; Frommer, J.; Wang, R.; Piunova, V.; Sly, J.; La, Y.-H. Layer-by-Layer Assembled Core–Shell Star Block Copolymers for Fouling Resistant Water Purification Membranes. *Polymer* **2016**, *103*, 468–477.
23. Soltannia, B.; Islam, M. A.; Cho, J.-Y.; Mohammadtabar, F.; Wang, R.; Piunova, V. A.; Almansoori, Z.; Rastgar, M.; Myles, A. J.; La, Y.-H.; Sadrzadeh, M. Thermally Stable Core-Shell Star-Shaped Block Copolymers for Antifouling Enhancement of Water Purification Membranes. *J. Membr. Sci.* **2020**, *598*, 117686.

24. Tokarev, I., Minko, S. Stimuli-responsive hydrogel thin films *Soft Matter* **2009**, 5, 511
25. Flory, P. J.; Rehner, J. Statistical Mechanics of Cross-linked Polymer Networks I Rubberlike Elasticity. *J. Chem. Phys.* **1943**, 11, 512-520.
26. Haraguchi, K., Li, H. J. *Angewandte Chemie International Edition* **2005**, 44, 6500.
27. Kim, J. H., Lee, S. B., Kim, S. J., Lee, Y. M. Rapid temperature/pH response of porous alginate-g-poly (N-isopropylacrylamide) hydrogels, *Polymer* **2002**, 43, 7549
28. Chen, L., Liu, M., Lin, L., Zhang, T., Ma, J., Song, Y., Jiang, L. Thermal-responsive hydrogel surface: tunable wettability and adhesion to oil at the water/solid interface. *Soft Matter* **2010**, 6, 2708.
29. Tanaka, T., Fillmore, D. J. Kinetics of swelling of gels. *The Journal of Chemical Physics* **1979**, 70, 1214.
30. Saunders, B. R., Vincent, B. Microgel particles as model colloids: theory, properties and applications. *Advances in Colloid and Interface Science* **1999**, 80, 1.
31. Saxena, S., Hansen, C. E., Lyon, L. A. Microgel mechanics in biomaterial design. *Accounts of Chemical Research* **2014**, 47, 2426.
32. Gao, J., Hu, Z. Optical Properties of N-Isopropylacrylamide Microgel Spheres in Water. *Langmuir* **2002**, 18, 1360
33. Schild, H. G. Poly (N-isopropylacrylamide): experiment, theory and application. *Progress in Polymer Science* **1992**, 17, 163.
34. Maeda, Y., Nakamura, T., Ikeda, I. Hydration and Phase Behavior of Poly(N-vinylcaprolactam) and Poly(N-vinylpyrrolidone) in Water. *Macromolecules* **2002**, 35, 217.
35. Lee, H.-N., Lodge, T. P. Lower critical solution temperature (LCST) phase behavior of poly (ethylene oxide) in ionic liquids. *The Journal of Physical Chemistry Letters* **2010**, 1, 1962.
36. Heskins, M.; Guillet, J. E., Solution Properties of Poly (Nisopropylacrylamide). *J. Macromol. Sci., Chem.* **1968**, 2, 1441-1455.
37. Cho, E. C., Lee, J., Cho, K. Role of Bound Water and Hydrophobic Interaction in Phase Transition of Poly(N-isopropylacrylamide) Aqueous Solution. *Macromolecules* **2003**, 36, 9929.
38. Liu, H., Zhu, X. Lower critical solution temperatures of N-substituted acrylamide copolymers in aqueous solutions. *Polymer* **1999**, 40, 6985.
39. Furyk, S., Zhang, Y., Ortiz-Acosta, D., Cremer, P. S., Bergbreiter, D. E. Effects of end group polarity and molecular weight on the lower critical solution temperature of poly(N-isopropylacrylamide).

*Journal of Polymer Science Part A: Polymer Chemistry* **2006**, 44, 1492.

40. Dalkas, G., Pagonis, K., Bokias, G. Control of the lower critical solution temperature—type cononsolvency properties of poly(N-isopropylacrylamide) in water—dioxane mixtures through copolymerisation with acrylamide. *Polymer* **2006**, 47, 243.
41. Senff, H., Richtering, W. Influence of cross-link density on rheological properties of temperature-sensitive microgel suspensions. *Colloid & Polymer Science* **2000**, 278, 830.
42. Sun, Q., Deng, Y. In situ synthesis of temperature-sensitive hollow microspheres via interfacial polymerization. *Journal of the American Chemical Society* **2005**, 127, 8274.
43. Berndt, I., Pedersen, J. S., Richtering, W. Temperature-Sensitive Core–Shell Microgel Particles with Dense Shell. *Angewandte Chemie International Edition* **2006**, 118, 1769.
44. Berndt, I., Richtering, W. Doubly Temperature Sensitive Core–Shell Microgels. *Macromolecules* **2003**, 36, 8780.
45. Kratz, K., Hellweg, T., Eimer, W. Influence of charge density on the swelling of colloidal poly (N-isopropylacrylamide-co-acrylic acid) microgels. *Colloids and Surfaces A: Physicochemical and Engineering Aspects* **2000**, 170, 137.
46. Tokarev, I., Minko, S. Stimuli-responsive hydrogel thin films. *Soft Matter* **2009**, 5, 511.
47. Kocak, G.; Tuncer, C.; Butun, V. pH-Responsive Polymers. *Polym. Chem.* **2017**, 8, 144-176.
48. Pourziad, S., Omidkhah, M. R., Abdollahi, M. Improved antifouling and self-cleaning ability of PVDF ultrafiltration membrane grafted with polymer brushes for oily water treatment. *Journal of Industrial and Engineering Chemistry* **2020**, 83, 401–408.
49. Liang, S., Kang, Y., Tiraferri, A., Giannelis, E.P., Huang, X., Elimelech, M.. Highly hydrophilic polyvinylidene fluoride (PVDF) ultrafiltration membranes via postfabrication grafting of surface-tailored silica nanoparticles. *ACS Appl. Mater. Inter.* **2013**, 5, 6694–6703.
50. Zhao, Y., Wen, J., Sun, H., Pan, D., Huang, Y., Bai, Y., Shao, L. Thermo-responsive separation membrane with smart anti-fouling and self-cleaning properties. *Chemical Engineering Research and Design.* **2020**, 156, 333-342
51. Aksoy, C., Kaner, P., Asatekin, A., Culfaz-Emecen, P. Z. Co-Deposition of Stimuli-Responsive Microgels with Foulants During Ultrafiltration as a Fouling Removal Strategy. *ACS Appl. Mater. Interfaces* **2019**, 11, 18711–18719
52. Schwarzenbach, R. P.; Egli, T.; Hofstetter, T. B.; von Gunten, U.; Wehrli, B. Global Water Pollution

- and Human Health. *Annu. Rev. Environ. Resour.* **2010**, 35, 109-136.
53. Rappaport, S. M.; Smith, M. T. Environment and Disease Risks. *Science.* **2010**, 330, 460-461.
54. Zahir, F., Rizwi, S. J., Haq, S. K., Khan, R. H. Low Dose Mercury Toxicity and Human Health. *Environ. Toxicol. Pharmacol.* **2005**, 20, 351-360.
55. Papanikolaou, N. C., Hatzidaki, E. G., Belivanis, S., Tzanakakis, G. N., Tsatsakis, A. M. Lead Toxicity Update. A Brief Review. *Med. Sci. Monit.* **2005**, 11, RA329-RA336.
56. Kimbrough, D. E., Cohen, Y., Winer, A. M., Creelman, L., Mabuni, C. A Critical Assessment of Chromium in the Environment. *Crit. Rev. Environ. Sci. Technol.* **1999**, 29, 1-46.
57. Fu, F. L., Wang, Q. Removal of heavy metal ions from wastewaters: A review. *J. Environ. Manage.* **2011**, 92, 407-418.
58. Kim, Y. S., Lee, H. M., Kim, J. H., Joo, J., Cheong, I. W. Hydrogel adsorbents of poly (Nisopropylacrylamide-co-methacryloyloxymethyl- 12-crown-4) for Li<sup>+</sup> recovery prepared by droplet microfluidics. *RSC Adv.* **2015**, 5, 10656–10661
59. Liu, Z., Luo, F., Ju, X. J., Xie, R., Sun, Y. M., Wang, W., Chu. L. Y. Gating membranes for water treatment: detection and removal of trace Pb<sup>2+</sup> ions based on molecular recognition and polymer phase transition. *J. Mater. Chem. A*, **2013**, 1, 9659–9671
60. Zhou, S., Chu, B. Synthesis and Volume Phase Transition of Poly(methacrylic acid-co-N-isopropylacrylamide) Microgel Particles in Water. *The Journal of Physical Chemistry B* **1998**, 102, 1364.
61. Pelton, R., Hoare, T. Microgel Suspensions: Fundamentals and Applications **2011**, 1, 1.
62. Jin, T., Ma, Y., Matsuda, W., Masuda, Y., Nakajima, M., Ninomiya, K., Hiraoka, T., Fukunaga, J. Y., Daiko, Y., Yazawa, T. Preparation of surface-modified mesoporous silica membranes and separation mechanism of their pervaporation properties. *Desalination* **2011**, 280, 139–145.
63. Xing, L., Guo, N., Zhang, Y., Zhang, H., Liu, J. A negatively charged loose nanofiltration membrane by blending with poly (sodium 4-styrene sulfonate) grafted SiO<sub>2</sub> via SI-ATRP for dye purification, *Separ. Purif. Technol.* **2015**, 146
64. Zhang, L., Lin, Y., Wu, H., Cheng, L., Sun, Y., Yasui, T., Yang, Z., Wang, S., Yoshioka, T., Matsuyama, H. An ultrathin in situ silicification layer developed by an electrostatic attraction force strategy for ultrahigh-performance oil–water emulsion separation, *J. Mater. Chem.* **2019**, 7, 24569–24582.
65. Daer, S., Akther, N., Wei, Q., Shon, H.K., Hasan, S.W. Influence of silica nanoparticles on the desalination performance of forward osmosis polybenzimidazole membranes, *Desalination* **2020**, 491.

50–59.

66. Huang, K., Quan, X., Li, X., Tezel, F.H., Li, B. Improved surface hydrophilicity and antifouling property of nanofiltration membrane by grafting NH<sub>2</sub>-functionalized silica nanoparticles, *Polym. Adv. Technol.* **2018**, 29, 3159–3170.

67. Li, X., Nayak, K., Stamm, M., Tripathi, B. P. Zwitterionic silica nanogel-modified polysulfone nanoporous membranes formed by in-situ method for water treatment, *Chemosphere* **2021**, 280, 130615

68. Akther, N., Phuntsho, S., Chen, Y., Ghaffour, N., Shon, H.K. Recent advances in nanomaterial-modified polyamide thin-film composite membranes for forward osmosis processes, *J. Membr. Sci.* **2019**, 584, 20–45.

69. Jin, H., Rivers, F., Yin, H., Lai, T., Cay-Durgun, P., Khosravi, A., Lind, M.L., Yu, P. Synthesis of AgCl mineralized thin film composite polyamide membranes to enhance performance and antifouling properties in forward osmosis, *Ind. Eng. Chem. Res.* **2017**, 56, 1064–1073.

70. Huang, A., Chen, L.H., Kan, C.C., Hsu, T.Y., Wu, S.E., Jana, K.K., Tung, K.L. Fabrication of zinc oxide nanostructure coated membranes for efficient oil/water separation, *J. Membr. Sci.* **2018**, 566, 249–257

71. Wu, M.B., Zhang, C., Pi, J.K., Liu, C., Yang, J., Xu, Z.K. Cellulose nanocrystals as anti-oil nanomaterials for separating crude oil from aqueous emulsions and mixtures, *J. Mater. Chem. A.* **2019**, 7, 7033–7041.

72. Thomas, S., Pasquini, D., Leu, S. Y., Gopakumar, D. A. Nanoscale Materials in Water Purification. **2019**, 2, 38

73. Yang, Q., Adrus, N., Tomicki, F., Ulbricht, M. Composites of functional polymeric hydrogels and porous membranes, *J. Mater. Chem.* **2011**, 9, 2783–2811.

74. Lohaus, T., Wit, P., Kather, M., Menne, D., Benes, N.E., Pich, A., Wessling, M. Tunable permeability and selectivity: heatable inorganic porous hollow fiber membrane with a thermo-responsive microgel coating, *J. Membr. Sci.* **2017**, 539, 451–457.

75. Dai, W., Barbari, T. Hydrogel membranes with mesh size asymmetry based on the gradient crosslinking of poly(vinyl alcohol), *J. Membr. Sci.* **1999**, 156, 67–79.

76. Fänger, C., Wack, H., Ulbricht, M. Macroporous poly(N-isopropylacrylamide) hydrogels with adjustable size “Cut-off” for the efficient and reversible immobilization of biomacromolecules, *Macromol. Biosci.* **2006**, 6, 393–402.

77. Li, J., Mooney, D.J. Designing hydrogels for controlled drug delivery, *Nat. Rev. Mater.* **2016**, 12, 16071.
78. Tripathi, B.P., Dubey, N.C., Stamm, M. Hollow microgel based ultrathin thermoresponsive membranes for separation, synthesis, and catalytic applications, *ACS Appl. Mater. Interfaces* **2014**, 20, 17702–17712.
79. Wiese, M., Nir, O., Wypysek, D., Pokern, L., Wessling, M. Fouling minimization at membranes having a 3d surface topology with microgels as soft model colloids, *J. Membr. Sci.* **2019**, 569, 7–16.
80. Mura, S.; Nicolas, J., Couvreur, P. Stimuli-responsive nanocarriers for drug delivery. *Nature Materials* **2013**, 12, 991-1003
81. Stuart, M. A. C., Huck, W. T., Genzer, J., Müller, M., Ober, C., Stamm, M., Sukhorukov, G. B., Szleifer, I., Tsukruk, V. V., Urban, M. Emerging applications of stimuli-responsive polymer materials. *Nature Materials* **2010**, 9, 101-113.
82. Xia, Y., Cheng, C., Wang, R., He, C., Ma, L., Zhao, C. Construction of microgels embedded robust ultrafiltration membranes for highly effective bioadhesion resistance, *Colloids Surfaces B* **2016**, 139, 199–210.
83. Chen, X., Zhao, B., Zhao, L., Bi, S., Han, P., Fen, X., Chen, L. Temperature- and pH-responsive properties of poly(vinylidene fluoride) membranes functionalized by blending microgels, *RSC Adv.* **2014**, 4, 29933–29945
84. Menne, D., Pitsch, F., Wong, J.E. A. Pich, M. Wessling, Temperature-modulated water filtration using microgel-functionalized hollow-fiber membranes, *Angew. Chem. Int. Ed.* **2014**, 53, 5706–5710.
85. Zhou, S., Xue, A., Zhang, Y., Li, M., Wang, J., Zhao, Y., Xing, W. Fabrication of temperature-responsive ZrO<sub>2</sub> tubular membranes, grafted with poly (N-isopropylacrylamide) brush chains, for protein removal and easy cleaning. *J. Membr. Sci.* **2014**, 450, 351–361.
86. Chede, S., Escobar, I. Fouling control using temperature responsive N-isopropylacrylamide (NIPAAm) membranes. *Environ. Prog. Sustainable Energy* **2016**, 35, 416–427
87. Mondal, S., Wickramasinghe, S. Photo-induced graft polymerization of N-isopropyl acrylamide on thin film composite membrane: Produced water treatment and antifouling properties. *Sep. Purif. Technol.* **2012**, 90, 231–238.
88. Heyes, D.M., Brańka, A.C. Interactions between microgel particles, *Soft Matter* **2009**, 14, 2681.
89. Bell, D.J., Ludwanowski, S., Luken, A., Sarikaya, B., Walther, A., Wessling, M. Hydrogel

membranes made from crosslinked microgel multilayers with tunable density, *Journal of Membrane Science* **2021**, 620, 118912

90. Goodwin, J. W.; Ottewill, R. H.; Pelton, R.; Vianello, G.; Yates, D. E., Control of particle size in the formation of polymer lattices, *British Polymer Journal* **1978**, 10, 173-180.

91. Parasuraman, D., Serpe, M. J. Poly (N-Isopropylacrylamide) Microgels for Organic Dye Removal from Water. *ACS Appl. Mater. Interfaces* **2011**, 3, 2732-2737.

92. Parasuraman, D., Serpe, M. J. Poly (N-Isopropylacrylamide) Microgel-Based Assemblies for Organic Dye Removal from Water. *ACS Appl. Mater. Interfaces* **2011**, 3, 4714-4721.

93. Parasuraman, D., Leung, E., Serpe, M. J. Poly (N-isopropylacrylamide) Microgel Based Assemblies for Organic Dye Removal from Water: Microgel Diameter Effects. *Colloid Polym. Sci.* **2012**, 290, 1053-1064.

94. Parasuraman, D., Sarker, A. K., Serpe, M. J. Poly(N-Isopropylacrylamide)-Based Microgels and Their Assemblies for Organic-Molecule Removal from Water. *Chemphyschem* **2012**, 13, 2507-2515.  
156

95. Parasuraman, D., Sarker, A. K., Serpe, M. J. Recyclability of poly (Nisopropylacrylamide) microgel-based assemblies for organic dye removal from water. *Colloid Polym. Sci.* **2013**, 291, 1795-1802.

96. World Health Organization and UNICEF Joint Monitoring Programme. (2017). Progress on Drinking Water and Sanitation, 2017 Update and MDG Assessment.

97. Qasem, N. A. A., Mohammed, R. H., Lawal, D. U. Removal of heavy metal ions from wastewater: a comprehensive and critical review, *npj Clean Water* **2021**, 36, 1-15.

98. Hargreaves, A. J., Vale, P., Whelan, J., Constantino, C., Dotro, G., Cartmell, E. Mercury and antimony in wastewater: fate and treatment, *Water Air Soil Pollut* **2016**, 227, 89

99. Al-Rashdi, B. A. M.; Johnson, D. J.; Hilal, N. Removal of Heavy Metal Ions by Nanofiltration. *Desalination* **2013**, 315, 2-17.

100. Abdullah, N.; Gohari, R. J.; Yusof, N.; Ismail, A. F.; Juhana, J.; Lau, W. J.; Matsuura, T. Polysulfone/Hydrous Ferric Oxide Ultrafiltration Mixed Matrix Membrane: Preparation, Characterization and its Adsorptive Removal of Lead (II) from Aqueous Solution. *Chem. Eng. J.* **2016**, 289, 28-37.

101. Alvarez, M. T.; Crespo, C.; Mattiasson, B. Precipitation of Zn(II), Cu(II) and Pb(II) at Bench-scale Using Biogenic Hydrogen Sulfide from the Utilization of Volatile Fatty Acids. *Chemosphere* **2007**, 66,

1677-1683.

102. Chen, Q.; Luo, Z.; Hills, C.; Xue, G.; Tyrer, M. Precipitation of Heavy Metals from Wastewater Using Simulated Flue Gas: Sequent Additions of Fly Ash, Lime and Carbon Dioxide. *Water Res.* **2009**, 43, 2605-2614.

103. Gupta, S.; Tai, N.-H. Carbon Materials as Oil Sorbents: A Review on the Synthesis and Performance. *J. Mater. Chem. A* **2016**, 4, 1550-1565

104. Li, B.; Zhou, F.; Huang, K.; Wang, Y.; Mei, S.; Zhou, Y.; Jing, T. Highly Efficient Removal of Lead and Cadmium During Wastewater Irrigation Using a Polyethylenimine-grafted Gelatin Sponge. *Sci. Rep.* **2016**, 6, 33573.

105. Lee, C.G.; Jeon, J.W.; Hwang, M.J.; Ahn, K.H.; Park, C.; Choi, J.W.; Lee, S.H. Lead and copper removal from aqueous solutions using carbon foam derived from phenol resin. *Chemosphere* **2015**, 130, 59–65.

106. Maneechakr, P.; Karnjanakom, S. Adsorption behaviour of Fe(II) and Cr(VI) on activated carbon: Surface chemistry, isotherm, kinetic and thermodynamic studies. *J. Chem. Thermodyn.* **2017**, 106, 104–112.

107. Petrus, R.; Warchol, J.K. Heavy metal removal by clinoptilolite. An equilibrium study in multi-component systems. *Water Res.* **2005**, 39, 819–830

108. Bajda, T.; Klapyta, Z. Adsorption of chromate from aqueous solutions by HDTMA-modified clinoptilolite, glauconite and montmorillonite. *Appl. Clay Sci.* **2013**, 86, 169–173

109. Bajda, T.; Szala, B.; Solecka, U. Removal of lead and phosphate ions from aqueous solutions by organo-smectite. *Environ. Technol.* **2015**, 36, 2872–2883.

110. Wang, Y.Y.; Liu, Y.X.; Lu, H.H.; Yang, R.Q.; Yang, S.M. Competitive adsorption of Pb(II), Cu(II), and Zn(II) ions onto hydroxyapatite-biochar nanocomposite in aqueous solutions. *J. Solid State Chem.* **2018**, 261, 53–61

111. Snowden, M. J.; Thomas, D.; Vincent, B. Use of Colloidal Microgels for the Absorption of Heavy-Metal and Other Ions from Aqueous-Solution *Analyst* **1993**, 118, 1367-1369.

112. Morris, G. E.; Vincent, B.; Snowden, M. J. Adsorption of Lead Ions onto N-isopropylacrylamide and Acrylic Acid Copolymer Microgels. *J. Colloid Interface Sci.* **1997**, 190, 198-205.

113. Pearson, R. G. Chemical Hardness and Bond Dissociation Energies *Inorg. Chem.* **1988**, 27, 734.

114. Brynildson, M. E., Bakac, A., and Espenson, J. H. Evidence for a Bond Homolysis Pathway for O<sub>2</sub>

Release in the Decomposition of the Superoxo-chromium(III) Ion  $\text{CrO}_2^{2+}$  *J. Am. Chem. Soc.* **1987**, 109, 4579-4583.